

國立交通大學
機械工程學系

博士論文



環形振動式陀螺儀與加速規混成式微感測器之研究

**Investigation on the Hybrid Ring-type Vibrating Micro
Gyroscope and Accelerometer**

研究生：翁 瑞 鴻

指導教授：成 維 華 教授

中華民國 九十四年七月

環形振動式陀螺儀與加速規混成式微感測器之研究

**Investigation on the Hybrid Ring-type Vibrating Micro Gyroscope
and Accelerometer**

研究生：翁 瑞 鴻 **Student: Jui-Hong Weng**

指導教授：成 維 華 **Advisor: Dr. Wei-Hua Chieng**

國 立 交 通 大 學

機 械 工 程 學 系

博 士 論 文

A Dissertation

Submitted to Department of Mechanical Engineering

College of Engineering

National Chiao Tung University

in Partial Fulfillment of the Requirements

for the Degree of Philosophy

in

Mechanical Engineering

July 2005

Hsinchu, Taiwan, Republic of China

中華民國九十四年七月

環形振動式陀螺儀與加速規混成式微感測器之研究

研究生：翁瑞鴻

指導教授：成維華教授

國立交通大學機械學系

摘 要

本論文針對環形振動式微陀螺儀之結構設計、電路分析與製程實作等予以研究，並且考慮加速規功能以延伸成環形振動式陀螺儀與加速規混成式微感測器。結構設計考量須包含環形振動式陀螺儀之工作原理與元件受加速度下之變化，文中以對稱性分析結構設計所造成之影響，結果顯示結構須同時具備旋轉對稱與鏡面對稱。電路分析包含驅動電路與感測電路。驅動力來源係利用電容兩電極板間之靜電力，類似機制則可應用於感測電路。由於結構驅動於其共振頻率可有效增加訊號強度，驅動電路加入鎖相迴路則可達此目的。元件實作係利用矽晶片以反應離子蝕刻配合陽極接合技術，可製造懸浮結構與可振動結構，具高度可行性。製程設計主要針對消除在乾蝕刻過程所產生的尺寸效應。

Investigation on the Hybrid Ring-type Vibrating Micro Gyroscope and Accelerometer

Student: Jui-Hong Weng

Advisor: Dr. Wei-Hua Chieng

Department of Mechanical Engineering
National Chiao Tung University

Abstract

The dissertation discusses the structure design, electronic circuit analysis and fabrication of the hybrid sensor; the sensor is designed, based on vibrating ring gyroscope, to detect one angular rate and two accelerations on the associated plane. The structural design considers the principle of vibrating ring gyroscope and structural dynamics under acceleration. Symmetric analysis shows that both rotational symmetry and mirror symmetry are basic requirements for the sensor. Electronic circuit analysis includes driving circuit and sensing circuit. The electrostatic force between structures provides driving force; on the other hand, the similar mechanism is used in the sensing scheme. The phase locked loop in the driving circuit is used to excite the structure at the natural frequency to amplify the signal. The structure is fabricated by using reactive ion etching and anodic bonding technologies to carry out the suspending structure. The process is developed for eliminating the aspect ratio dependent effect (ARDE) in dry etching process.

致 謝

逝者如斯乎，不捨晝夜。受教於成維華老師已近十年，平易近人的態度，實事求是的風格，極為耐心的教導，早已在我的生命中刻下不可抹滅的痕跡。在此感謝老師數年來的督促與指導，啟我童蒙，使我受益良多，並使得本論文得以完成。

感謝每位口試委員精闢的見解與指教。「聽君一席話，勝讀十年書」，正代表我對每位口試委員的感謝。

研究期間，感謝賴振民學長的幫助，並且在精神上、實驗上提供寶貴的經驗與協助。感謝蔡奇洋學弟協助我克服許多實驗中的困難。感謝學弟童永成、楊嘉豐、張仰宏、吳秉霖、黃旭生等在各方面的協助，以及實驗室諸位學長學弟的相互支援與鼓勵。

最後，我要感謝我的母親，對孩兒無盡的付出，永遠的關懷與包容，衷心的將此學位的榮耀獻給親愛的母親。並感謝所有關心我的親朋好友，謝謝。

Contents

摘 要.....	i
Abstract.....	ii
致 謝.....	iii
Contents	iv
List of Figures	vi
List of Tables	x
CHAPTER 1 INTRODUCTION.....	1
1.1 General Introduction	1
1.2 Architecture of the Dissertation.....	3
CHAPTER 2 DESCRIPTION OF THE VIBRATING GYROSCOPE	5
2.1 Reviews.....	5
2.2 Principles.....	11
CHAPTER 3 STRUCTURE DESIGN.....	16
3.1 Vibrating Ring Gyroscope	16
3.2 Symmetry	20
3.2 Natural Frequency.....	23
CHAPTER 4 ELECTRONICS CIRCUIT	26
4.1 Interface	26
4.2 Control Loops	33
4.3 Driving Circuit.....	33
4.4 Detection Modes	39
4.5 Schema for Detecting Rotation and Acceleration	42
4.6 Theoretical Errors	44
CHAPTER 5 FABRICATION	46
5.1 Brief of Process Technologies	46
5.2 Fabrication Process	49
5.3 Sensitivity of Sensor Characteristics to Manufacturing Errors in Fabrication	53
5.4 Preliminary Test.....	54

CHAPTER 6 CONCLUSION.....	56
6.1 Summary of the Research	56
6.2 Potential Improvement of the Design	46
References.....	59
List of Publication.....	116



List of Figures

Figure 2.1 Vibrating beam gyroscope	70
Figure 2.2 Tuning fork gyroscope	70
Figure 2.3 Dual accelerometer gyroscope	71
Figure 2.4 Double gimbals vibrating gyroscope	71
Figure 2.5 Schematic diagram for z-axis vibrating gyroscope.....	72
Figure 2.6 Z-axis vibrating gyroscope.....	72
Figure 2.7 Schematic diagram for x-axis vibrating gyroscope.....	73
Figure 2.8 X-axis vibrating gyroscope	73
Figure 2.9 Schematic diagram for dual-axis vibrating gyroscope.....	74
Figure 2.10 Dual-axis vibrating gyroscope	74
Figure 2.11 Poly-silicon vibrating ring gyroscope (PRG).....	75
Figure 2.12 Vibrating ring gyroscope (Si-VSG)	75
Figure 2.13 Simple pendulum and its projection on: (a) fixed frame; (b) rotating frame	76
Figure 2.14 (a) A particle moves above a rotating frame; (b) the path projection on the rotating frame.....	77
Figure 2.15 The frame rotates counterclockwise and a particle P moves on it with velocity.....	78
Figure 2.16 The position vector of a point P relative to a rotating system.....	78
Figure 2.17 (a) The Coriolis force on a rotating disk; (b) the steady precession of a gyroscope	79
Figure 3.1 (a) The radial displacement u and tangential displacement v for the circular ring; (b) $n=0$; (c) $n=1$; (d) $n=2$; (e) $n=3$; (f) $n=4$	80
Figure 3.2 (a) The 2nd mode vibration shapes and its generalized coordinates; (b) the primary mode on 0 degree axis; (c) the secondary mode result from Coriolis force on 45 degree axis	81
Figure 3.3 Coordinate system of the sensor	82
Figure 3.4 Motion of the ring, comprising first and second modes of vibration	82

Figure 3.5 Supports arrangement (a) four supports; (b) eight supports	83
Figure 3.6 (a) Structural deformed due to linear acceleration along x-axis; (b) force response for the force applied at one point positive to x-axis.....	84
Figure 3.7 The vibrating ring gyroscope with symmetry support and symmetry arrangement.....	85
Figure 3.8. (a)(b)Scheme for detecting rotation of gyroscope; (c)(d) scheme for detecting linear acceleration of accelerometer	86
Figure 3.9 Finite element analysis: the part of the structure modeled by quadrilateral shell elements and convergence of the natural frequency with mesh refinement.....	87
Figure 3.10 Mode shape of the structure (a) rotation mode; (b) plane motion mode; (c) 2nd vibration mode; (d) 3rd vibration mode.....	88
Figure 4.1 (a) Top view of structure with electrode; (b) detail view of support with electrode.....	89
Figure 4.2 Intersects of electrostatic force and structure rebalance force	90
Figure 4.3 The variable capacitor connected to the detection circuit represented by an impedance	90
Figure 4.4 (a) Schematic diagram for detection scheme; (b) output voltage plot for 1n farad (line 1) and 1p farad (line 2).....	91
Figure 4.5 (a) Output voltage plot for variable capacitance C2; (b) schematic diagram for detection with stray capacitance. .	92
Figure 4.6 (a) Basic circuit for switched-capacitor; (b) stray-insensitive design	93
Figure 4.7 (a) Basic circuit for detection scheme; (b) schematic diagram for capacitive detection circuit.....	94
Figure 4.8 (a) Schematic diagram for basic circuit with internal resistance; (b) output voltage plot shows periodical disturbance	95
Figure 4.9 Schematic overview of control loops and structure	96

Figure 4.10 (a) Schematic diagram of microstructure with PLL driving circuit; (b) Silicon structure etched with RIE and observed with optical microscope (10 x 5)	97
Figure 4.11 (a) Function block diagram for second order system with PLL; (b) experiment apparatus setup.....	98
Figure 4.12 Numerical results: (a) $\zeta = 1$; (b) $\zeta = 0.01$; (c) $\omega_n = 1000\text{Hz}$ and $\zeta = 0.01$	99
Figure 4.13 Experimental results: (a) bode diagram of the emulation plant; (b) tracking profile	100
Figure 4.14 (a)Arrangement of driving electrodes and sensing electrodes;(b) linear displacement; (c) rotation	101
Figure 4.15 Schematic function diagram for rebalanced control circuit	102
Figure 4.16 Applying forces and corresponding displacements under second mode.....	102
Figure 5.1. Fabrication by method I: (a) silicon patterning using photo resist, (b) deep silicon etching, (c) anodic bonding, (d) back-sided wet etching and (e) releasing of structure	103
Figure 5.2 Photographs of the ring-type motion sensor fabricated by the process shown in Fig. 5.1. (a) Side view of the structure, with ARDE effect shown; (b) top view of a corner of the structure, 20 μm high	104
Figure 5.3 Fabrication by method II (method I with dummy fields): (a) silicon patterning using photo resist, (b) deep silicon etching, (c) protective layer deposition, (d) anodic bonding, (e) back-sided wet etching and (f) releasing of structure	105
Figure 5.4 Photographs of the ring-type motion sensor fabricated using process shown in Fig. 5.3. Top view of the structure, 60 μm high.....	106
Figure 5.5 Fabrication by method III: (a) silicon patterning using photo resist, (b) deep silicon etching, (c) protective layer deposition, (d) anodic bonding, (e) back-sided wet etching and (f) releasing of structure	107
Figure 5.6 Photographs of the ring-type motion sensor fabricated using process in Fig. 5.5. Top view of a structure with a height of 180 μm , under back lighting through the glass	108

Figure 5.7 Normalized sensitivities of sensor characteristic of interest versus manufacturing errors in the gap width..... 109

Figure 5.8 (a) Photograph of the ring-type motion sensor when the support ring is in a neutral position. (b) Electrical connections..... 110

Figure 5.9 (a) Photograph of the ring-type motion sensor when the support ring is attracted by electrode. (b) Deformed structure. (c) Electrical connections..... 111

Figure 5.10 (a) Connections of electrical test. (b) Simplified model. (c) Frequency response..... 112



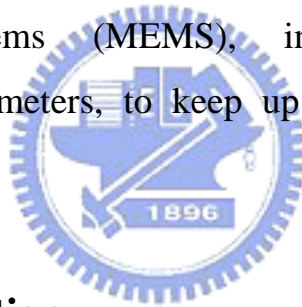
List of Tables

Table. 1 Natural frequency of separated parts of the structure.....	113
Table. 2 Comparison between calculated and simulated results	113
Table. 3 Comparison of identification data and experimental results	114
Table. 4 Rebalance Force on Electrodes for Compensating Acceleration	114
Table. 5 Applying forces and induced displacements under second mode.....	115
Table. 6 Dimensions of parameters	115



Chapter 1 Introduction

Sensors for detecting motion have received considerable interest in recent decades. The gyroscope and the accelerometer represent two important categories of inertial technology for detecting motion. Sensor technology has evolved from discrete, expensive and inflexible units to smart, self-calibrating, silicon-based devices, which are integrated, low-cost and small, and exhibits other advantageous properties [1,2]. The rapid development of semiconductor technology has enabled micro electromechanical systems (MEMS), including micro-machined gyroscopes and accelerometers, to keep up with the requirements of modern sensors.



1.1 General Introduction

The gyroscope is used in many applications, including guidance systems, navigation systems and control systems. Specific applications of the gyroscope include tactical weapon guidance, ship and airplane navigation, craft attitude control, motor sensors and commercial electronics [3]. Many different concepts of gyroscope have been conceived and successfully developed. The conventional gimbaled spinning wheel or rotor is the most known gyroscope. The laser ring gyro is also widely applied and proven in inertial navigation applications [4]. Though high accuracy, these devices are too expensive for low-cost application and too large for minimal size requirement. The vibrating gyroscope is another successful class of gyro designs. It uses vibrating

mechanical elements to sense the rotation, that means no spinning and lubrication parts are needed. By the 1960s, engineers began to try alternative to the wheel using vibrating rather than rotating bodies to provide gyroscopic torques from the Coriolis acceleration. Most gyroscope engineers were developing vibrating gyroscopes based on vibrating strings and tuning forks. Vibrating gyroscopes not only produce low-cost devices but also still have medium performance due to the precision of micro-machining techniques. Vibrating string gyro, tuning fork gyro, vibrating shell gyro are known as vibratory rate sensor or rotation sensor [5]; all of them could be implemented with micro-machining technology. The hemispherical resonator gyroscope (HRG) [6], a kind of vibrating shell gyro, has achieved inertial navigation performance levels rivaling that of the laser ring gyro. The vibrating ring type gyro, which is a simplified case of vibrating shell gyro, is the subject of this dissertation. The specific structural design of such gyro makes it particularly candidates for integration into accelerometers.

Accelerometer is widely used in many applications of engineering for several decades and many different successful designs have been convinced. Since the piezo-resistive silicon accelerometer was developed by Roylance LM[7] in 1977, the silicon-based accelerometer has become a main stream of the acceleration detection sensor instead of the convectional pendulous accelerometer. Those silicon-based devices can be classified into piezo-resistive, capacitive, piezo-electric, piezo-junction effect, thermal, electromagnetic and electron tunneling accelerometer [7-13]. Its structural design and simplicity of fabrication make the capacitive accelerometer a popular type of accelerometer. Furthermore, the basic scheme of the capacitive accelerometer exploits electrostatic force, which can drive a vibrating microstructure. With consideration of structure

design, simple process and fabrication, the capacitive accelerometer fits our requirement.

Notably, the vibration of a circular ring can be theoretically decoupled into several modes. The first mode stands for the linear motion, and the second involves rotation. Two independent vibration modes exist concurrently. Therefore, the capacitive accelerometer and the vibrating ring gyroscope can be integrated in a motion sensor that detects both acceleration and rotation.

1.2 Architecture of the Dissertation

The purpose of the dissertation is to investigate a motion sensor that can sense both rotation and acceleration. The structural design concept includes the principles of both gyroscope and accelerometer. The structure is designed base on vibrating ring gyroscope. The principle of the vibrating gyroscope is described in Ch. 2. It also reviews several types of vibrating gyro and discusses the mechanism of a vibrating gyroscope.

Structural design of the sensor is discussed in Ch. 3. Deriving the governing equations of a vibrating ring helps to understand the mechanism of a vibrating ring gyroscope and requirements in designing structure. The symmetry of the structure design is discussed in this chapter with considering for integration of gyro and accelerometer. The structural natural frequency is also discussed.

Chapter 4 talks about interface circuit, driving circuit, and control loops. Several types of interface circuits are reviewed. A phase locked loop is merged into the driving circuit. The signal phase lag and magnitude are discussed to select detection modes. Theoretical errors are also discussed.

In Chapter 5, structural fabrication and preliminary test of the fabrication results are presented. The structure is made by silicon and formed with dry etching. Inductive coupled plasma (ICP) is used for deep silicon etching process, and anodic bonding is used to create a suspending structure for the vibration. Several sets of process are developed for eliminating the aspect ratio dependent effect (ARDE) that always affects the performance of deep silicon etching.

Chapter 6 concludes this dissertation and shows the contributions of this effort. Future interests and efforts are also recommended.



Chapter 2 Description of the Vibrating Gyroscope

The structure of motion sensor proposed in this dissertation is based on vibrating ring gyroscope. As mentioned in chapter one, many micro-machined vibrating gyroscopes have been carried out with different design concept. These types of micro-machined vibrating gyroscopes are reviewed in this chapter. The basic mechanism of the vibrating gyro is based on Coriolis acceleration that comes from the rotational difference between two rotating frames. To understand this, we analyze the Coriolis effect with the respect of classical mechanics [14-18]. The principle and measurement scheme of vibrating ring gyro are discussed in this chapter.

2.1 Reviews

An original design of vibrating gyro is the vibrating string gyro, which was described by Quick [19] in 1964. The string vibrates in a plane and the plane of vibration tends to stay fixed in space without extra applied. With the string lying along the z-axis and vibrating in xz-plane, a pickoff positioned along y-axis is used to measure the induced vibration. The Coriolis acceleration induced by the rotation causes the string vibration to be coupled into the y-axis, and the amplitude is positive proportional to the rotation rate. In order to avoid the environment noise, the implying frequency is usually above 10kHz. Anisoelectricity and geometric asymmetry cause large drift errors; bias torques arisen form

asymmetry damping and end attachment. There is no successful marketed vibrating string gyro.

A similar design to the vibrating string gyro is the vibrating beam gyro. Due to square or rectangular cross section, the beam vibrates with its two identical bending modes as shown in Fig. 2.1[20]. The beam, which is lying along with the z-axis, vibrates in the xz-plane of the primary mode, and the Coriolis force induced vibration on the secondary mode. Typically, the primary mode amplitude is driven to be fixed. The output amplitude of secondary mode is proportional to the rotation rate. Beam actuation and detection usually uses piezo-electric transducer; capacitively actuation and detection are also available. There are other kinds of cross section such as triangular and etc [21], which still works with two identical modes. The problem of this kind of design is the large temperature drift. It usually comes from the piezo-electric material and their cement layers. The other one is mounting problem. Moreover, the flexibility along the beam axis causes the device to be sensitive to the environmental vibration.

To solve the mounting problem, the structure is transformed into the symmetry design as shown in Fig. 2.2[22,23]. The principle for the tuning fork likes that for the vibrating beam gyroscope. For balanced system made from two bars oscillating anti-phase, it has no net torque at the junction and can obtain stable mounting condition. It leads to low energy loss and obtain higher Q factor. The symmetry design usually forms as tuning fork or trident. The balance structure is less sensitive to the linear acceleration with respect to the vibrating beam gyro. But it has large zero bias error for its open loop operation. Besides, the misalignment for individual tines that makes a vibration torque also leads to the bias error. The bending and torsional elastic moduli of the metal material vary dramatically over temperature; the crystalline quartz or silicon made

structure allows the device overcome this problem. It also makes them small, inexpensive, and requiring few powers [24].

A further modification form the tuning fork gyro is the double fork gyro or the dual accelerometer gyro as shown in Fig. 2.3[25]. Similar to the tuning fork, the opposite proof masses vibrate in anti-phase on xz-plane and the Coriolis acceleration induced vibration appears in y-axis. The output amplitude of out plane vibration in y-axis is proportional to the rotation rate. The seismic masses are supported by beam-type suspension like accelerometer. The structure is usually driven electrostatically, piezoelectrically or electromagnetically. The out plane vibration is detected capacitively for the large area form the roof masses. Because of the similarity to the tuning fork gyroscope, they share many of the same advantages and disadvantages.

There are several types of micro-machined vibrating gyroscope that are conceptually similar to the conventional gyroscope. The first one is double gimbals vibrating gyroscope [26]. This device is fabricated with bulk micromachining to form the double gimbals as shown in Fig. 2.4. The outer gimbals is electro-statically driven at constant amplitude using the drive electrodes, and the inner gimbals synchronously vibrates along the stiff axis of the inner gimbals. When exposed to a rotation normal to the plane of the device, Coriolis force causes the inner gimbals to oscillate about its weak axis with a frequency equal to the drive frequency. The vibration of inner gimbals is detected by using the variable capacitance. Therefore, maximum resolution is obtained when the outer gimbals is driven at the resonant frequency of the inner gimbals, causing the signal to be amplified by the mechanical quality factor of the sense resonance mode of the structure. The out plane motion is strongly damped due to squeeze film effect and the Q factor decreases. Moreover,

the capacitively driving and detection may result in nonlinear motion from the gimbal frames.

Those above reported in the literatures are bulk-micromachined silicon-on-glass vibrating beams [27], vibrating membranes [28], and double-gimbaled structures [29] as demonstrated. Since the Young's modulus of single-crystal silicon changes with crystallographic orientation, symmetric vibrating structures made of single-crystal silicon may show excessive mechanical coupling between drive and sense modes due to the anisotropy, resulting in a large error with unacceptable drift characteristics [27]. Surface-micromachined vibratory gyroscopes have also been demonstrated. Some have been integrated with the readout electronic circuitry on a single silicon chip, reducing parasitic capacitances and hence increasing the signal-to-noise ratio. In addition, the vibrating structure is made of polysilicon, which has a high quality factor and an orientation-independent Young's modulus.

Single-axis polysilicon surface-micromachined vibrating gyroscopes have been realized at Berkeley [30,31] and Samsung [32–34]. Figure 2.6 depicts the schematic diagram for the z-axis vibrating gyroscope. The structure is compliant in two identical directions and driven to vibrate in sensing mode. When exposed to a rotation normal to the plane of the device, Coriolis force causes the vibration in sensing mode that is proportional to the rotation rate. Berkeley's z-axis vibratory rate gyroscope resembles a vibrating beam design and consists of an oscillating mass that is electrostatically driven into resonance using comb drives. Any detection that resulted from Coriolis acceleration is detected differentially in the sense mode using comb fingers. This device was integrated with a trans-resistance amplifier on a single die using the Analog Devices BiMEMS process. The remaining control and signal-processing electronics were implemented off-chip. Samsung has also

reported a very similar surface-micromachined z-axis device, shown in Fig. 2.5, with polysilicon resonating mass supported by four fishhook-shaped springs [33]. Hybrid attachment of the sensor chip to a CMOS application-specific integrated circuit (ASIC) chip used for readout and closed-loop operation of the device was done in a vacuum-packaged ceramic case.

The x-axis vibrating gyroscope, which is similar to z-axis vibrating gyroscope, has been demonstrated and reported at HSG-IMIT. It is a surface-micromachined precision x-axis vibratory gyroscope (MARS-RR) with a very small zero-rate output achieved by mechanical decoupling of the drive and sense vibration modes [35]. Figure 2.7 depicts the schematic diagram for the x-axis vibrating gyro. The structure is driven electro-statically with comb fingers to vibrate in rotary mode. When exposed to the rotation about x-axis, Coriolis force tilts the structure to vibrate along y-axis and the rotation is detected. This device, shown in Fig. 2.8, was fabricated through the standard Bosch foundry process featuring a 10- μm -thick structural polysilicon layer in addition to the buried polysilicon layer, which defines the sense electrodes.

The dual-axis vibrating gyroscope is reported at Berkeley [36], that a surface-micromachined dual-axis gyroscope based on the rotational resonance of a 2- μm -thick polysilicon rotor disk, as shown in Fig. 2.10 and the schematic diagram in Fig. 2.9. Since the disk is symmetric in two orthogonal axes, the sensor can sense rotation equally about these two axes. Also reported in this literature is a cross-shaped nickel-on-glass two-axis micromachined gyroscope [37].

The vibrating ring gyroscope is one subject of this proposal. General Motors and the University of Michigan have developed a vibrating ring gyroscope [38] as shown in Fig. 2.11. This device consists of a ring, semicircular support springs, and drive, sense, and balance electrodes,

which are located around the structure. Symmetry considerations require at least eight springs to result in a balanced device with two identical flexural modes that have equal natural frequencies [39]. The first micromachined version of the vibrating ring gyroscope was fabricated by electroforming nickel into a thick polyimide mold on a silicon substrate in a post circuit process [38-40]. To improve performance further, a new polysilicon ring gyroscope (PRG) [41] was recently fabricated through a single-wafer, all-silicon, high-aspect-ratio polysilicon trench-refill technology [42] at the University of Michigan. A similar design is developed by British Aerospace Systems & Equipment (BASE) as shown in Fig. 2.12 [43-45].

The vibrating ring structure has some important features compared to other types of vibratory gyroscopes. First, the symmetry of the structure makes it less sensitive to spurious vibrations. Only when the ring has mass or stiffness asymmetries induce a spurious response from the environmental vibrations. Second, two identical flexural modes of the structure with nominally equal resonant frequencies are used to sense rotation, and the detected signal is amplified by the quality factor of the structure, that resulting in higher sensitivity. Third, the vibrating ring is less temperature sensitive since the vibration modes are affected equally by temperature. Last, electronic balancing of the structure is possible. Any frequency mismatch due to mass or stiffness asymmetry that occurs during the fabrication process can be electronically compensated by use of the balancing electrodes that are located around the structure.

2.2 Principles

As reviewed in previous section, almost basic mechanism of those micro-machined vibrating gyroscopes is based on Coriolis force. The Coriolis force is a fictitious force that occurs in the accelerating reference frame. It is actually one component of the inertial force that arises from the accelerating system. In general, we can realize it with two relatively rotating frames under which the Coriolis acceleration is accompanied with centrifugal acceleration. The force that changes the motion of a particle arisen from the rotation frame is named after Gustave-Gaspard Coriolis in 1835. It also distinguishes the force from acceleration and gravity.

The simple pendulum swings along the oscillation surface and projects its path onto the frame as shown in Fig. 2.13. The frame is fixed and the projection path is a straight line on the fixed frame as depicted in Fig. 2.13(a). When the frame rotates, the path of the projection forms a leaf-like curve as shown in Fig. 2.13(b). It comes from the relative motion between the frame and the oscillation surface of the pendulum. If someone stay on the frame and observe the pendulum, he would think that there seems an extra “force” acts on the pendulum. In fact, it is the famous experiment demonstrated by Jean Bernard Léon Foucault. This experiment was demonstrated at Paris Observatory in 1851, which shows the earth rotates, and the pendulum is known as Foucault pendulum. The pendulum swing is changed by Coriolis force arisen form the relative frames rotation.

Figure 2.14 shows a simple case for demonstrating the Coriolis force. A particle moves with constant velocity along with positive x-axis independently above the rotating frame as shown in Fig. 2.14(a). The path projecting onto the frame forms a spiral curve as shown in Fig. 2.14(b). If

someone stay on the frame and observe the particle, he would think that there seems an extra “force” acts on the particle and cause it to rotate. The force is recognized as the Coriolis force. At any arbitrary instance that the spiral curve intersects with the x-axis, the velocity components along with the x-axis and y-axis are V_x and $-V_y$. The angular momentum is expressed as follows.

$$H = \vec{r}\vec{i} \times m\vec{V} = \vec{r}\vec{i} \times m(V_x\vec{i} - V_y\vec{j}) = -rmV_y\vec{k} = -mr^2\Omega\vec{k}, \quad (2-1)$$

where the V_y is the particle velocity relative to the frame in y-axis. For the particle moves farther out and the momentum increases, there must be a moment exerted. The moment is equal to the rate change of the angular momentum. The moment comes from the Coriolis force, which is in negative y-axis, is expressed as follows.

$$M = \vec{r}\vec{i} \times (-F_{Coriolis}\vec{j}) = -F_{Coriolis}r\vec{k} = \frac{dH}{dt} = -2m\Omega r \frac{dr}{dt} \vec{k}. \quad (2-2)$$

The radius change rate is equal to the particle moving velocity V_x that along with x-axis. For constant rotation rate, the Coriolis acceleration is represented as follows.

$$a_{Coriolis} = \frac{F_{coriolis}}{m} = 2\Omega \frac{dr}{dt}. \quad (2-3)$$

For two relative rotating frames, there seems to be extra force exerted to the object on the frames. The force tends to push the two coinciding points on different frames and causes them farther away. As shown in Fig. 2.14, the Coriolis force pushes the particle to the right with the respect of the frame. On the other hand, another force should be supplied to insure the particle moves synchronously with the frame. Figure 2.15 depicts the particle moves on the rotating frame with velocity in radius direction. The particle moves from point P to point P' and leaves the radius difference. With the respect of the absolute coordinate, there is velocity difference perpendicular to radius direction. There must be a

force, which makes the particle sticking on the rotating frame, or the particle would move far away from the initial coinciding point on the frame. From classical mechanics, the general motion of a particle relative to an arbitrary moving system is shown in Fig. 2.16[15]. The expression for the absolute acceleration of the point P is expressed as follows.

$$a = \ddot{R} + \dot{\Omega} \times r + \ddot{r} + \Omega \times (\Omega \times r) + 2\Omega \times \dot{r} , \quad (2-4)$$

where R is the position vector from the fixed system to the rotating system that rotates with Ω , and r is the particle position vector relative to the rotating system. The last term is known as the Coriolis acceleration and expressed as follows.

$$a_{Coriolis} = 2\Omega \times V . \quad (2-5)$$

It actually arises from two sources. One is the changing direction in space of the velocity of point P relative to the moving system. The other is the change rate of the frame velocity due to the changing magnitude or direction of the particle position vector relative to the moving system [15].

The concept of Coriolis force can be exactly mapped to the steady precession for the dynamics. We take a simple example as the illustration. Figure 2.17(a) shows a disk rotates along z-axis with angular rate ω . Those point along the y-axis travels with velocity V that is proportional to the radius. When the disk is exposed to the rotation of the rotation rate Ω , the corresponding Coriolis forces on every point of the disk result in a torque M along x-axis. We can also solve this by gyro dynamics and obtain the angular momentum H [14,48]. With the rotation angular rate ω in spin axis and Ω in precession axis, the resultant moment in couple axis is M_0 expressed as follows.

$$M_0 = \Omega \times H , \quad (2-6)$$

which is equal to the Coriolis force resultant torque M .

The basic mechanism for the conventional gyroscope is to setup a rotating body and its gimbals, then measure the induced moment to estimate the input rotation. By examining all design of the vibrating gyroscope as reviewed, the basic mechanism is to setup a vibratory body, then measure the responding torque or force to estimate the input rotation as depicts form Eq. (2-5). Equations (2-5) and (2-6) are conceptually equivalent. However, there is seems no other kind of design concept such as to provide fixed moment and to measure the response. The reason is that we provide a force or moment to the device and the devices will response such as linear velocity or angular velocity. It is similar to the conventional gyroscope design. Besides, it is relatively complex to make a rotating structure for the recent MEMS technologies. Therefore, all gyroscope designs are based on similar concept.

Mathematically, the motion of a vibration system can be modeled in terms of so-called normal mode. In this mode, the system is represented by independent spring and mass oscillation system. For each mode for the system, the energy is stored in specific mode and isolated with each other [46]. Unless the damping or rotation exists, the vibration for one mode will not induce the coupled vibration in the other mode. As the ideal Foucault pendulum, the governing equation is expressed as follows.

$$\begin{cases} \ddot{x} - 2\Omega\dot{y} + \omega^2 x = 0 \\ \ddot{y} + 2\Omega\dot{x} + \omega^2 y = 0 \end{cases} \quad (2-7)$$

where x is the amplitude of the pendulum swing along the x-axis, y is the amplitude of the pendulum swing along the y-axis, Ω is the rotation rate about z-axis, and ω is the natural frequency of the vibration of the pendulum [16]. Without exposed to the rotation about z-axis, the governing equation as expressed in Eq. (2-7) can simply be taken as two independent systems. With the rotation, the vibrations for the two axes influence each other. The degree of the influence stands for the rotation

or rotation rate. The rotation sensing principles of the vibrating shell gyro was first analyzed by G. H. Bryan in 1890 [65]. For the conventional gyroscope or those MEMS gyroscopes as reviewed, the basic design concept for the structure is to setup two identical frames. Generally, the two frames are perpendicular with each other in physical space that is trivial in sense. A structure, which is designed to employ two orthogonal frames, also follows the basic concept. The vibrating ring follows the basic concept and is the subject of analysis of this dissertation. The principle of a vibrating ring gyroscope is discussed in the following chapter.



Chapter 3 Structural Design

The structural design of the motion sensor discussed in this chapter includes deriving the governing equations of a vibrating ring, symmetric analysis of supports, and calculation of natural frequencies of the structure. The structure design proposed in this dissertation is based on a vibrating ring gyroscope. The structure of vibrating ring gyroscope is consisted of the main ring and supports. Deriving the governing equations of a vibrating ring helps to understand the mechanism of a vibrating ring gyroscope and requirements in designing structure. The influence of the geometric symmetry for supports is discussed in this chapter. It reveals that proper design for the support yields both rotational symmetry and mirror symmetry. To obtain high quality factor, the natural frequency of the structure is calculated.

3.1 Vibrating Ring Gyroscope

Figure 3.1(a) depicts the circular ring and the displacement is denoted as radial displacement u and tangential displacement v [47]. For general case for the flexural in-plane vibration, the displacement is represented in the form of trigonometric series. Assume that the elongation of the central line of the ring remains constant in the flexural mode. The radial and tangential displacements are expressed as follows.

$$\begin{aligned}
u &= \sum (a_n \cos n\theta + b_n \sin n\theta) \\
v &= \sum \left(-\frac{a_n}{n} \sin n\theta + \frac{b_n}{n} \cos n\theta\right),
\end{aligned} \tag{3-1}$$

where a and b are functions of time, and n denotes the number of modes [28]. These terms, $\cos n\theta$ and $\sin n\theta$, are orthogonal on the interval $0 \leq \theta \leq 2\pi$. The designed structure is a complete ring, such that one time function is independent of the others. The figure 3.1(b)-(f) show the shape for different modes. The potential energy of bending and the kinetic energy of vibration for the entire ring are expressed as follows.

$$\begin{aligned}
V &= \frac{EI}{2r^4} \int_0^{2\pi} \left(\frac{\partial^2 u}{\partial \theta^2} + u\right)^2 r d\theta \\
T &= \frac{\rho A}{2} \int_0^{2\pi} (\dot{u}^2 + \dot{v}^2) r d\theta,
\end{aligned} \tag{3-2}$$

where ρ is ring's density; t is ring's thickness; w is ring's width; E is Young's modulus of the material, and I is its moment of inertia. The differential equation of motion is obtained by using Lagrange's equation, and the coefficient a_n and b_n are taken as the generalized coordinates. For the orthogonalization from the trigonometric series, the differential equations of motion are expressed as follows.

$$\begin{aligned}
\ddot{a}_n + \frac{EIn^2(1-n^2)^2}{\rho Ar^4(1+n^2)} a_n &= 0 \\
\ddot{b}_n + \frac{EIn^2(1-n^2)^2}{\rho Ar^4(1+n^2)} b_n &= 0.
\end{aligned} \tag{3-3}$$

These coefficient a_n and b_n are obviously independent with each other. If we take the motion of the ring as superposition of the n -th mode vibrations, the set of coefficient can be used as the coordinates to express the motion. For example, those modes of the two 2nd mode vibrations for the ring are shown in Fig. 3.2(a). The motion of the ring can be expressed

with a_2 and b_2 instead of describing the ring mode shape with $\cos 2\theta$ and $\sin 2\theta$, because a_2 is coincident with $\cos 2\theta$ and b_2 is coincident with $\sin 2\theta$. This expression can be expanded to n-th mode.

Figure 3.2(b) shows a ring vibrates with 2nd mode and lies on 0 degree axis. Simply divided into four sector and there is a velocity for each sector. When the ring is exposed to a rotation, the Coriolis force is induced on the ring and the resultant force lies on 45 degree axis as shown in Fig. 3.2(c). For the ring, the primary mode lies on 0 degree axis and the secondary mode on 45 degree axis, that they are independent from each other. Mathematically, the orthogonal function from $\sin 2\theta$ is $\cos 2\theta$ rather than other $\cos n\theta$ that n is not equal to 2. Thus, the Coriolis force induced vibration from the primary mode will exactly lies on the secondary mode for the ring. The vibrating ring gyroscope is inherent from ring structure that yields two identical axes. When the structure is exposed to the rotation, the Coriolis force induces the vibration from one axis to another. The rotation can be obtained by measuring the response of the induced vibration, which follows the design concept of gyroscope.

Considering the general motion of a vibrating ring, Fig. 3.3 depicts the coordinate system of the motion sensor, including the inertial coordinate, the translating and rotating coordinate and the sensor coordinate. The sensor translates, without rotation, relative to a translating and rotating frame, which moves relative to a fixed inertial coordinate, where \vec{r}_1 specifies the position vector from inertial coordinate to the translating and rotating coordinate and \vec{r}_2 specifies the position vector from the frame to the sensor. The sensor is taken as a vibrating ring with a radius of r_3 . The vibration of the main ring includes radial and tangential displacements denoted as u and v , respectively, as defined in

Eq. (3-1). The potential energy of bending and the kinetic energy of vibration for the entire ring are obtained similar to Eq. (3-2).

Lagrange's equation, taking a_2 as a generalized coordinates yields the differential equation of motion as follows.

$$\begin{aligned} & \frac{5}{8}m\ddot{a}_2 - m\Omega_z\dot{b}_2 - \frac{1}{2}m\dot{\Omega}_z b_2 + \frac{9\pi EI}{r_3^3}a_2 \\ & + \left(\frac{5}{16}ma_2\Omega_x^2 - \frac{5}{16}ma_2\Omega_y^2 - \frac{5}{8}ma_2\Omega_z^2\right) \\ & + \left(\frac{3}{8}mr_3\Omega_x^2 - \frac{3}{8}mr_3\Omega_y^2\right) = f_{a_2} \end{aligned} \quad (3-4)$$

This equation governs the second mode of flexural vibration of the ring, as depicted in Fig. 3.4. The detection of rotation depends on the second mode. This expression involves the centrifugal force associated with a_2 and r_3 . In this work, these terms are made relatively small by designing the structure with a high effective stiffness, which affects the flexural vibration [107]. Besides, those terms associated with r_3 will not appear in the higher order vibrations, such as the third mode. A higher order vibration may be a solution when a low stiffness and a large radius are required.

Considering Eq. (3-2), using *Lagrange's equation*, and taking a_1 as the generalized coordinate, yield the differential equation of motion is expressed as follows.

$$\begin{aligned} & m\ddot{a}_1 - (2m\Omega_z\dot{b}_1 + mb_1\dot{\Omega}_z) + (m\Omega_x\Omega_y b_1 - ma_1\Omega_z^2 - ma_1\Omega_y^2) \\ & + m\ddot{x} - (2m\Omega_z\dot{y} + my\dot{\Omega}_z - 2m\Omega_y\dot{z} - mz\dot{\Omega}_y) \\ & + (mz\Omega_x\Omega_z + my\Omega_x\Omega_y - mx\Omega_z^2 - mx\Omega_y^2) = f_{a_1} \end{aligned} \quad (3-5)$$

where x , y and z are relative position vectors of the sensor in the translating and rotating frame, and a_1 and b_1 represent the rigid body motion of the ring. This equation governs the first mode of flexural

vibration of the ring, as depicted in Fig. 3.4. The detection of linear acceleration depends on the first mode. In the first row of Eq. (3-5), the centrifugal terms are smaller than other terms on micro scale. The last two rows in Eq. (3-5) represent the rigid body motion of the sensor. They can be shifted to the right of the equation and considered as part of the applied force.

3.2 Symmetry

The structural design of the motion sensor is determined with reference to both rotation and acceleration. The structure consists of the main ring and the supports. The influence of the symmetry on the support is discussed. The first design consideration of the support is the function for a gyroscope. The 2nd mode vibration of the ring is the desired mode shape as shown in Fig. 3.2(b) and Fig. 3.2(c), because it is relative simple to those flexural vibrations that are capable of detecting rotation. The main ring surrounded by four asymmetric supports, as shown in Fig. 3.5(a), is the simplest arrangement for the gyroscopic function. Those supports are placed in directions a_2 and b_2 , such that the structure is equally stiff in these directions. The supports placed at opposite position are identical, without which the mass center of the structure involves the plane motion when the structure vibrates. However, two second modes of vibration of the structure are not exactly at 45 degrees to each other and their natural frequencies are different. The structure exhibits planar motion when it vibrates, causing extra energy loss. The deformation of the support is not uniform, generating noise that affects detection. Thus, the supports should be placed as presented in Fig. 3.5(b), with rotational symmetry denoted by C_8 [49]. This arrangement yields a balanced device

with two modes that have the same natural frequency [46] at 45 degrees to each other.

But it does not fit the requirement of accelerometer. The centrifugal force and Coriolis force are generally applied simultaneously. Figure 3.6 (a) shows the structure deformed due to the linear acceleration along x-axis. As the asymmetry of the support, it employs non-collinear relationship between force and displacement. It affects to the structure though placed with rotational symmetry arrangement. Under linear acceleration, the structure deformation contains both linear displacement and rotational displacement as shown. For the bending moment on the attaching point between ring and support, the ring does not hold circular shape. In fact, for a motion sensor, it is unavoidable to expose to acceleration. Figure 3.6 (b) shows the force response with force applied at one point positive to x-axis on the structure. It also employs non-collinear relationship between force and displacement. By integrating with the electronic circuit, it is common to apply force to the structure for closed loop control. A feedback control loop may be used to rebalance those phenomena, but the design of control loops is complicated. Fortunately, those effects are not very serious on the micro scale, yet they cause undesired noise. Besides, asymmetric supports induce much more stress on the connection between the main ring and the supports than that of the symmetric supports.

Those phenomena come from the asymmetry of the support and can be described mathematically. A semi-circular model is taken as the example. Similar to the model for the full ring, the potential energy of bending and the kinetic energy of vibration for the semi ring are expressed similar as Eq. (3-2). The boundary of integration is from 0 to π for the half circle. Because the orthogonalization of the trigonometric

series does not hold for semicircle, the potential energy of bending and the kinetic energy of vibration for the semi ring are expressed as follows.

$$\begin{aligned}
 V &= \frac{EI}{r^3} \frac{\pi}{2} \sum_{n=1}^{\infty} (1-n^2)^2 (a_n^2 + b_n^2) + \sum F(i, j) a_i b_j \\
 T &= \frac{1}{2} \pi r \rho A \sum_{n=1}^{\infty} \left(1 + \frac{1}{n^2}\right) (\dot{a}_n^2 + \dot{b}_n^2) + \sum G(i, j) \dot{a}_i \dot{b}_j,
 \end{aligned} \tag{3-6}$$

where $F(i, j)$ and $G(i, j)$ represent the coupled terms of coordinates. By using Lagrange's equation and take a_n as the generalized coordinate, the differential equation of motion is expressed as follows.

$$\pi r \rho A \left(1 + \frac{1}{n^2}\right) \ddot{a}_n + \frac{EI\pi}{r^3} (1-n^2)^2 a_n + \sum g(i, j) \ddot{b}_j + \sum f(i, j) b_j = 0. \tag{3-7}$$

This result is different from Eq. (3-3) for those generalized coordinate a_n and b_n are no longer independent from each other. Obviously, the corresponding equation of motion with respect to a_n would appear with the coupled terms of b_j , that the state of a_n would be affected by b_j . As shown in Figs. 3.6(a) and 3.6(b), the displacement along with a_2 is accompanied with displacement in other axis. Besides, it causes the natural frequency of the mode is state dependent that will make many problems for sensing and driving. If the natural frequency drifts from the desired driving frequency, the quality factor may change that makes the signal scaling differs from normal value. A coordinate transformation is required to gather a better and simpler description for the motion. Practically, the transformation is not always the same due to the manufacture error. A higher degree of symmetry of the structure presents better performance. Figure 3.7 depicts the structure that contains symmetric supports. The structure is both mirrors symmetric and rotationally symmetric, and the degree of symmetry is denoted as D_4 . This structure is originally designed by Y. Cheng [56]. The shape of the

support is the same as that of the main ring, simplifying the estimation of the dynamic response. As expected, two modes are 45 degrees to each other as shown in Figs. 3.8(a) and 3.8(b). This structure exhibits a collinear force-displacement relationship, and is insensitive to those defects described above. The mirror symmetry of the structure facilitates the design of the rebalance loops that compensate for accelerations. The compensating voltage is proportional to the acceleration, so the structure can be used as an accelerometer. The symmetry of the structure, on which the use of the sensor as a gyroscope and accelerometer depends, is both rotational and mirrors symmetry.

Figures 3.8(a) and 3.8(b) depict the detection scheme used to measure the rate of rotation. The fixed amplitude of the primary mode is driven in a_2 and the Coriolis force induces a response in the form of the secondary mode in b_2 . Figures 3.8(c) and 3.8(d) present the detection scheme for sensing acceleration. The opposing support rings are displaced equally when the structure is accelerated. The difference between the induced signals of the displacements of the opposing support rings represents the linear accelerations.

3.3 Natural Frequency

For many microstructures such as MEMS, vibrating at its natural frequency is necessary to obtain higher quality factor when it involves the motion detection. The calculation for the natural frequency is important to our structure, because the basic mechanism for the motion sensor proposed in this dissertation is based on the vibrating ring. The resonant frequency of the structure, in principle, is the working point of the electronic circuit of the sensor. According the frequency, we design the corresponding circuits, and relative performance would be affected.

Designing the circuit with an excessively high frequency raises many problems, such as the band limitation of an operational amplifier. The procedure we calculate the resonant frequency of the structure is separating the structure into three parts, finding out the resonant frequency of each part individually, and calculating the composite resonant frequency. Considering the second mode, we separate the structure into the main ring, extending support rings and rotating support rings. The similarity between the main ring and the supports simplifies the calculation. Table 1 lists the mode and natural frequency of separated parts of the structure.

Problematically, the natural frequency of the rotating support ring is not close to ω_1 . Accordingly, the frequencies of the two modes close to ω_1 , with similar boundary conditions, are estimated. The exact frequency is determined using two concepts. The first is to weight the effective mass. The mode of vibration of a composite structure should be similar to that of a substructure with a greater effective mass. In the design proposed here, the effective mass of the main ring is weighted more heavily and the mode of the structure is close to that of the main ring. The extending support rings are also heavily weighted. Hence, the natural frequency of the structure should be between ω_1 and ω_2 . The second concept is the impedance for each mode. The impedance of a mass-spring system is expressed as follows.

$$Z = \left| \frac{F}{X} \right| = |K - M\omega^2|. \quad (3-8)$$

The natural frequency of the structure is assumed to be ω_1 . The impedances of the two modes are expressed as follows.

$$\begin{aligned} Z_3 &= 0.105M\omega_1^2 \\ Z_3' &= 0.53M\omega_1^2 \end{aligned} \quad (3-9)$$

Clearly, Z_3' is about five times Z_3 . The authors believe that the natural vibration of the structure must be efficient. Thus, the mode associated with Z_3 should be the desired mode of the rotating support rings.

The natural frequency of the structure is determined by adding the total kinetic energy and the total potential energy. The natural frequency of the structure ω is expressed as follows.

$$\omega \cong 1.048\omega_1. \quad (3-10)$$

This frequency is close to ω_1 and the mode is very similar to the second mode, and so the requirements are satisfied.

Table 2 compares the numerical and theoretical results, and the errors between these results are less than 5%. The structure is modeled by quadrilateral shell elements, and the type of the element is Shell63. The maximum elements used reaches 50000. Figure 3.9 shows the part view and full view of the meshed structure. The natural frequency of the second mode of the silicon structure is 22823Hz. Figure 3.10 shows those relative modes. Figure 3.10(a) shows the rotation mode. Figure 3.10(b) shows the first vibration mode, and it is also plane motion mode. Figure 3.10(c) shows the second vibration mode, and Fig. 3.10(d) shows the third vibration mode.

Chapter 4 Electronics Circuit

The electronics discussed in this chapter includes the electrostatic force driving circuit and the detection circuit. The detection modes including the open loop mode and force-to-rebalance mode are discussed. The driving circuit to force the structure to vibrate at the natural frequency is implemented with the phase locked loops. Electrostatic force is commonly used for MEMS devices [55]. The variable capacitor, formed by ring structure and electrode, provides both driving scheme and detection scheme, which takes advantage on the electrostatic force.



4.1 Interface

Electrostatic force is commonly used as the force source for the MEMS device. Variable capacitor and comb drive are the most commonly used mechanisms [55]. Variable capacitor is used in this work, and the capacitor is formed between the support ring and the electrode as shown in Figs. 4.1(a) and 4.1(b). Figure 4.1(a) shows the top view of structure with electrodes. The electrode locates inside the support, and the gap exists between the electrode and the support as shown in Fig. 4.1(b). When the voltage difference exists between the electrode and support, a capacitor is formed. The attraction of the charge in the capacitor provides the electrostatic force. Because the gap is relative small to the structure, the electrostatic force is taken as the force between the two parallel plates. The electrostatic force is expressed as follows.

$$F_{electrostatic} = -\varepsilon A \frac{V^2}{d^2}, \quad (4-1)$$

where ε is permittivity, A is the effective area, V is the applied voltage, d is the gap width between support and electrode, and negative stands for the electrostatic force is always attractive. The shape for the electrode is quarter circle on the opposite, because it makes greater effective displacement between electrode and support for the second mode of vibration of a ring. When the electrostatic force is applied to the structure, the balance equation is expressed as follows.

$$kx = -\varepsilon A \frac{V^2}{(d_0 + x)^2}, \quad (4-2)$$

where k is the structural stiffness, d_0 is the neutral gap width between the support and electrode and x is the structure displacement away from the neutral point. There three solutions imply three intersects shown as Fig. 4.2. The left intersect stands for an unreasonable solution. The middle one stands for an unstable solution and the structure is close to the electrode which is rarely achieved under general condition. The right one stands for the stable solution. Applying different voltage to the electrode changes the position of these intersects. Applying too high voltage causes the structure sticks to the electrode, and the voltage is so-called pull-in voltage. This voltage for the designed structure presented in this dissertation is 51 Volt in theory. Applying a simple sinusoidal wave to the electrode will cause the structure vibrating at the doubled-frequency. The desired input voltage is expressed as follows.

$$(1 + \sin \omega t)^2 = 2 \sin \omega t + \frac{3}{2} + \frac{-1}{2} \cos 2\omega t. \quad (4-3)$$

The doubled-frequency term is ignored because this frequency is far from the natural frequency of the structure.

When the electrostatic force is used to drive the structure, the voltage indicates the structural displacement. When the electrostatic force is used to detect the structural displacement, the structural displacement does not proportionally indicate the various voltages. The relative detection circuit should be concerned additionally, and the affect of detection circuit to the detected signal should be as small as possible. It is sure that structural displacement changes the capacitance between structure and electrode. The capacitance is expanded in Taylor series expressed as follows.

$$C = \varepsilon AV^2 \left(\frac{1}{d_0^2} + \frac{-2}{d_0^3} \cdot x + \frac{6}{d_0^4} \cdot x^2 + \dots \right). \quad (4-4)$$

Take x as small displacement and ignore the high degree terms, the capacitance difference is expressed as follows.

$$\Delta C = C_0 \cdot \frac{-2x}{d_0}, \quad (4-5)$$

where C_0 is the static capacitance expressed as $\frac{\varepsilon AV^2}{d_0^2}$.

Consider the detection circuit connect to the variable capacitor, the circuit can be represented as an impedance as shown in Fig. 4.3. If the impedance is simply taken as a resistor, the governing equation is expressed as follows.

$$C\dot{V}_{out} + \left(\dot{C} + \frac{1}{R} \right) V_{out} = \dot{C} V_i, \quad (4-6)$$

where V_{out} is the detected signal, V_i is the structure voltage, C is the variable capacitor and R is the effective resistance. This equation is a nonlinear equation. Through numerical analysis, the circuit shears similar phenomenon with a high pass filter. It means the resistance should be large enough to avoid rejecting low frequency signal. Besides, if the

capacitor is connected to an operational amplifier, the DC signal is possible missed.

Figure 4.4(a) shows the schematic diagram of the detection scheme. A fixed voltage reference feeds to two capacitors, C1 and C2, and the divided voltage feeds to a buffer amplifier. The output voltage is the function of capacitance. The change on C1 or C2 causes the variance of the out voltage. The replacement of C2 to a variable capacitance on structure makes the output voltage yields the displacement of the structure. The output voltage is express as follows.

$$V_o = \frac{C1}{C1 + C2} V_i, \quad (4-7)$$

where V_o is the output voltage, and V_i is the input voltage. Typically, the output voltage remains constant value without other disturbance as the line one shown in Fig. 4.4(b). However, the existence of input bias current for the practical op-amp causes charge in the capacitors doesn't remain conservation. It leads to the drift of output voltage to the power supply rail [56]. The current leakage doesn't affect large capacitance, because the quantity of charge leakage is not comparable with the total charge in the capacitance. The capacitance for MEMS devices is relative small to the ordinary electronic circuit. One picofarad to hundred femtofarad of capacitance is commonly designed for MEMS. The input bias current of op-amp greatly affects the output voltage at this scale level as shown in Fig. 4.2(b). The output voltage is expressed as follows.

$$V_o = \frac{Q_0 - i_L \cdot t}{C1 + C2}, \quad (4-8)$$

where Q_0 is the initial charge in the capacitance, and i_L is the bias leakage current. It causes the signal DC distortion, and the output voltage obviously drifts to the lower power rail. The ultra-low input bias current op-amp is one possible solution. However, at the level of 10 femtoampere

current leakage still affects the signal too much, and the op-amp achieves femtoampere bias current is too much expensive.

Taking the negative power rail V^- as the steady-state value of the non-inverting input of the op-amp, the variable capacitance induced output voltage for a time period of the variation is expressed as follows.

$$\Delta V = \frac{(V^-) \frac{\varepsilon A}{d + \Delta d} \cdot \frac{\Delta d}{d} + i_L \frac{2\pi}{\omega}}{-C1 + \frac{\varepsilon A}{d + \Delta d}}, \quad (4-9)$$

where ω is the variation frequency of the capacitance, d is the static gap of C2, and Δd is the gap difference. The output voltage is induced by capacitance variation and charge leakage. The later term is neglected with high variation frequency that can achieve with 10KHz for a popular op-amp such as TL061. With relative small quantity of C1, the output voltage induced by the variation is expressed as follows.

$$\Delta V = (V^-) \frac{\Delta d}{d}.$$

(4-10) The voltage plot is shown in Fig. 4.5(a). For practical op-amp, the existence of the stray capacitance, as shown in Fig. 4.5(b), ruins the linearity of the expression. The stray capacitance is not negligible at this scale, and this detection method suffers from the stray capacitance. In fact, the interconnection for structure and detection circuit may induce many undesired condition including the stray capacitance, and it certainly happens.

Switching capacitor circuit is often used readout circuit for the variable capacitance detection [57-61]. The basic schematic diagram is shown as Fig. 4.6(a) [62]. The capacitors are arranged with op-amp and the applied voltage of the capacitance is switched by MOSFET. The output voltage is expressed as follows.

$$V_o = -V_i \frac{C1}{C2}. \quad (4-11)$$

Figure 4.6(b) depicts a modified design that is insensitive to the stray capacitance to the substrate [64]. Though the capacitor connects to the op-amp, the effect of charge leakage due to the input bias current is neglected. During the phase of $\bar{\phi}$ as depicted in Fig. 4.6(a), the capacitor C2 is recharged. With high switching frequency, the effect of charge leakage is eliminated. For the desired application in this work, the variable capacitor can be placed as C1 or C2 in the circuit. The position of C2 is preferred for it performs linear relation. But, the voltage across the variable capacitor is time-various, that will cause much noise. If the variable capacitor is placed at C1, it performs non-linear relation. Integrating with the sampling technique, the switched-capacitor is often used to develop the digital readout technique such as for pressure sensor [65] and accelerometer [66]. The relative circuit or a microprocessor for this method is required. Some drawback of the switched-capacitor has been reported, such as the charge-injection of the MOS switch [67,68], the effect of drain-source leakage [69], and clock feed-through [70]. The timing of clock also should be designed carefully [71]. Nevertheless, the switched-capacitor is widely used in readout circuits, because it provides great potential to integrate with digital circuits.

An interface circuit to measure the capacitive transducer that is based on current mirror is developed by W. H. Ko and G. J. Yeh [74]. The first feature of this circuit is insensitive to the stray capacitance for the architecture is based on the same level to ground or somewhat network. The other feature is the sensitivity and null point of the output voltage is controlled independently by two voltage sources. This method is CMOS integrated, and it basically suits for the surface micromachining for MEMS. The process used in this work is classified as bulk

micromachining. The on-chip amplifier integrated with the bulk micromachining process requires further developed.

Figure 4.7(a) shows the capacitive measurement used takes advantage on NMOS source follower. The structure is pulled to fixed voltage reference V_i . With the structural vibration, the capacitance between the ring and electrode is various from the static capacitance C . It induces charge flow out to the loading resistor R and NMOS gate. For high input impedance of the MOS gate, the charge flows through the loading resistor. It causes a voltage difference on the gate of the NMOS and expressed as follows.

$$\Delta V \propto \frac{\Delta C \cdot V_s}{T} R = V_s \cdot \Delta C \cdot f \cdot R, \quad (4-12)$$

where V_s is the static voltage at gate of MOS, T is the time period of the structural vibration and the same with the variation of capacitor, f is the vibration frequency, and R is the loading resistance. The voltage difference is relative small to the static voltage. The total voltage feeds to the NMOS source follower as shown in Fig. 4.7(b), and the level shifter is added for eliminating the static voltage and magnifying the voltage difference. The level shifter inverts the input signal, and another inverter can be used if required. The similar scheme is used for many MEMS device detection circuit [75,76]. The input bias current always exists that leads the DC level to the rail voltage of the source follower or operational amplifier. Compensating the bias current by using the reverse-bias current of a diode is one solution. It's inconvenient for using different types of amplifier. Moreover, the existence of the internal resistance in the detection circuit as shows in Fig. 4.8(a) will lead to a kind of low frequency periodical disturbance to the out signal as shows in Fig. 4.8(b). This may be induced by the common mode effect of the MOSFET M2

and M3. Switching-capacitors circuit can be a solution; however the circuit is relatively complex.

4.2 Control Loops

Figure 4.1 presents the top and detailed views of the structure of the sensor. The main ring in the center is the main body designed to vibrate in the flexural mode. Figure 4.9 indicates how the main ring is connected to eight support rings that surround it. The main ring and the support rings are designed to vibrate in the plane, as depicted in Fig. 3.8. Electrodes are located at the centers of the support rings, as shown in Fig. 4.1, forming capacitors and driving the structure. The potential difference between the support ring and the electrode generates an electrostatic force that attracts them toward each other, and drives the structure to vibrate. The electrodes are shaped to maximize effective displacement when the structure vibrates in the desired modes of vibration.

Figure 4.9 schematically depicts the control loops that are used to manipulate the sensor. The main driving loop causes the structure to vibrate as desired. The vibration is enhanced by phase-locked loops, and the structure vibrates at the resonant frequency to yield large amplitudes [27]. A rebalancing loop is designed to rebalance the vibration induced by the Coriolis force. Two detection loops are designed to balance the vibration induced by linear motion. Three loops cooperate to balance the planar motion.

4.3 Driving Circuit

The system damping ratio is an important index of the performance of a micro electromechanical system (MEMS) or any system that exhibits

resonance. The Q factor is the reciprocal of the damping ratio. With a high Q, the measurement signal of the system response can be effectively magnified. However, the damping ratio can never be easily determined in practice, especially when the excitation frequency from the driving circuit is as high as 20K Hz. The phase difference between output and input signals depends on the system's parameters. Those of a mechanical system are effective mass, effective stiffness, and system damping; for an electronic circuit, they are equivalent inductance, capacitance, and resistance. Evaluating the input/output relationship, including phase difference, identifies the system's parameters. The phase locked loop (PLL) is extensively used in the modulation/demodulation circuits [77-79]. It provides a fixed phase error between output and input signals, locking the frequency and phase. Typically, the phase difference between the output and input of a PLL is $\pi/2$. The phase difference of a second order system without damping is $-\pi/2$ when the system is driven at its natural frequency [80]. The natural frequency can be obtained when a PLL is the driving circuit of a second order system [81,82]. In practice, the system always contains the damping component, which shifts the tracking frequency from the natural frequency. Thus, measuring the tracking frequency reveals the damping ratio.

As well as determining the parameters of a system, the method proposed can be used in the following applications. The phase locked loop can be used as the driving circuit for a system. As shown in Fig. 4.10(a), the microstructure is obtained from finite element analysis software, Ansys5.3. The PLL module is used as the driving circuit. Appropriately setting the gain of the voltage-controlled oscillator (VCO) causes the tracking frequency to approach the natural frequency. The natural frequency of the system, especially for MEMS, possibly changes for several reasons, such as manufacturer's error or operating

environment. Figure 4.10(b) shows the silicon structure etched by reactive ion etching (RIE), and captured using microscope (10 x 5). The RIE process yields different structure width because various gap dimensions are required between the structures [84]. It causes shifting and splitting of the resonant frequency [85]. In practice, no two devices have the same natural frequency. Almost every kind of device suffers thermal problems that also influence the natural frequency [86]. The scheme proposed here eliminates the effect of the shifting of resonant frequency.

Notably, this scheme can be easily merged into the design of control circuit of the system. The circuit can be used not only to drive the system, but also to test it. Identifying the system's parameters for microstructure of MEMS presents many problems. The signal can be measured using a network analyzer, such as an HP 35670A. However, in mass production, an efficient method to measure the system parameters is required. Furthermore, the microstructure is typically packaged, making measurement more difficult. Military and transportation applications usually require self-testing functions. Merging PLL into the system enables the testing functions. The internal testing circuit supports both testing during manufacture and self-testing during operation. The internal circuit should have a testing mode, so that no extra circuit is required for testing.

Consider a second order system, the governing equation is shown as follows.

$$a_2\ddot{X} + a_1\dot{X} + a_0X = F \sin \omega t, \quad (4-13)$$

where a_2 is effective mass, a_0 is effective stiffness, F is applied signal, ω is driving frequency, and a_1 is system damping. The particular solution is expressed as follows.

$$X = A \sin(\omega t - \theta), \quad (4-14)$$

where A is the amplitude, and θ is the phase lag. The phase lag is expressed as follows.

$$\theta = \tan^{-1}\left(\frac{2\zeta\omega / \omega_n}{1 - \omega^2 / \omega_n^2}\right), \quad (4-15)$$

where ζ is the damping ratio, and ω_n is the natural frequency [80]. With fixed input and output signals as shown in Fig. 4.11(a), the input signal and output signal are modulated as follows.

$$\sin(\omega t - \theta) \cdot \sin(\omega t) = \frac{1}{2} \cos(-\theta) - \frac{1}{2} \cos(2\omega t - \theta). \quad (4-16)$$

Using the loop filter, simply as low pass filter yields a modulated signal is shown as follows.

$$\sin(\omega t - \theta) \cdot \sin(\omega t) \cong \frac{1}{2} \cos(-\theta). \quad (4-17)$$

Consider a driving frequency ω , close to the natural frequency ω_n . Replace ω / ω_n with α in the first few terms of the Taylor expansion in Eq. (4-17) as follows.

$$\frac{1}{2} \cos(-\theta) = \frac{1}{2} \left\{ -\frac{1}{\zeta} (\alpha - 1) + \frac{1}{2\zeta} (\alpha - 1)^2 + \frac{1 - \zeta^2}{2\zeta^3} (\alpha - 1)^3 + \dots \right\} \quad (4-18)$$

When α is around a, Eq. (4-18) could be approximated as follows.

$$\frac{1}{2} \cos(-\theta) = -\frac{1}{2} \cdot \frac{1}{\zeta} (\alpha - 1). \quad (4-19)$$

In the steady state, the filtered signal is fed into the voltage-controlled oscillator (VCO) and the output frequency of VCO is shown as follows.

$$\omega = \omega_0 + K_{VCO} \cdot \frac{1}{2} \cos(-\theta), \quad (4-20)$$

where ω_0 is the initial frequency of VCO, and K_{VCO} is the VCO gain. The output signal of VCO is fed back to the modulator and is fed into the plant. Equation (4-20) yields the steady state of frequency as follows.

$$\frac{\omega}{\omega_n} = \frac{\omega_0 + K_{VCO}/2\zeta}{\omega_n + K_{VCO}/2\zeta} \quad (4-21)$$

Thus, if $K_{VCO}/2\zeta$ is sufficiently large, the tracking frequency is close to the resonant frequency. Measuring the tracking frequency yields an estimate of the damping ratio as follows.

$$\zeta = \frac{1}{2} \cdot \frac{K_{VCO}}{\omega_n} \left(\frac{\omega - \omega_n}{\omega_0 - \omega} \right) \quad (4-22)$$

Moreover, ω_n may be unknown or should be checked. We could set different initial frequency as ω_{01} and ω_{02} ; therefore, different tracking frequency, ω_1 and ω_2 could be obtained. The resonant frequency and damping ratio can be estimated as follows.

$$\omega_n = \frac{\omega_{01}\omega_2 - \omega_{02}\omega_1}{\omega_{02} - \omega_{01} + \omega_1 - \omega_2} \quad (4-23)$$

$$\zeta = \frac{K_{VCO}}{2} \cdot \frac{\omega_1 - \omega_2}{\omega_{02}\omega_1 - \omega_{01}\omega_2} \quad (4-24)$$

Equation (4-21) states that the tracking frequency ω approaches ω_n , if K_{VCO} is sufficiently large. Equation (4-22) leads to an estimate of the damping ratio for various VCO gains, at fixed ω_n and ω_0 . As shown in Fig. 4.12(a), the damping ratio was set to 1, and the estimated damping ratio was varied by applying different values of K_{VCO} . Figure 4.12(a) clearly shows that a larger K_{VCO} corresponds to an estimated damping ratio closer to the set damping ratio. The damping ratio was set to 0.01, and the results shown in Fig. 4.12(b).

The system's natural frequency ω_n can be estimated, if required. Applying different VCO initial frequencies, ω_{01} and ω_{02} yields two tracking frequencies ω_1 and ω_2 . Thus, the natural frequency can be estimated from Eq. (4-23), as shown in Fig. 4.12(c). The set natural frequency is 1000Hz at a damping ratio of 0.01, and the estimated natural frequency is close to 1000Hz at the larger VCO gain. Theoretically, the tracking frequency is relative close to the natural frequency with large VCO gain setting. In practice, the VCO gain should not exceed 10^6 . In fact, 10^3 to 10^4 is acceptable. A VCO gain that is too high causes numerical errors in the simulation.

The experiment involves an electric circuit. An inductor, resistor and capacitor are used to emulate a second-order plant. The voltage signal, fed into the VCO module, stands for the driving frequency. Thus, the 8051 module is added to read the voltage as a data readout processor. Figure 4.11(b) shows the equipment.

The theoretical natural frequency, ω_n , of the plant is a function of both the inductance and the capacitance. Though the parameters of the passive components are not accurate, they still provide information to indicate the natural frequency of the plant. For practical components with quantitative errors, the system damping ratio is determined by measuring relationship between the input and output using a network analyzer, as shown in Fig. 4.13(a). Various resistances were set to yield different damping ratios. Table 3 presents the identification data.

Equations (4-23) and (4-24) yield estimates of natural frequency and damping ratio with different initial frequency settings, when ω_{01} and ω_{02} are read out in terms of voltage from the junction before VCO. Table 3 shows the estimated data. The estimated damping ratio follows the trend

of the set damping, and the estimated natural frequency is close to the identification data.

At a large VCO gain, the tracked frequency approaches the natural frequency as follows from Eq. (4-21). Figure 4.13(b) plots the tracked profile. Table 3 presents the data. The damping setting does not greatly affect the estimated natural frequency. The damping clearly does not affect ω_n . In the numerical results, the tracking frequency is close to the natural frequency at large VCO gain. The experimental data show that the VCO gain is approximately 10^3 . Due to the existence of the offset in the op-amp, a large VCO gain will cause saturation.

Practically, a real system is usually not a simple second order system. Continuous bodies have several natural frequencies in different modes. Furthermore, the junction between the structure and the circuits may results in extra modes. Dividing the frequency bandwidth into many sub-bands of the system that each behaves as a second order system for every division. Multi-band testing can be performed to estimate the system parameters with the proposed method. Moreover, this scheme can determine the net effect of the system, including the damping of the driving circuits and the sensing circuits.

4.4 Detection Modes

The driving electrodes and sensing electrodes are arranged as shown in Fig. 4.14(a). A driving electrode places opposite to a sensing electrode. The driving electrodes are separated with sensing electrodes. Because the electrostatic force is always attractive, the electrodes should be balance placed to enlarge the sensing range. As shown in Fig. 4.14(b), the electrodes D1, D2, and D4 are used to form the control loop. When the acceleration is positive to the x-axis, the voltage of D1 rises to pull the

ring back to the neutral position. When the acceleration is negative, D4 is accompanied with D2 to pull back the ring. Similar mechanism is used on y-axis. The summary of the rebalance force on electrodes for the acceleration is listed in Table 4. The feedback voltage signal in the closed-loop stands for the amplitude of the linear acceleration.

The structural displacement is caused both by linear acceleration and Coriolis force. As shown in Fig. 3.4, both linear acceleration and flexural vibration induce the displacement of the main ring of the structure. The displacement is expressed as follows.

$$S = X \cos \omega t + r \cos \omega_n t, \quad (4-22)$$

where X is the amplitude induced by linear acceleration, ω is the acceleration frequency, r is the amplitude of the flexural vibration, and ω_n is the natural frequency of the structure. The frequency range of the acceleration is from zero to 50Hz, and the natural frequency of the structure is 20K Hz. These two frequencies are far away and can be separated with filters. Higher order filter is used for boarder range of the acceleration.

The sensing coupling of the acceleration and rotation leads to the signal coupling, and force to rebalanced mode is used to eliminate this effect. The closed loop control is used for this purpose, and it has fast time response of signal. Figure 4.15 shows the concept. An extra force f_1 applies on the structure and induces the displacement. The rebalanced force f_2 feeds back to the structure according to the induced displacement. The PI control is used for the zero steady-state error.

Figure 4.16 shows the applying forces and corresponding displacements under second mode. The input force f_a is sinusoidal force with unit magnitude and zero-phase. Assume the input frequency is close

to the natural frequency, the response displacement x_a is $\frac{Q}{K}$ and the lagged phase is $(-\frac{\pi}{2} + \theta_a)$. The magnitude of vibration velocity v_a is $\frac{Q}{K}\omega$ and the phase lag is θ_a . When the structure is exposed to a rotation rate Ω , the induced Coriolis force is f_b . The magnitude of f_b is Ω times of v_a , and the phase lag is the same as which of v_a . The corresponding displacement induced by f_b is x_b . The magnitude of x_b is $(\frac{Q}{K})^2\omega\Omega$. When the natural frequencies of two modes are identical, the phase lag of x_b is $(-\frac{\pi}{2} + 2\theta_a)$. Applying phase-locked loops to the driving circuit can effectively eliminate the phase lag θ_a , because it will actually track the phase at $-\frac{\pi}{2}$. If we use open-loop mode to detect the rotation rate, the ratio between x_a and x_b is expressed as follows.

$$\frac{x_b}{x_a} \propto \omega_n \Omega \frac{Q}{K}. \quad (4-23)$$

If we use force-to-rebalance mode to detect the rotation rate, the ratio between f_a and f_b is expressed as follows.

$$\frac{f_b}{f_a} \propto \omega_n \Omega \frac{Q}{K}. \quad (4-24)$$

Obviously, two expressions are similar. The magnitude of x_b is $(\frac{Q}{K})^2\omega\Omega$, that stands for the induced displacement will be magnified by quality factor and reduced by structural stiffness. Under slight damping condition, open-loop mode is preferred. Under atmosphere, the quality factor for the micro structure presented in this dissertation possibly is less than 10.

Moreover, if the natural frequencies of two modes are not identical, the ratio between x_a and x_b is expressed as follows.

$$\frac{x_b}{x_a} \propto \omega_n \Omega \frac{Q}{K} \frac{\sin(\omega t - \frac{\pi}{2} + \theta_b)}{\sin(\omega t - \frac{\pi}{2})}. \quad (4-25)$$

There exists an extra phase lag due to the different natural frequencies of two modes. The ratio between f_a and f_b remains simple expression as Eq. (4-25). Thus, force-to-rebalance mode is preferred. Table 5 lists the summary of applying forces and corresponding displacements under second mode.

4.5 Scheme for Detecting Rotation and Acceleration

When both the main ring and support rings of the sensor are considered, the governing equation of the n -th mode vibration is represented as follows.

$$\begin{cases} A\ddot{a}_n - B\Omega\dot{b}_n - B_2\dot{\Omega}b_n + c\dot{a}_n + Ca_n = F_{a_n} \\ A\ddot{b}_n + B\Omega\dot{a}_n + B_2\dot{\Omega}a_n + c\dot{b}_n + Cb_n = F_{b_n} \end{cases}, \quad (4-26)$$

where A is the effective mass; B and B_2 are the effective masses associated with the Coriolis force; c is the effective damping; C is the effective stiffness; F_{a_n} and F_{b_n} are the generalized forces, and a_n and b_n are generalized coordinates of the n th mode of vibration.

This work addresses the first and second modes. The first mode involves linear acceleration, and the second involves rotation. The rebalancing loop for detection is added to sense the rotation without which the signal process would be much more complex. Based on Eq. (4-26), with reference to the second mode but ignoring the angular acceleration, the driving forces are as follows.

$$\begin{cases} F_{a_2} = \sin \omega t \\ F_{b_2} = -Kb_2 \end{cases}, \quad (4-27)$$

where ω is the natural frequency of the second mode and equals $\sqrt{C/A}$ and K is gain of the rebalancing force which is exerted by the rebalancing loop. The output signal determined by the rebalancing loop is,

$$V_{rot} = Kb_2 = -\Omega \frac{B}{c} \sin \omega t. \quad (4-28)$$

The output voltage is proportional to the rate of rotation. This finding is obtained by setting a large gain of rebalancing force, making b_2 much smaller than a_2 in Eq. (4-26), such that the terms in b_2 can be neglected. It also eliminates the effect of angular acceleration. Figures 3.8(a) and 3.8(b) depict the detection scheme used to measure the rate of rotation. The fixed amplitude of the primary mode is driven in a_2 and the Coriolis force induces a response in the secondary mode in b_2 .

The first mode of vibration is rebalanced by two rebalancing loops to sense linear accelerations. The amplitude of induced displacement is constrained by the applied force, the driving frequency, effective stiffness, and gain of the rebalancing force. When the driving frequency is much smaller than the resonant frequency of the first mode, the amplitude and the output voltage are approximated to,

$$\begin{cases} a_1 = \frac{f_{acc}}{C + K} \\ V_{acc} = Ka_1 = \frac{K}{C + K} f_{acc} \end{cases}. \quad (4-29)$$

The effective stiffness is designed to be high to reduce the amplitude as much as possible. Also, the rebalance loop is added to yield the readout circuit. Figures 3.8(c) and 3.8(d) present the detection scheme for sensing

acceleration. The opposing support rings are displaced equally when the structure is accelerated. The difference between the induced signals of the displacements of the opposing support rings represents the linear accelerations.

4.6 Theoretical Errors

The sources of theoretical errors discussed herein include the shifting of the natural frequency and angular acceleration. The structure is designed to vibrate at its resonant frequency, is close to the natural frequency if damping is weak. The factors that influence the resonant frequency must be considered. The first one is damping. Providing a stable environment in which the sensor can operate is a solution. Acceleration is one primary factor that influences the natural frequency. Theoretically, a force or acceleration causes the natural frequency to drift, governed by,

$$\Delta\omega = \omega_n \cdot \sqrt{\frac{r^2}{EI n^2 \pi^2} \cdot F} . \quad (4-30)$$

According to the simulation results, this drift is neglectable. This effect depends on the ratio of the applied force to the relative stiffness of the structure. In this work, this ratio on the micro scale is too small to have any effect.

Equation (4-26) specifies the errors due to the angular acceleration. As mentioned, the sensor incorporates designed rebalancing loops. A steady state error actually occurs in the rebalancing loops. This error is simply treated as a constant force applying to the structure. Equation (4-26) for the second mode of vibration is solved as follows;

$$\begin{aligned}
 a_n &= \frac{1}{C} F_a + \frac{B_2 \dot{\Omega}}{C^2 + KC + (B_2 \dot{\Omega})^2} F_b \\
 b_n &= \frac{-B_2 \dot{\Omega}}{C^2 + KC + (B_2 \dot{\Omega})^2} F_a + \frac{C}{C^2 + KC + (B_2 \dot{\Omega})^2} F_b
 \end{aligned}
 \tag{4-31}$$

When a force is applied, an angular acceleration causes the force in a single direction to have an unwanted influence on another direction, generating noise. Applying a sinusoidal force also creates this problem. Increasing the effective stiffness and the gain of the rebalancing force can solve it. However, an excessive effective stiffness makes the natural frequency of the structure extremely high, which leads to a high working point of the circuit. A better alternative is to increase the gain of the rebalancing force.



Chapter 5 Structural Fabrication and Preliminary Test

In general, silicon micro-machining processes for fabrication of vibratory gyroscopes fall into one of four categories: 1) silicon bulk micromachining and wafer bonding; 2) poly-silicon surface micromachining; 3) metal electroforming and LIGA; and 4) combined bulk surface micromachining or so-called mixed processes [87]. The process proposed in this chapter falls in to the first category. The fabrication is based on the deep silicon etching and wafer bonding. An aspect ratio dependent effect (ARDE) always occurs in the dry etching process for a MEMS device. Three sets of processes are developed and modified progressively for eliminating ARDE from the fabrication results. Results indicate that the proposed process provides more flexibility than other processes with respect to the structural fabrication of a MEMS device. The sensitivity of the sensor characteristic to the manufacturing errors is considered as well. Preliminary test results are also presented.

5.1 Brief of Process Technologies

The deep silicon etching used in this dissertation is executed with inductive coupled plasma (ICP). Two sets of RF power unit provide high-density plasma and isotropic etching. With this setting, the effective plasma area locates middle of the chamber and does not damage the chamber surface. It also decoupled the effects for two independent power sources. The primary etchants are SF₆ and C₄F₈. The original etchants

are SF₆ and oxygen, and the later is the sidewall passivating gas. The sidewall etching simultaneously happens and the protection is required to provide better slope. With oxygen adding, the silicon dioxide recombines and deposits on the surface including sidewall and bottom [88,89]. An alternative is to provide the passivation from C₄F₈. With C₄F₈, the thin Teflon like passivation layer deposits on the wafer, including the bottom and the sidewall of previously etched hole during the process. Significantly higher aspect ratios are achieved by using a time-multiplexed process, which continuously switches between passivation and etching steps. This method works for this scale but not for narrower gap to 0.1μm. The reason comes from the thickness of the polymer. For the scale of sub-micron, the influence from the polymer is comparable with gap itself. The chlorine etching is a possible solution. The possible damages from the ICP dry etching process are electrical and mechanical influence. Electrically, the plasma may damage the threshold voltage of the p-n junction and the breakdown of the gate oxide. The circuit component is not implemented on the structure, and it does not affect the design. The process quiet often induces the structural damage for III-V but not for silicon. Especially, the desired material is silicon wafer and it inherits the crystalline structure even processed. Some experiment shows that the high-density plasma caused low stress and damage during the process relative to other fabrication process [90].

The dry etched silicon wafer and the glass wafer are bonded with anodic bonding technique. This process is accomplished with anodic bonder. The bonding temperature is 380°C and the bonding voltage is 500 volt. Generally speaking, the anodic bonding technique is used to bond the silicon and glass, and it is a mature technique that required simple equipment setup. Anodic bonding relies on charge migration to produce bonded wafers. This usually involves a silicon wafer and a glass wafer

with a high content of alkali metals [91]. For instance, Pyrex borosilicate glass, a typical material for this application, has a sodium oxide (Na_2O) content of 3.5%. In this approach, the presence of mobile metals is exploited by applying a high negative potential to the glass to attract the positive ions (Na^+) to the negative electrode, where they are neutralized [92]. Such a removal permits the formation of a space charge at the glass-silicon interface, which creates a strong electrostatic attraction between the silicon and the glass wafers that holds both pieces firmly in place. This technique has been reported as producing uniform bonds; however, the presence of charge carriers makes this bond generally not compatible with active devices. The bonding process increases the leakage current for CMOS process [94]. The technique, originally proposed by Wallis and Pomerantz [95], has been used for pressure sensor, solar cell, and piezoresistive applications, as well as for packaging. A novel application which involves with anodic bonding, was presented in 1997 by Robert Bayt [96]. Moreover, the structure fabricated with anodic bonding can withstand a chamber pressure up to 1000 psi. This process does not involve many problems for mechanical property.

The structure is dumped into the KOH to etch the upper layer of silicon. The composition of the KOH solution should be taken care about the relative etching rate for silicon to oxide. The desired condition for KOH is 10%wt and 60°C that implies the ratio to 1000[97]. An alternative etchant is TMAH which provides very high etching selectivity for silicon to oxide [103,104]. Moreover, both using of KOH and TMAH require a stable environment to insure the liquid concentration remains constant.

5.2 Fabrication Process

The device can be fabricated in numerous ways. Silicon bulk micromachining and wafer bonding technologies are used in this work follow from the structural design and the capacitive detection scheme. The main frame of the structure sits on the plane of the silicon wafer. The structural stiffness along the z-axis should be as large as possible to minimize the coupling of vibrations along different axes. Hence, deep silicon etching is used to form a bulk structure. Besides, detecting and driving schemata, based on the electrostatic force, would be more effective for relatively large capacitances. A larger capacitance corresponds to a deeper structure. Deep silicon etching technique for forming high-aspect-ratio structures must be used to ensure good detection performance. Anodic bonding is utilized to bond the silicon to the glass. It is a mature technique and is used herein to create the suspended structure.

Three processes are developed for fabricating the structure of the motion sensor. They are modified to reduce the ARDE and are described as follows. The process described in the following sections is observed along $\overline{AA'}$ indicated in Fig. 4.1(a).

Figure 5.1 shows the first method of fabricating the sensor. The process begins with a $\{1, 0, 0\}$ n-type silicon wafer, which is patterned using photo resist, as depicted in Fig. 5.1(a). The patterned wafer is etched with deep silicon etching by ICP etcher, as depicted in Fig. 5.1(b). The etched silicon wafer is bonded to a glass wafer by anodic bonding, as depicted in Fig. 5.1(c). The upper part of the composite wafer is removed by back-sided wet etching and the structure is formed, as indicated in Fig. 5.1(d). The structure is then released by wet etching the glass wafer, as indicated in Fig. 5.1(e). Ideally, the etching rate is uniform at every

position on the wafer. During deep etching, the RIE lag appears in the narrow trench. This effect is known as the aspect ratio dependent effect (ARDE). Figure 5.1(b) plots the RIE lag in the capacitor gap. The capacitor gap is 2 μm wide, as shown in Fig. 4.1(a). During the wet etching of the backside, some part not on the capacitor gap will be etched through first, as presented in Fig. 5.1(d). Intuitively, etching could be continued through the gap. However, this aforementioned structure has a high aspect ratio. Etching through the silicon wafer causes permanent damage to the wall of the structure. The structure will not be released until the removal of the RIE lag part of the structure, as depicted in Fig. 5.1(e). Figure 5.2(a) presents the side view of the unreleased structure, which has formed a 100 μm -high wall. Reducing the etching depth reduces ARDE and the RIE lag. Figure 5.2(b) presents the structure with a 20 μm -high wall. However, the final structure is not sufficiently strong to prevent structural warping. The ARDE is negligible for the designed 20 μm -high structure.

An alternative means (method II) of modifying the process is to add a protective layer and dummy fields. Figure 5.3 schematically describes method II. The dummy field can be used to reduce the RIE lag in dry etching, as plotted in Fig. 5.3(b). The RIE lag is not entirely eliminated, because the dummy field should be sized so as not to affect the performance of the sensor. Hence, the gap between the structure and the dummy field is wider than that between the structure and the electrode. The protective layer is added after dry etching and before anodic bonding, as depicted in Fig. 5.3(c). This protective layer must be suitable to undergo the anodic bonding process. Hence, oxide and nitride are the candidate materials for this layer. This layer will protect the wall of the structure as long as the silicon is etched through in a back-sided wet

etching process. The protective layer should resist the etchant until the RIE lag part is removed. The etchant used in wet etching must be isotropic. The height of the structure can be estimated from the following formula.

$$H = \frac{t \cdot S}{L_{RIE}} \cdot (1 - L_{RIE}), \quad (5-1)$$

where H is the height of the structure; t is the thickness of the protective layer; S is the selectivity of the etchant, and L_{RIE} is the RIE lag ratio. The protective layer used in this case is nitride, and its thickness is 2000\AA . A thicker layer does not favor anodic bonding. The etchant used is HNA. The etching selectivity is 60. The dummy fields reduce the RIE lag ratio to 0.2. The height of the structure with the protective layer is estimated to be up to $40\mu\text{m}$, when the protective layer is included. When the protective layer is etched away and the silicon is exposed, as described above, etching can be performed $20\mu\text{m}$ more deeply, without being affected by the ARDE. Hence, a $60\mu\text{m}$ ($40\mu\text{m} + 20\mu\text{m}$) structure is accordingly fabricated, and is presented in Fig. 5.4.

The third method improves upon method II. The dummy field is sized to equalize the widths of all trenches (gaps) on the wafer, effectively eliminating ARDE and the RIE lag, as presented in Figs. 5.5(a) and 5.5(b). Unlike in method II, the dummy fields must be removed. A $2\mu\text{m}$ step between the bonding region and non-bonding region is etched before the PR coating process is performed to remove the dummy field, as indicated in Fig. 5.5(a). The dummy field makes negligible RIE lag in the deep silicon etching process. The protective layer is deposited on silicon, as depicted in Fig. 5.5(c), and a 2000\AA oxide is used herein. This layer is not necessary but still used for better yield. An inter layer of 5000\AA nickel is deposited on the glass wafer. This layer prevents the

bonding of dummy fields to the glass, as indicated in Fig. 5.5(d). It also prevents the bonding of the structure to the glass, ensuring that the structure is ideally released. An anodic bonder is used to bond the silicon wafer and the glass wafer. Back-sided wet etching removes the upper part of the resulting SOI structure, yielding the structure depicted in Fig. 5.5(e). The structure is released by wet etching the glass wafer, as depicted in Fig. 5.5(f). Figure 5.6 presents the resulting structure, whose height is 180 μm , which is satisfactory [106].

During the removal of the dummy fields, rather than increasing the step height which generates lithographic deficit, the inter layer is introduced between the silicon and the glass in this method. Moreover, anodic bonding can generate a large electrostatic force that collapses the suspended structure. In the absence of an interlayer, the force would pull silicon and glass into contact with each other, causing undesired bonding [105].

There is a parameter, which is not directly involved with the fabrication, but concerned about package. It is quality factor, and it vitally affects the sensor performance. With high quality factor, the signal would be magnified and the noise would be suppressed relatively. For the sensor, the quality factor is concerned about structure damping and the viscous damping. The structure damping comes from the silicon itself. Both single and polycrystalline silicon microstructures have shown high mechanical quality factors (10^4 to 10^6) under medium vacuum levels that the pressure is less than 10 milli-torr [98]. In other words, the quality factor is dominated by viscous damping under atmosphere or low vacuum levels. Generally, the viscous damping for the microstructure is classified as lateral damping [99] and squeeze damping [100]. The lateral damping means the damping effect exists at the lateral period relative to the moving direction. It is recognized with Reynold's Number. The squeeze-

film damping theory describes about phenomenon that the air is trapped between two parallel plates. It is quite often for microstructure. The condition for the squeeze-film is expressed as the squeeze number. With considering about the sensor for those two damping theories, the quality factor of the structure is 15 under 10 torr. The quality factor required from the design needs more than that, which means a vacuum environment provided by packaging is required. Anodic bonding contains the possibility to provide the package. The glass is used as the substrate and it can be used more. In fact, many designs have taking advantage on anodic bonding to provide vacuum and relative package [101].

5.3 Sensitivity of Sensor Characteristics to Manufacturing

Errors in Fabrication

The ring radius, ring width, ring thickness, and gap between the ring and the electrode may all manifest manufacturing errors. Their sensitivities are estimated from the dimensional parameters, given in Table 6. Single crystal silicon is a suitable material for its material properties, including density and Young's modulus, are stable. In fact, lithography rarely produces an error in the ring radius. Therefore, only by the error in the ring width that arises during fabrication affects the resonant frequency. The ring width designed here is $10\mu\text{m}/20\mu\text{m}$, and the possible resultant error is from $1\mu\text{m}$ to $2\mu\text{m}$, or 10%. The error in the width of the ring can cause an error in the width of the gap. The gap width used here is $2\mu\text{m}$, and so the error may strongly influence the performance of the sensor. The width of the gap increases as the width of the ring is reduced. An error in the gap width is the most common manufacturing error. Figure 5.7 plots the normalized sensitivities, listed in Table 6, versus the change in the gap width. The width of the ring is

designed to be ten times the width of the gap. The maximum error in the gap width is usually equal to the designed gap width because of the etching process used in this work. The normalized sensitivities of the sensor characteristics of interest to the inaccuracy in the gap width depicted in Fig. 5.7 shows that every considered characteristic is degraded as the gap width increases. The figure also shows that the gap width increase influences less on the natural frequency about 10%, and on acceleration signal about 30%. However, the gap width increase seriously downgrades the other sensor characteristics. In the worst case, parameters such as the S/N ratio fall to around one-fifth of the designed values. Improve the process capability or taking other method to fabricate the structure is necessary. The anisotropic characteristics of the structure can cause coupling of the vibration modes, which are related to crystallographic orientation of the silicon wafer [35], and the rotational misalignment in the fabrication. They can be eliminated by aligning the first mask with the crystal orientation of the wafer[36].

5.4 Preliminary Test

Figure 5.8(a) presents the gap between the support ring and the electrode in their neutral positions. Figure 5.8(b) indicates that the gap width is reduced when the electrode attracts the support ring. Figure 5.9(a) depicts the support ring is deformed into an oval shape. Figure 5.9(c) depicts the electrical connection of the driving electrode. This deformed shape is very close to the designed mode of vibration. Due to the over-etching in dry etching process, the width of gap increases to $4\mu\text{m}$ and the natural frequency of the structure decreases to around 19kHz by visually checked under microscope (10x100). The increase of gap width also makes the increase of pull-in voltage. The pull-in voltage is above 106

volt and theoretical value is 51 volt. Those results follow the estimation of sensitivities.

Figure 5.10(a) shows the connections of electrical test. The electrode is connected to a sinusoidal wave as the input. The output point locates between the support ring and the field. The right side corner of the field is connected to electrical ground. The capacitance between the support ring and electrode is simplified as effective capacitance C_x . The resistance of the support is simplified as effective resistance R_{ring} , and the resistance between the output point and ground is represented as R_{field} . Figure 5.10(b) shows the simplified model of the electrical test. Figure 5.10(c) shows the frequency response when 5 volt signal feed to the structure, and it shows the circuit is a typical high pass filter. Those parameters in the simplified model are estimated as follows. R_{field} is $12\text{k}\Omega$, R_{ring} is $100\text{k}\Omega$, and C_x is 1.294pf . In fact, this test does not show the exact properties of the system, but it helps to estimate whether the fabrication result follows the design or not. The capacitance C_x is 0.63pf in theory. The resistances appeared to be higher than the theoretical analysis which calculates that R_{ring} and R_{field} are within $1\text{k}\Omega$. It decreases the detecting current and causes signal drift. Under this circumstance, switched-capacitor type interface circuit is sound.

Chapter 6 Conclusion

The object throughout this research was to develop a micro sensor detecting both linear acceleration and rotational rate. Many of our goals were achieved with the sensor design discussed in this dissertation. Some were not. In this chapter we summarize the results from the recent development and discuss options for completing the sensor development.

6.1 Summary of the Research

Through the recent designs for the micromachined accelerometer and the vibrating gyroscope, the capacitive type accelerometer and vibrating ring gyroscope are high potential to be integrated not only for similar structure but the compatible driving and detecting schema.

In theory, the Coriolis force induced by rotation and transportation speed in the rotation frame. By setting the speed, the induced Coriolis force proportionally indicates the rotation rate. Setting the rotation rate to measure the transportation speed is not suitable for microstructure because it is relatively complicated to make a micro rotating structure.

The vibration of a ring can be decoupled into several modes. With proper design of structural size, the first mode and second mode can properly indicate the linear acceleration and rotation rate. Considering the symmetry of support, asymmetry supports is difficult to be analyzed by using simple coordinates. Even under symmetrical arrangement connected to the main ring, it still affects the vibration under acceleration.

Rotational symmetry and mirror symmetry are both required for the structural design.

A simple concept of impedance helps to calculate the natural frequency of the structure, and the corresponding modes are obtained by finite element analysis. The errors between these results are less than 5%. The drift of natural frequency caused by applying force is slight for microstructure.

The structural design leads to mixed signal contains acceleration and rotation signals. Four loops are required for the detection circuits. The phase locked loop is merged into the driving circuit to obtain high quality factor, and it is useful for determine the damping ratio and the undamped natural frequency of the structure. It is also necessary for detecting rotation rate. Using force-to-rebalance mode of detection could eliminate those noise caused by the different natural frequencies of two vibrating axes. Setting high feedback loop gain helps to eliminate the theoretical error caused by angular acceleration.

The structure is fabricated by using silicon deep etching and anodic bonding technologies. Three sets of process are developed and compared for eliminating the aspect ratio dependent effect that always found after deep silicon etching. Some undesired bonding was found after anodic bonding process. It is possible caused by the strong electrostatic force during the bonding process, and adding an inter layer of metal between the structure and glass substrate eliminates this effect. The primary manufacturing error is the over-etching during deep silicon etching. The sensitivity analysis shows the worst case of the downgrade sensor characteristic is S/N ratio falls to around one-fifth of the designed value. The applying of anodic bonding also provides a method for the sensor package.

The preliminary test shows that the natural frequency decreases to around 19kHz, which follows the estimation of sensitivities. The electrical test to the structure shows that the fabrication result follows the design in general. However, the existence of large internal resistance may dramatically affect the detected signal. Redesigning the proper interface circuit will greatly improve the sensor performance.

In summary, this dissertation has discussed the development of a micro sensor detecting both linear acceleration and rotation rate. The structural design, electronics analysis, and fabrication are presented. The preliminary test shows that the sensor is highly feasible to be carried out by using micromachining technology.

6.2 Potential Improvement to the Design

For the structural design, the radial vibration along with the primary axis may induce the tangential vibration along with the secondary axis. It may cause undesired quadrature signal to the detection circuit. The possible way is to design a support to transmit only the radial displacement.

The existence of large internal resistance of the structure may seriously affect signal detection of the interface circuit. One possible way is to change the material of the structure. The other way is to design switched capacitor circuit suitable for the structure.

Vertical thin wall structure is manufactured according to the structural and electrical design. Owing to the fabrication difficulty in making deep trench, applying comb appears to offer great potential of improvement.

References

- [1] Keister, G.W. *Sensors and transducers*, ECN 21-32. Apr. 1992.
- [2] L.K. Baxter, "Capacitive Sensors Design and Applications", IEEE Press, New York, 1997.
- [3] "The Vibration Gyroscope", *British Aerospace Systems and Equipment Report #TR5102*, March 1993.
- [4] A. Lawrence, "Modern Inertial Technology Navigation Guidance and Control", Springer-Verlag, New York, 1993, pp. 163-181.
- [5] A. Lawrence, "Modern Inertial Technology Navigation Guidance and Control", Springer-Verlag, New York, 1993, pp. 148-162.
- [6] E.J Loper, D.D. Lynch, "Projected System Performance Based on Recent HRG Test Results", *Proceedings 5th Digital Avionics System Conference*, Seattle, Washington, Nov. 1983.
- [7] L.M. Roylance, J.B. Angeel, "A Batch-fabricated Silicon Accelerometer", *IEEE Transactions on Electron Devices*, Vol. ED-26, No. 12, 1979, pp. 1911-1917.
- [8] H. Seidel, H. Riedel, R. Jolbeck, G. Muck, W. Kuoke, M. Koniger, "Capacitive Silicon Accelerometer with Highly Symmetrical Design", *Sensors and Actuators*, A21-A23, 1990, pp. 312-315.
- [9] K. Okada, "Tri-Axial Piezo-electric Accelerometer", *Transducer '95*, June 25-29, 1995, pp. 566-569.
- [10] B. Puers, L. Reynaret, W. Soneyw, W.M.C. Sansen, "A New Uniaxial Accelerometer In Silicon Based on The Piezo-junction Effect", *IEEE Trans. of Electronic Device*, Vol. 35, No. 8, 1988, pp. 764-770.
- [11] R. Hiratsuka, D.C.V. Duyn, T. Otaredain, P. de Vries, "Design Consideration for The Thermal Accelerometer", *Sensors and Actuators A*, Vol. 32, 1992, pp. 380-385.

- [12] E. Abbaspour-Sani, R.S. Huang, C.Y. Kwok, “A Linear Electromagnetic Accelerometer”, *Sensors and Actuators*, A44, 1994, pp. 103-109.
- [13] H.K. Rockstad, T.W. Kenny, J.K. Reynolds, W.J. Kaiser, T.B. Gabrielson, “A Miniature High Sensitivity Broad-band Accelerometer Based on Electron Tunneling Transducers”, *Sensors and Actuators A*, Vol. 43, 1994, pp. 107-114.
- [14] Ronald N. Arnold, Leonard Maunder, “Gyrodynamics and its Engineering Applications”, Academic Press, New York and London, 1961, pp. 49-59.
- [15] Donald T. Greenwood, “Principles of Dynamics 2nd edition”, Prentice-Hall, 1988, pp. 48-50.
- [16] Robert A. Berker, “Introduction to Theoretical Mechanics”, McGraw-Hill, 1974, pp. 248-255.
- [17] Anders Persson, “How Do We Understand the Coriolis Force?”, *Bulletin of the American Meteorological Society*, Vol. 79, No. 7, July 1998, pp. 1373-1385.
- [18] Eliassen, A., and K. Pedersen, “*Meteorology, An Introductory Course. Vol. I, Physical Processes and Motion*”, Universitetsforlaget, 1977, pp. 204.
- [19] Quick, W.H. “Theory of the vibrating string as an angular motion sensor”, *Trans. ASME, J. Appl. Mech.*, Sep. 1964, pp.523-534.
- [20] W. D. Gates, “Vibrating Angular Rate Sensors May Threaten the Gyroscope”, *Electronics*, 10, June 1968, pp. 130-134.
- [21] S. Fujishima et al, “Piezoelectric Vibratory Gyroscope using Flexural Vibration of a Triangular Bar”, *IEEE 45th Annual Symposium on Frequency Control*, 1991, pp. 261-265.
- [22] A. Lawrence, “Modern Inertial Technology Navigation Guidance and Control”, Spring-Verlag, New York, 1993, pp. 149-151.

- [23] D. Boocock, L. Maunder, "Vibration of a symmetry tuning fork", *J. Mech. Eng. Sci.* 11, 4, 1969.
- [24] Hunt, G.W., A.E.W. Hobbs, "Development of an accurate tuning-fork gyroscope", *Symposium on Gyros, Proc. Inst. Mech. Eng.*, London, 1964.
- [25] L. Parameswaran, C. Hsu, and M. A. Schmidt, "A Merged MEMS-CMOS Process Using Silicon Wafer Bonding," *Proc. IEEE Int. Electron Devices Mtg.*, Washington, DC, December 1995.
- [26] P. Greiff, B. Boxenhorn, T. King, and L. Niles, "Silicon monolithic micromechanical gyroscope," in *Tech. Dig. 6th Int. Conf. Solid-State Sensors and Actuators (Transducers'91)*, San Francisco, CA, June 1991, pp. 966–968.
- [27] K. Maenaka, T. Fujita, Y. Konishi, and M. Maeda, "Analysis of a highly sensitive silicon gyroscope with cantilever beam as vibrating mass," *Sensors Actuators A*, vol. 54, pp. 568–573, 1996.
- [28] D. Wood, G. Cooper, J. Burdess, A. Harris, and J. Cruickshank, "A silicon membrane gyroscope with electrostatic actuation and sensing," in *Proc. SPIE 1995 Symp. Micromachining and Microfabrication*, Austin, TX, 1995, pp. 74–83.
- [29] H. Kuisma, T. Ryhanen, J. Lahdenpera, E. Punkka, S. Ruotsalainen, T. Sillanpaa, and H. Seppa, "A bulk micromachined silicon angular rate sensor," in *Tech. Dig. 9th Int. Conf. Solid-State Sensors and Actuators (Transducers'97)*, Chicago, IL, June 1997, pp. 875–878.
- [30] W. A. Clark, R. T. Howe, and R. Horowitz, "Surface micromachined-axis vibratory rate gyroscope," in *Tech. Dig. Solid-State Sensor and Actuator Workshop*, Hilton Head Island, SC, June 1996, pp. 283–287.

- [31] T. Juneau and A. P. Pisano, "Micromachined dual input axis angular rate sensor," in *Tech. Dig. Solid-State Sensor & Actuator Workshop*, Hilton Head Island, SC, June 1996, pp. 299–302.
- [32] Y. Oh, B. Lee, S. Baek, H. Kim, J. Kim, S. Kang, and C. Song, "A surface-micromachined tunable vibratory gyroscope," in *Proc. IEEE Micro Electro Mechanical Systems Workshop (MEMS'97)*, Japan, 1997, pp. 272–277.
- [33] K. Y. Park, C. W. Lee, Y. S. Oh, and Y. H. Cho, "Laterally oscillated and force-balanced micro vibratory rate gyroscope supported by fish hook shape springs," in *Proc. IEEE Micro Electro Mechanical Systems Workshop (MEMS'97)*, Japan, 1997, pp. 494–499.
- [34] S. An, Y. S. Oh, B. L. Lee, K. Y. Park, S. J. Kang, S. O. Choi, Y. I. Go, and C. M. Song, "Dual-axis microgyroscope with closed-loop detection," in *Proc. IEEE Micro Electro Mechanical Systems Workshop (MEMS'98)*, Heidelberg, Germany, Feb. 1998, pp. 328–333.
- [35] W. Geiger, B. Folkmer, J. Merz, H. Sandmaier, and W. Lang, "A new silicon rate gyroscope," in *Proc. IEEE Micro Electro Mechanical Systems Workshop (MEMS'98)*, Heidelberg, Germany, Feb. 1998, pp. 615–620.
- [36] T. Juneau, A. P. Pisano, and J. H. Smith, "Dual axis operation of a micromachined rate gyroscope," in *Tech. Dig. 9th Int. Conf. Solid-State Sensors and Actuators (Transducers'97)*, Chicago, IL, June 1997, pp. 883–886.
- [37] T. Fujita, T. Mizuno, R. Kenny, M. Maenaka, and M. Maeda, "Two-dimensional micromachined gyroscope," in *Tech. Dig. 9th Int. Conf. Solid-State Sensors and Actuators (Transducers'97)*, Chicago, IL, June 1997, pp. 887–890.

- [38] M. W. Putty and K. Najafi, "A micromachined vibrating ring gyroscope," in *Tech. Dig. Solid-State Sensor and Actuator Workshop*, Hilton Head Island, SC, June 1994, pp. 213–220.
- [39] M. W. Putty, "A micromachined vibrating ring gyroscope," Ph.D. dissertation, Univ. Michigan, Ann Arbor, Mar. 1995.
- [40] D. R. Sparks, S. R. Zarabadi, J. D. Johnson, Q. Jiang, M. Chia, O. Larsen, W. Higdon, and P. Castillo-Borelley, "A CMOS integrated surface micromachined angular rate sensor: It's automotive applications," in *Tech. Dig. 9th Int. Conf. Solid-State Sensors and Actuators (Transducers'97)*, Chicago, IL, June 1997, pp. 851–854.
- [41] F. Ayazi and K. Najafi, "Design and fabrication of a highperformance polysilicon vibrating ring gyroscope," in *Proc. IEEE Micro Electro Mechanical Systems Workshop (MEMS'98)*, Heidelberg, Germany, Feb. 1998, pp. 621–626.
- [42] A. Selvakumar and K. Najafi, "High density vertical comb array microactuators fabricated using a novel bulk/poly-silicon trench refill technology," in *Tech. Dig. Solid-State Sensor and Actuator Workshop*, Hilton Head Island, SC, USA, 1994, pp. 138–141.
- [43] Fox, C.H.J. & Hardie, D.S.W. "Vibratory Gyroscopic Sensors Symposium Gyro Technology", (DGON), 1984.
- [44] Varnham M.P. et al, US Patent 5226321.
- [45] I. Hopkin, "Performance and design of a silicon micromachined gyro", *Proc. Symp. Gyro Technology*, Stuttgart, Germany, 1997, pp. 1.0–1.10.
- [46] W. Soedel, "Vibrations of Shells and Plates", Marcel Dekker, New York and Basel, 1981, pp. 76-80.
- [47] S. Timoshenko, D.H. Young, W. Weaver, JR., "Vibration Problems in Engineering 4th edition", John Wiley & Sons, 1974, pp. 476-481.
- [48] F. P. Beer, E. Russell Johnston JR, "Vector Mechanics for Engineers", McGraw-Hill, 1977.

- [49] G. H. Duffey, "Applied Group Theory for Physicists and Chemists", Prentice Hall, Englewood Cliffs, 1992, pp.106-120.
- [50] A. D. Boardman, D.E. O'Connor, P.A. Young, "Symmetry and its Applications in Science", J.W. Arrowsmith, Bristol, England, 1973, pp. 8-17.
- [51] M. A. Armstrong, "Groups and Symmetry", Springer-Verlag, New York, 1988.
- [52] Rudolf Lidl, Gunter Pilz, "Applied abstract algebra", Springer, New York, 1998.
- [53] A. Lawrence, "Modern Inertial Technology Navigation Guidance and Control", Springer-Verlag, New York, 1993, pp. 152-157.
- [54] Ansys, INC, "Ansys® Release5.3", 1996.
- [55] S. Timoshenko, D.H. Young, W. Weaver, JR., "Vibration Problems in Engineering 4th edition", John Wiley & Sons, 1974, pp. 453-455.
- [56] Y. Cheng, "Development of LIGA Process for Micro Gyroscope", Report No.87-Yao Cheng-LIGA, The Micromachining Laboratory of SRRC, 1998.
- [57] R. T. Howe, "Resonant Microsensors", 4th International Conference on Solid State Sensors and Actuators, Tokyo, Japan, 1987, pp. 843-848.
- [58] L.K. Baxter, "Capacitive Sensors Design and Applications", IEEE Press, New York, 1997, pp. 51-56.
- [59] P.E. Allen, E. Sanchez-Sinencio, "Switched Capacitor Circuits", Van Nostrand Reinhold, New York, 1984.
- [60] P.K. Chan, H.L. Zhang, "A Switched-Capacitor Interface Circuit for Integrated Sensor Applications", ISCAS, vol. 1, 2001, pp. 372-375.
- [61] S. Ogawa, K. Watanabe, "A Switched-Capacitor Interface for High-Accuracy, High-Speed Ratiometric Signal Processing of Differential Capacitance Transducers" Proceedings of the 18th IEEE

- Instrumentation and Measurement Technology Conference, Vol. 2, 2001, pp. 1302-1307.
- [62] T. Salo, S. Lindfors, K. Halonen, "80 MHz Bandpass Delta-Sigma Modulator Using Switched-Capacitor Resonator Structure", *Electronics Letters*, Volume: 37 Issue: 14, 5 July 2001, pp. 877-878.
- [63] A. Srivastava, M.R. Gumma, J. Cherukuri, "Readout Interface Circuits for MOS C-V Sensors", *Proceedings of the 37th Midwest Symposium on Circuits and Systems*, 1994, vol. 1, pp. 187-190.
- [64] M. Kandler, J. Eichholz, Y. Manolo, W. Mokwa, "CMOS Compatible Capacitive Pressure Sensor with Read-out Electronics", *Microsystems*, Springer, New York, 1990, pp. 574-580.
- [65] G. H. Bryan, "On A Revolving Cylinder or Bell", *Proceedings of the Royal Society (London)*, 47, 1890.
- [66] Profschrift, Gerben Willem de Jong, "Smart Capacitive Sensors Physical, Geometrical and Electronics Aspects", *Delft University Press, Stevinweg*, 1994, pp. 133-137.
- [67] Joseph T. Kung, Hae-Seung Lee, "An Integrated Air-Gap-Capacitor Pressure Sensor and Digital Readout with Sub-100 Attofarad Resolution", *J. of Microelectromechanical Systems*, vol. 1, No.3, Sep. 1992, pp. 121-129.
- [68] Christopher J. Kemp, Leland Chip Spangler, "An Accelerometer Interface Circuit", *IEEE Custom Integrated Circuits Conference*, 1995, 15.2.1-15.2.4.
- [69] Joseph T. Kung, Hae-Seung Lee, Roger T. Howe, "A Digital Readout Technique for Capacitive Sensor Applications", *IEEE J. of Solid-State Circuits*, IEEE, vol. 23, No. 4, Aug 1988, pp. 972-977.
- [70] L.K. Baxter, "Capacitive Sensors Design and Applications", *IEEE Press*, New York, 1997, pp. 191-193.

- [71] Louis S Y Wong, Shohan Hossian, Andre Walker, “Leakage Current Cancellation Techniques for Low Power Switched-Capacitor Circuits”, International Symposium on Low Power Electronics and Design, Aug. 2001, pp. 310-313.
- [72] Y. E. Park, K. D. Wise, “An MOS Switched-Capacitor Readout Amplifier for Capacitive Pressure Sensors”, IEEE Proc. Custom IC Conf., Rochester, May 23, 1983, pp. 380-384.
- [73] Adel S. Sedra, Kenneth C. Smith, “Microelectronics Circuits”, Oxford University Press, New York, 1998, pp. 941-943.
- [74] Wen H. Ko, G. J. Yeh, “An Integrated Interface Circuit for Capacitive Sensors”, MicroSystem Technology, (Springer International), vol. 1, No. 1, Oct. 1994, pp42-47.
- [75] S. Chowdhury, G. A. Jullien, M. A. Ahmadi, W. C. Miller, N. Finch, D. Keating, “MEMS Acousto-Magnetic Components for use in a Hearing Instrument”, SPIE's Symposium on Design, Test, Integration, and Packaging of MEMS/MOEMS, Paris, France, May 9-11, 2000.
- [76] Gray K. Fedder, Roger T. Howe, “Multimode Digital Control of a Suspended Polysilicon Microstructure”, J. of MEMS, Vol. 5, No. 4, December 1996, pp. 283-297.
- [77] Dan H. Wolaver, “Phase-Locked Loop Circuit Design”, Prentice-Hall, 1991, pp. 1-5.
- [78] Roland E. Best, “Phase-Locked Loops Theory, Design, and Applications”, McGraw-Hill, 1993, pp. 7-25.
- [79] Paul Horowitz, Winfield Hill, “The Art of Electronics”, Cambridge University Press, 1989, pp. 641-653.
- [80] S. Timoshenko, D. H. Young, W. Weaver, “Vibration Problems in Engineering 4th ed”, John Wiley and Sons, 1974, pp. 72-79.

- [81] Robert P. Leland, "Adaptive Tuning for Vibrational Gyroscopes", Proceedings of 40th IEEE Conference on Decision and Control, Orlando, Florida USA, December 2001.
- [82] J. Crowe, M.A. Johnson, "Automated PI Control Tuning to meet Classical Performance Specifications using a Phase Locked Loop Identifier", Proceedings of the American Control Conference, Arlington, VA June 25-27, 2001.
- [83] Ansys, INC, "Ansys® Release5.3", 1996.
- [84] Sorab K. Ghandhi, "VLSI Fabrication Principles Second Edition", John Wiley and Sons, 1994, pp. 625-628.
- [85] M.W. Putty, K. Najafi, "A Micro-Machined Vibrating Ring Gyroscope", Tech Digest, Solid-State Sensors and Actuators Workshop, Hilton Head, SC, June 1994.
- [86] Jacob Fraden, "Handbook of Modern Sensors Physics, Designs, and Applications", AIP Press, 1997, pp. 25-27.
- [87] Navid Yazdi, Farrokh Ayazi, Khalil Najafi, "Micromachined Inertial Sensors", Proceedings of the IEEE, Vol. 86, No. 8, August 1998.
- [88] J. Bhardwaj, H. Ashraf, A. McQuarrie, "DRY SILICON ETCHING FOR MEMS", Symposium on Microstructures and Microfabricated Systems at the Annual Meeting of the Electrochemical Society, Montreal, Quebec, Canada, May 4-9, 1997.
- [89] A. A. Ayon, C. C. Lin, R. A. Braff, M. A. Schmidt, R. Bayt, and H. H. Sawin, "Etching Characteristics and Profile Control in a Time multiplexed Inductively Coupled Plasma Etch," *Solid-State Sensor and Actuator Workshop*, Hilton Head, SC, Jun. 1998, pp. 41-44.
- [90] Q. Chen, D.-J. Yao, C.-J. Kim, and G. P. Carman, "Investigation the Influence of Fabrication process and Crystal Orientation on Shear Strength of Silicon", *Journal of Material Science*, Vol. 35, No. 21, Nov. 2000, pp. 5465-5474.

- [91] S.A. Audet, K.M. Edenfeld, "Integrated Sensor Wafer-Level Packaging," Proc International Conference on Solid-State Sensors and Actuators, Chicago, Transducers '97, 1997, 1D4.09, pp. 287-289.
- [92] W.H. Ko et al. 1985. "Bonding Techniques for Microsensors," Micromachining and Micropackaging of Transducers, Elsevier Science Publishers.
- [93] R. C. Frye et al., J. Electrochem. Soc., Aug 1986, p. 1673.
- [94] K. Schjøllberg-Henriksen *et al.*, "Protection of MOS capacitors during anodic bonding", Technical Digest of MicroMechanics Europe, Cork, Ireland, 16-18 September 2001.
- [95] G.D. Wallis, D.I. Pomerantz, "Field Assisted Glass-Metal Sealing", J. Appl Physics, vol. 40, 1969, pp. 3946-3949.
- [96] R. Bayt et al., "A performance evaluation of MEMS-based Micronozzles", Proc 33rd AIAA/ASME/SAE/ ASEE Joint Propulsion Conference and Exhibit, Seattle, WA, July 1997.
- [97] H. Seidel et al., "Anisotropic Etching of Crystalline Silicon in Alkaline Solutions", J. Electrochem. Soc., Vol. 137, No. 11, November 1990, pp. 3612-3632.
- [98] K. Y. Yasumura *et al.*, "A study of microcantilever quality factor," in *Proc. Solid-State Sens. Actuator Workshop*, Hilton Head, SC, June 8-11, 1998, pp. 65-70.
- [99] Xia Zhang, William C. Tang, "Viscous Air Damping in Laterally Driven Microresonators", MEMS'94, pp. 199-204.
- [100] M. Andrews, I. Harris, G. Turner, "A Comparison of Squeeze-Film Theory with Measurements on a Microstructure", Sensors and Actuators, part: A, vol. 36, 1993, pp. 79-87.
- [101] A.R. Mirza, A.A. Ayon, "Silicon Wafer Bonding: Key to MEMS High-Volume Manufacturing", <http://www.sensormag.com/articles-1298/sil1298/main.shtml>.

- [102] H. Bruschi and G. Torzo, Method for accurate resonant frequency measurement with a phase modulated feedback loop, *Review of Science Instrumen*, 58 , 1978, pp. 2181-2184.
- [103] Kenji Tokoro, Daisuke Uchikawa, Mitsuhiro Shikida, and Kazuo Sato “Anisotropic Etching Properties of Silicon in KOH and TMAH Solutions” International Symposium on Micromechatronics and Human Science, 1998.
- [104] Kenji Tokoro , Daisuke Uchikawa, Kazuo Sato, Mitsuhiro Shikida “Comparision of Anisotropic Etching Properties between KOH and TMAH Solutions” IEEE, International Symposium on Micromechatronics and Human Science, 1999.
- [105] E. Obermerier, “Anodic Wafer Bonding”, Proceedings of the 3rd International Symposium on Semiconductor Wafer Bonding, vol. 95-7, 1995, pp. 212-220.
- [106] Jui-Hong Weng ,Wei-Hua Chieng and Jenn-Min Lai, “Structural fabrication of a ring-type motion sensor”, J. Micromech. Microeng. 14, 2004, pp. 710–716.
- [107] Jui-Hong Weng ,Wei-Hua Chieng and Jenn-Min Lai, “Structural design and analysis of micromachined ring-type vibrating sensor of both yaw rate and linear acceleration” Sensors and Actuators A 117 , 2005, pp. 230–240.

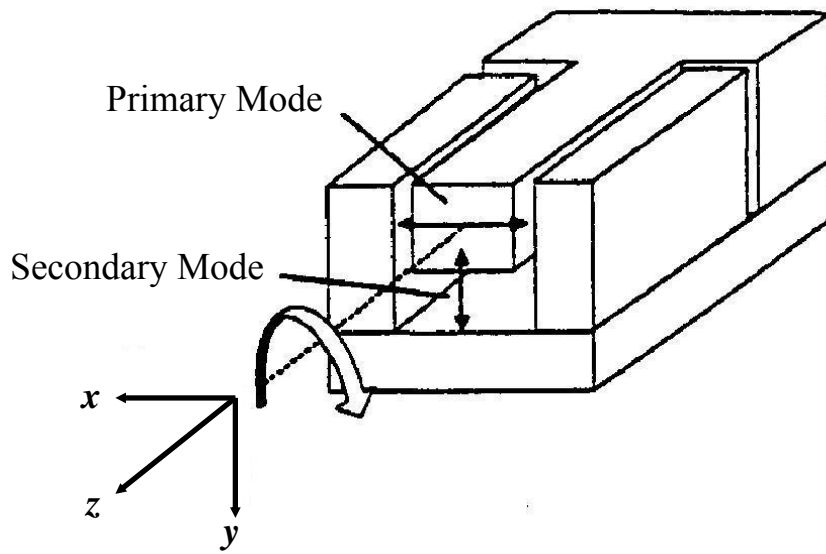


Figure 2.1 Vibrating beam gyroscope.

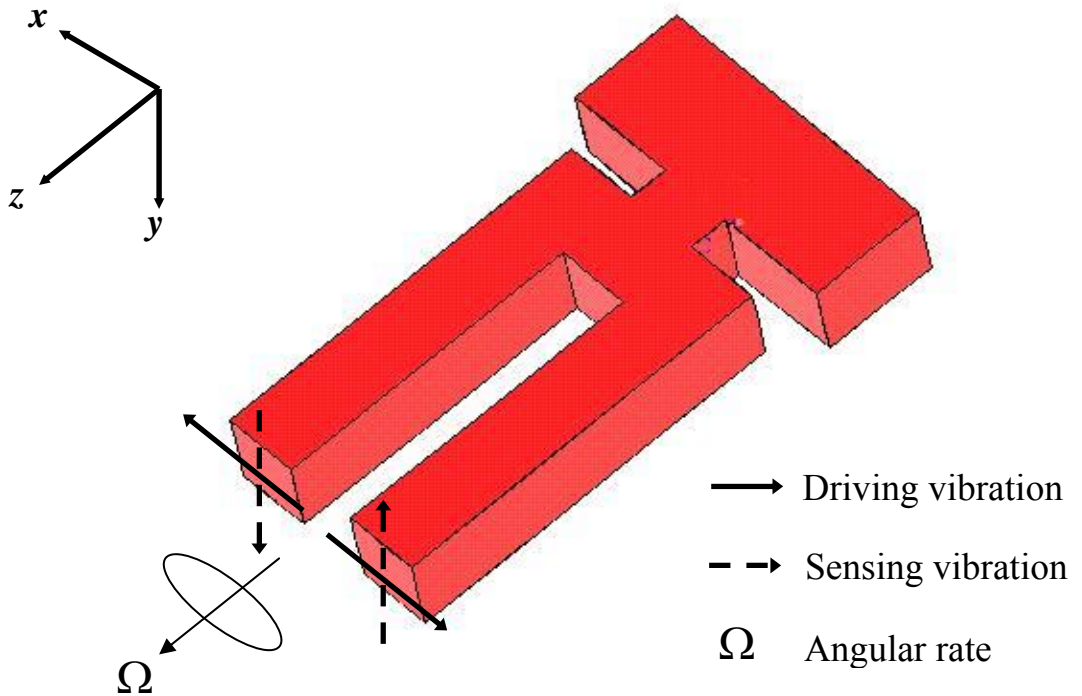


Figure 2.2 Tuning fork gyroscope.

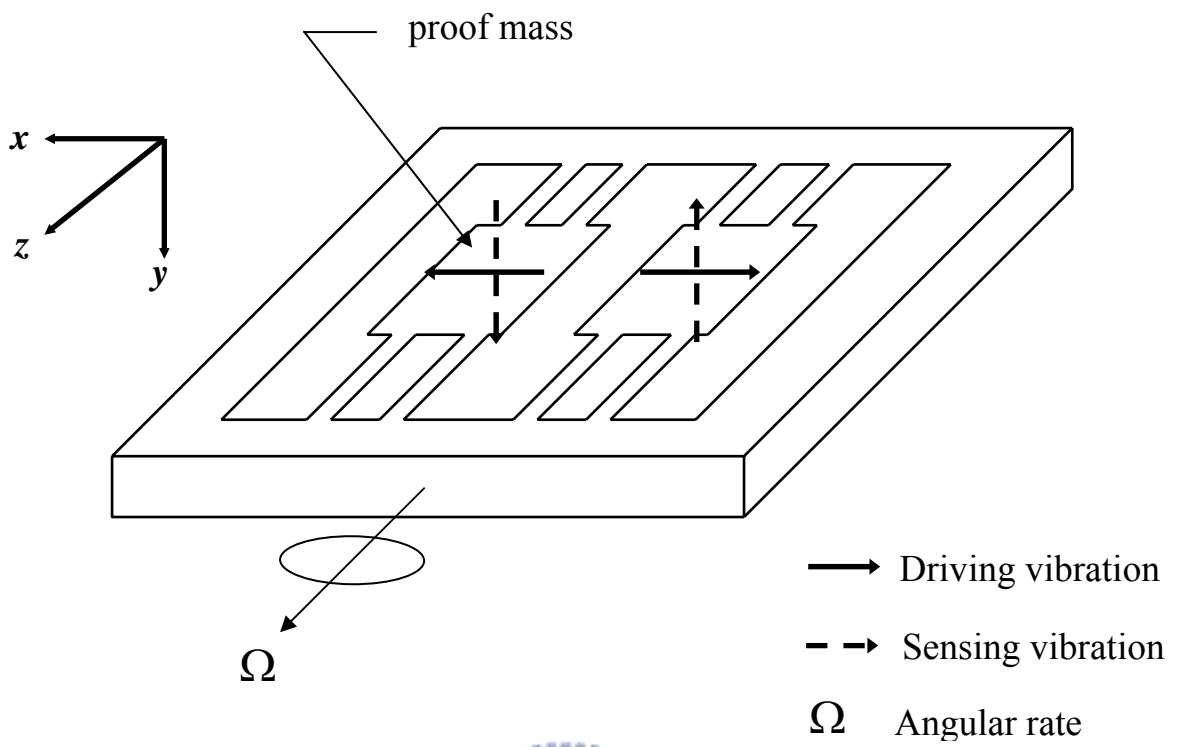


Figure 2.3 Dual accelerometer gyroscope.

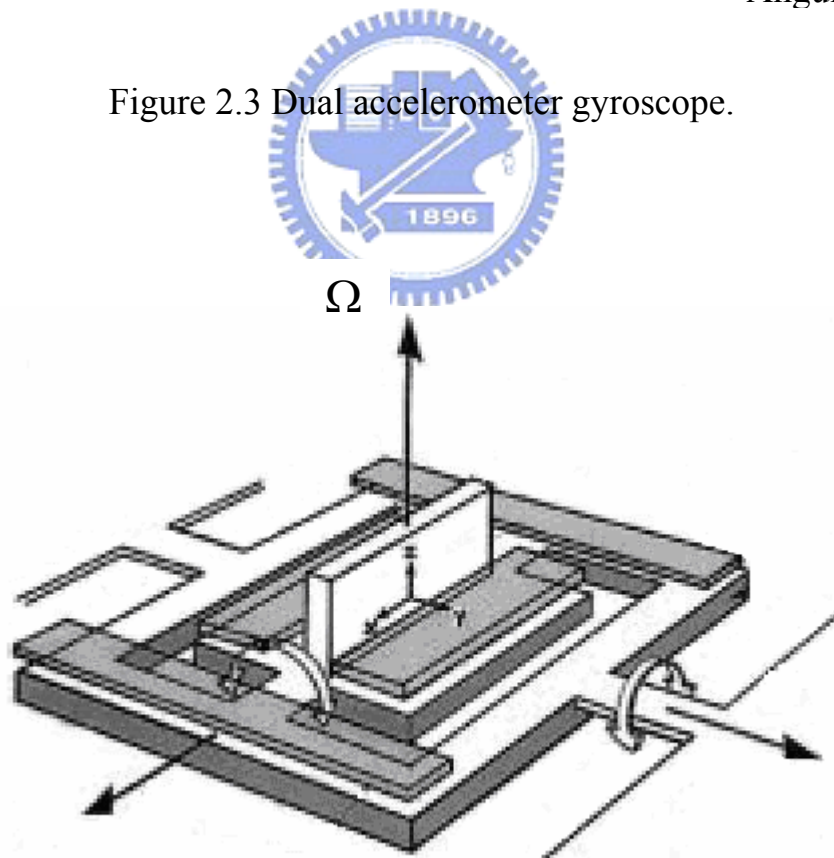


Figure 2.4 Double gimbal vibrating gyroscope.

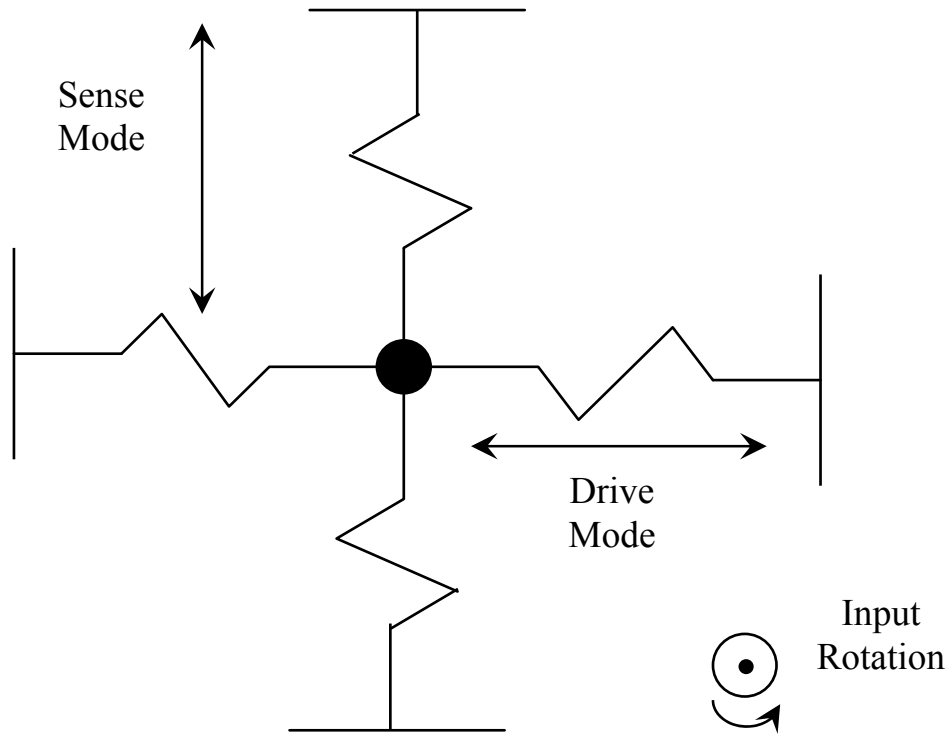


Figure 2.5 Schematic diagram for z-axis vibrating gyroscope.

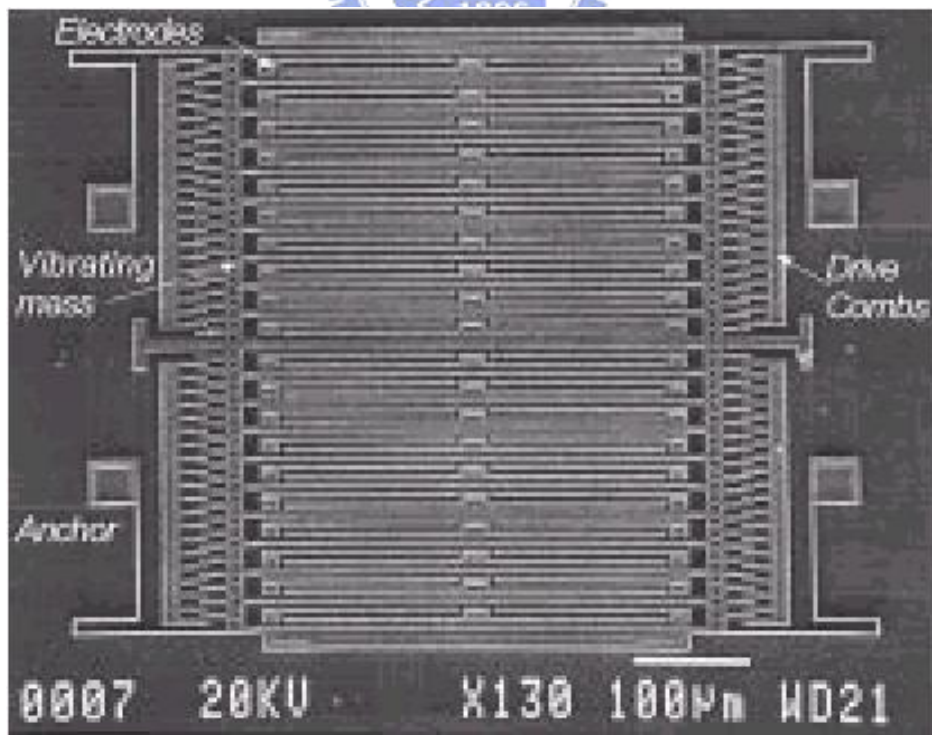


Figure 2.6 Z-axis vibrating gyroscope.

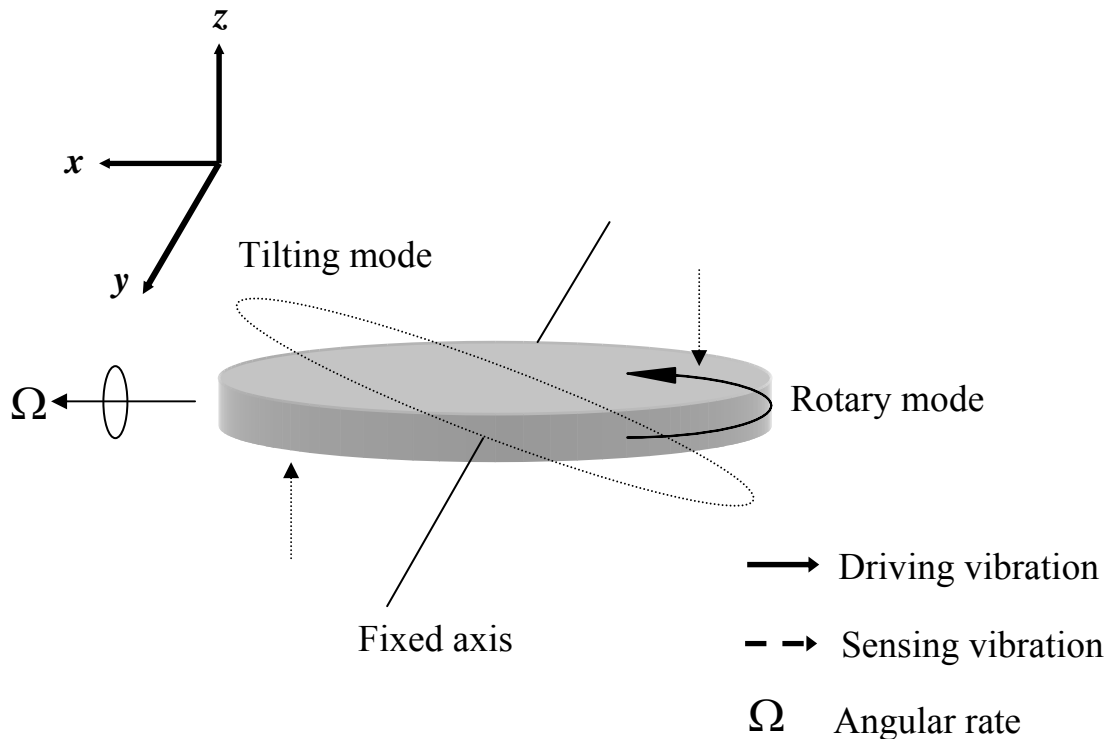


Figure 2.7 Schematic diagram for x-axis vibrating gyroscope.

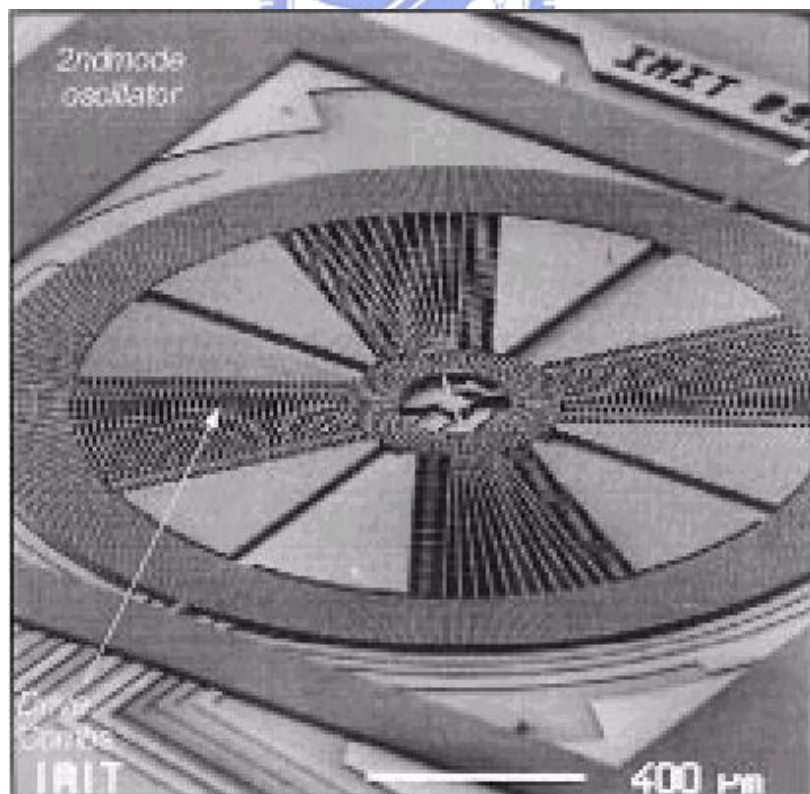


Figure 2.8 X-axis vibrating gyroscope.

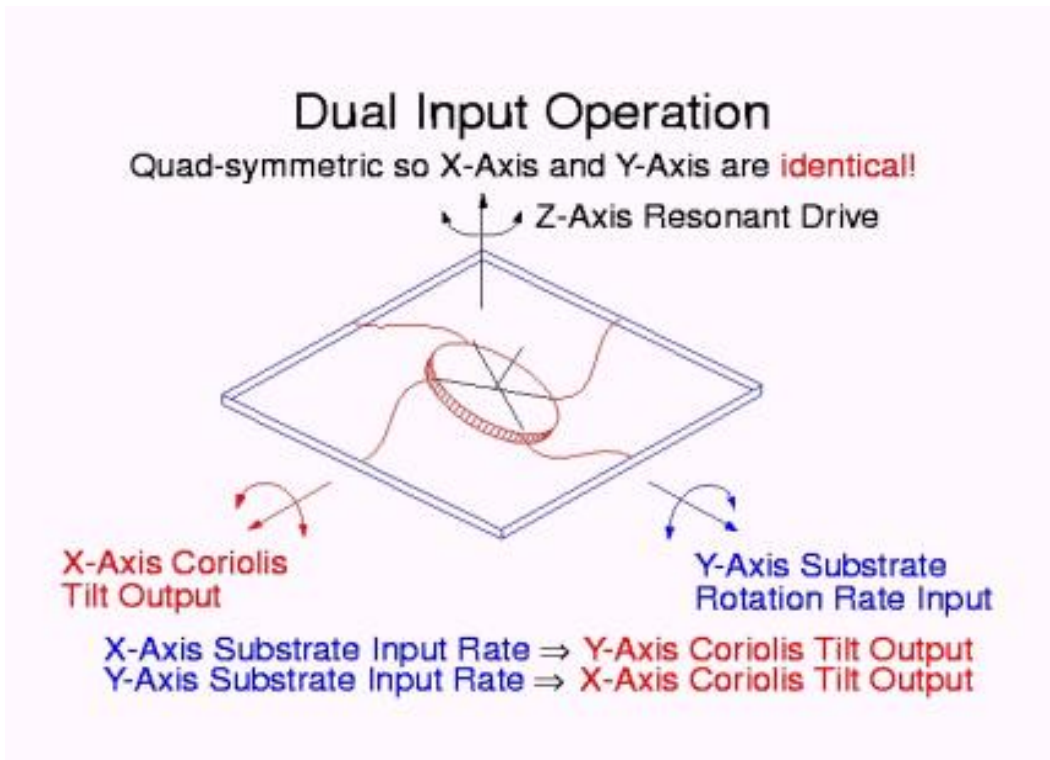


Figure 2.9 Schematic diagram for dual-axis vibrating gyroscope.

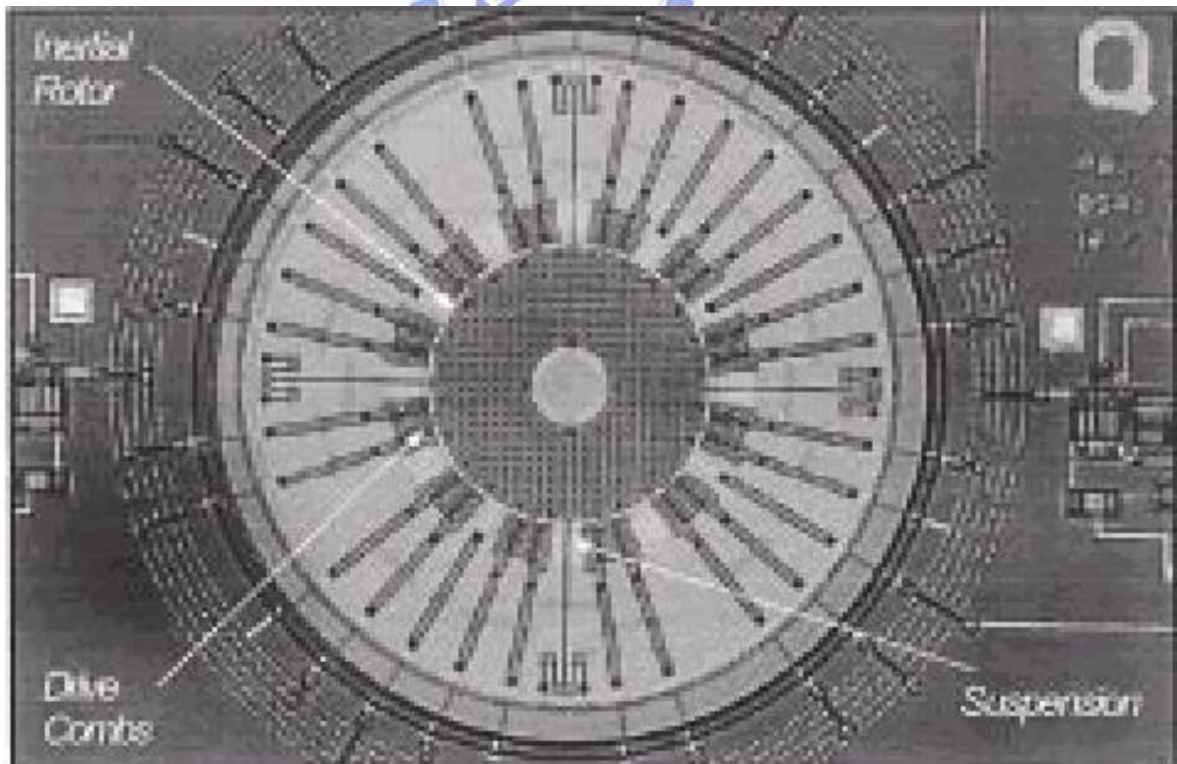


Figure 2.10 Dual-axis vibrating gyroscope.

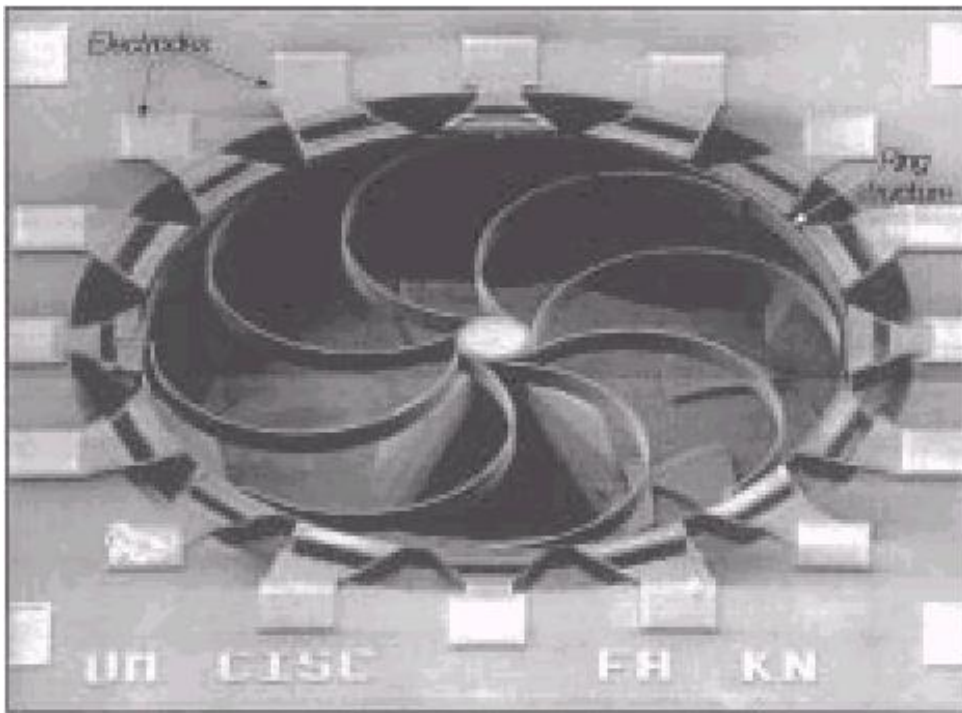


Figure 2.11 Poly-silicon vibrating ring gyroscope (PRG).

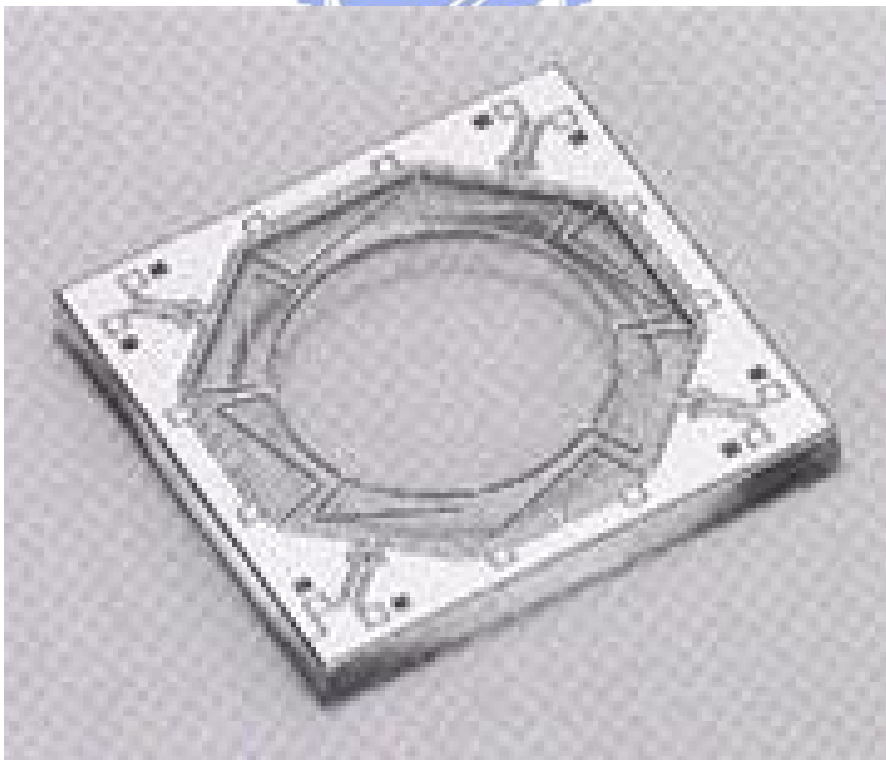
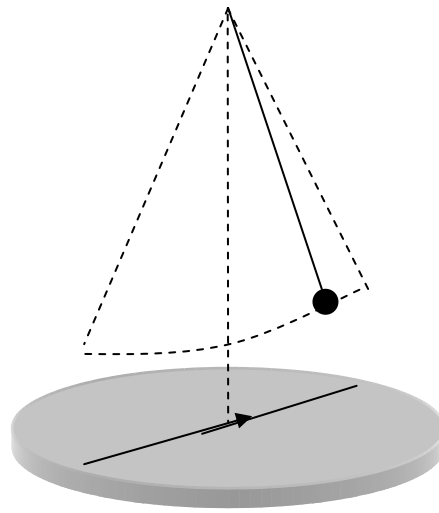
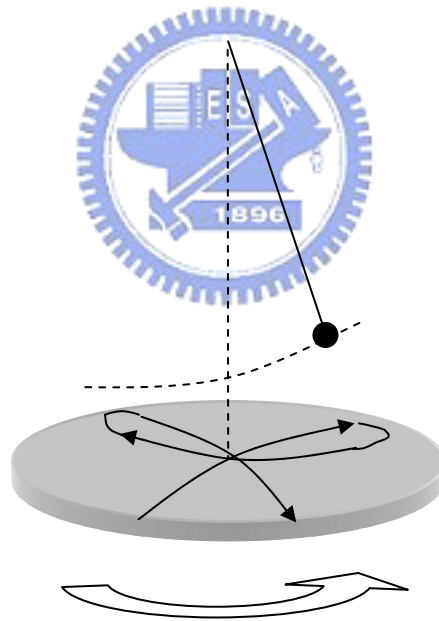


Figure 2.12 Vibrating ring gyroscope (Si-VSG).



(a)



(b)

Figure 2.13 Simple pendulum and its projection on: (a) fixed frame; (b) rotating frame.

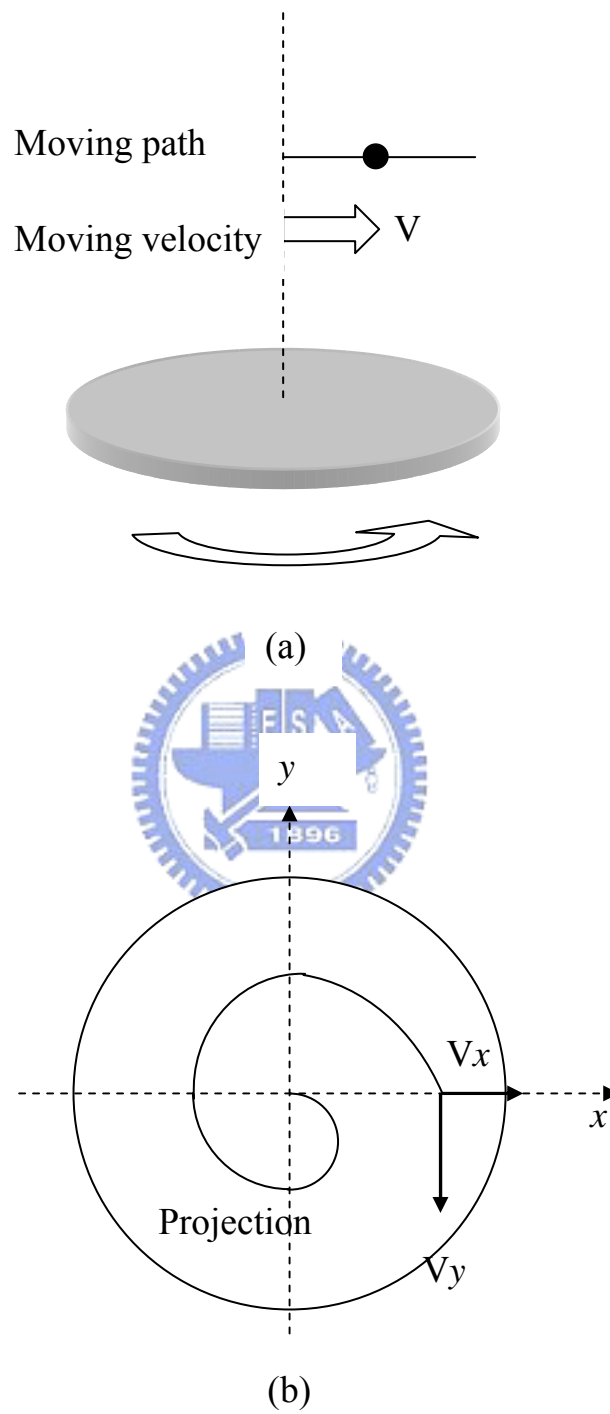


Figure 2.14 (a) A particle moves above a rotating frame; (b) the path projection on the rotating frame.

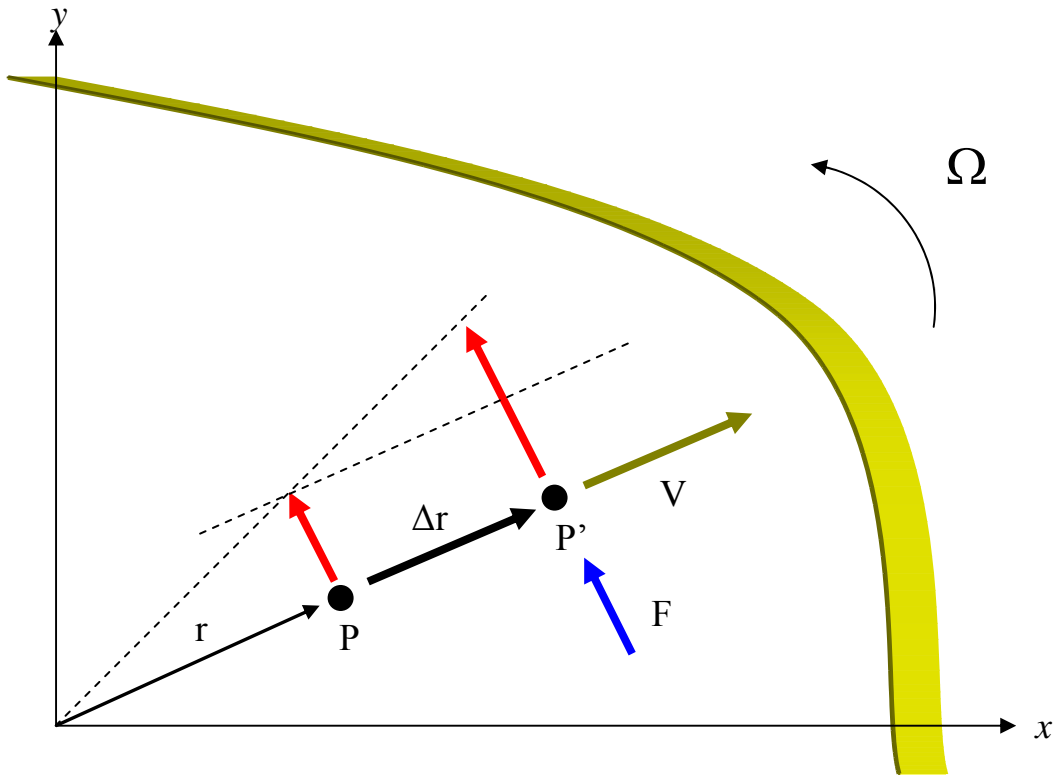


Figure 2.15 The frame rotates counterclockwise and a particle P moves on it with velocity.

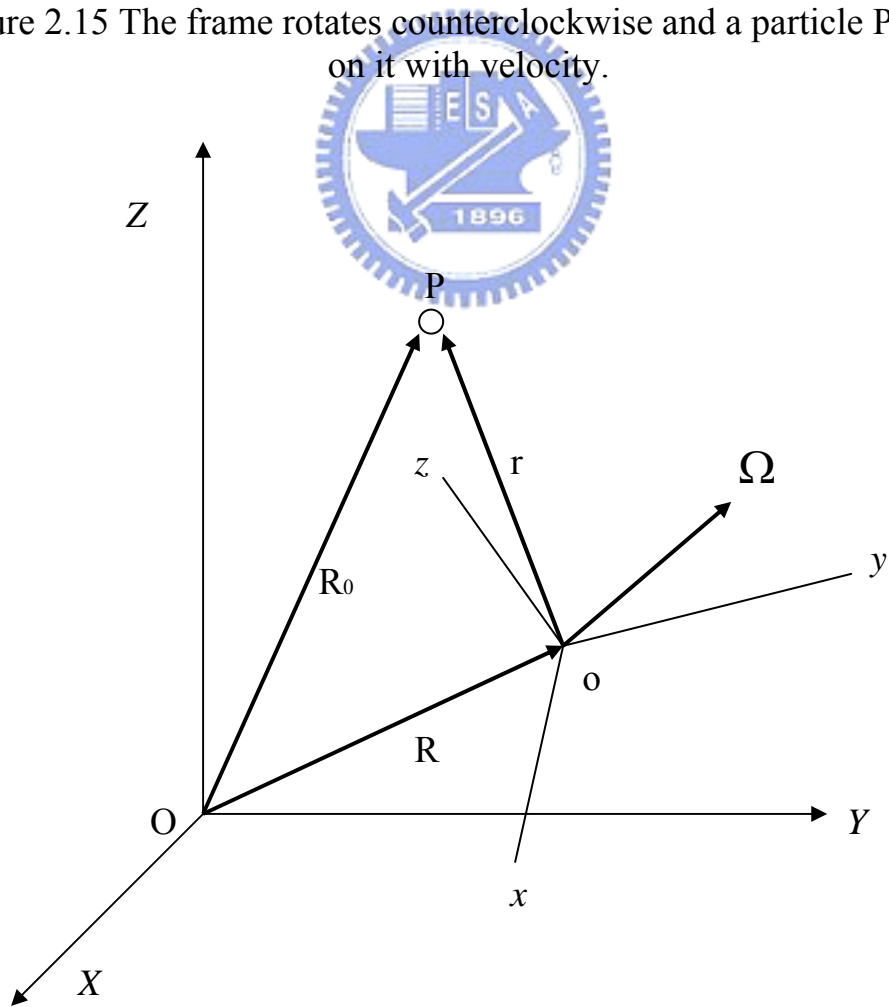


Figure 2.16 The position vector of a point P relative to a rotating system.

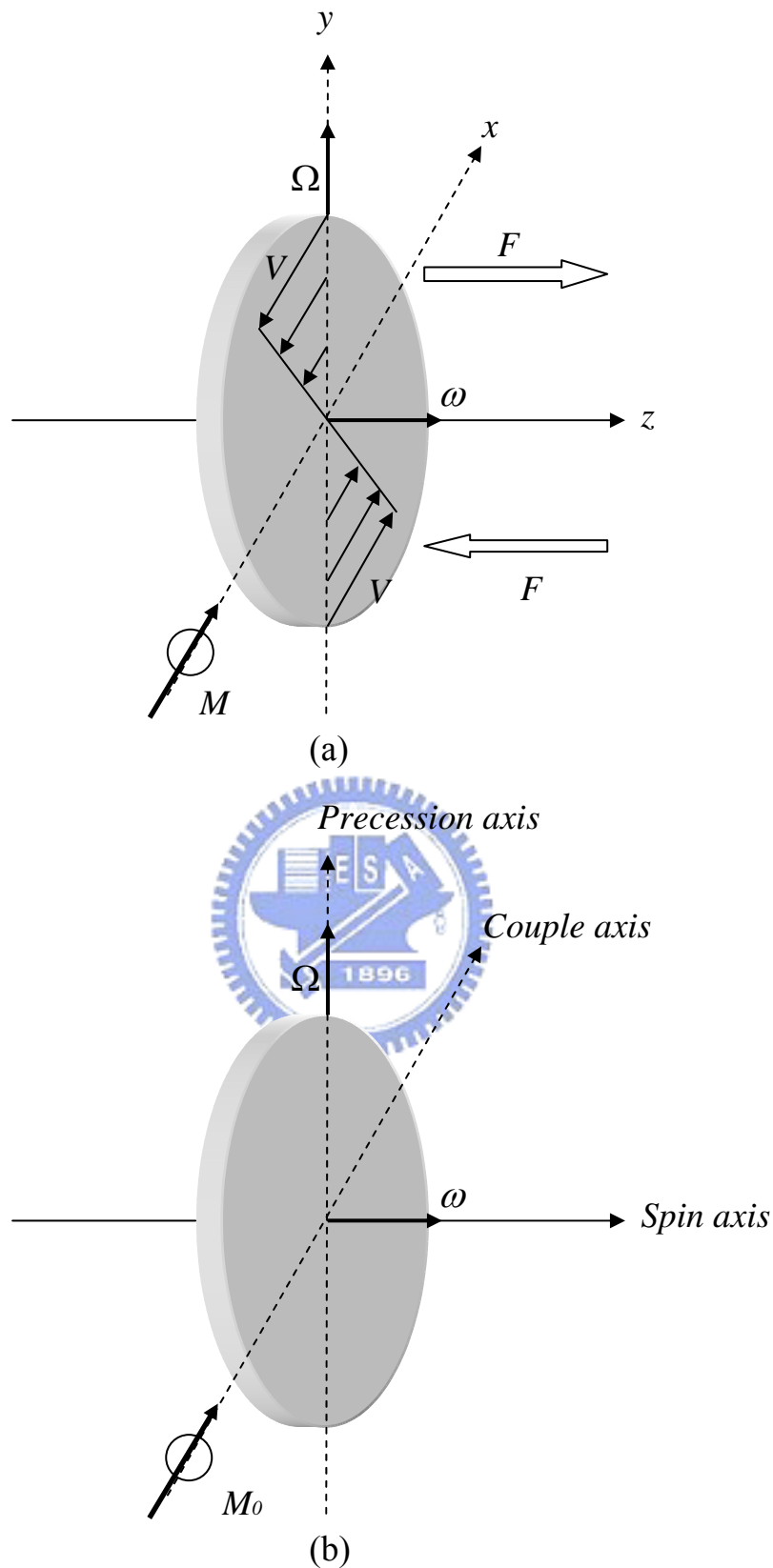


Figure 2.17 (a) The Coriolis force on a rotating disk; (b) the steady precession of a gyroscope.

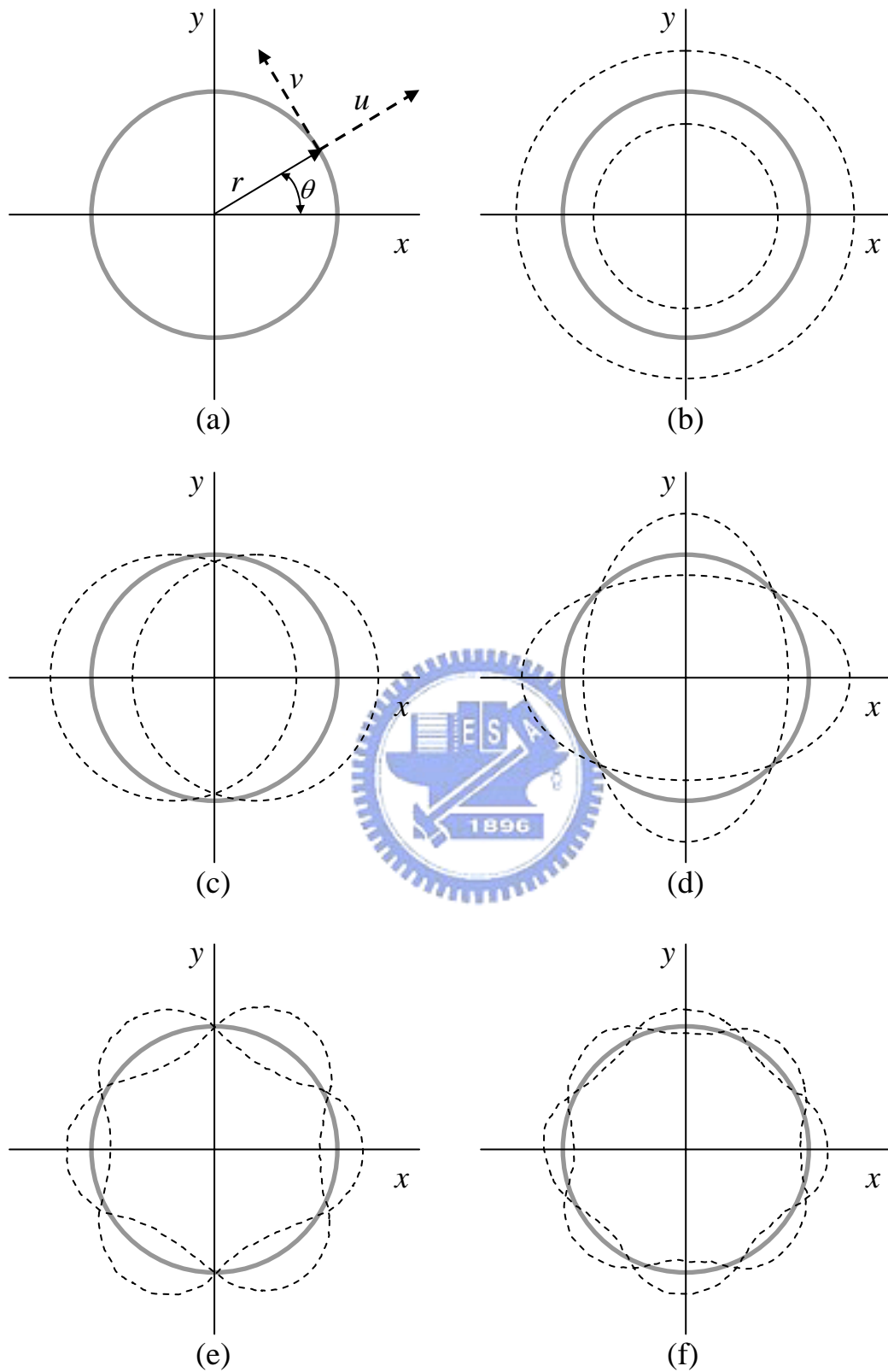


Figure 3.1 (a) The radial displacement u and tangential displacement v for the circular ring; (b) $n=0$; (c) $n=1$; (d) $n=2$; (e) $n=3$; (f) $n=4$.

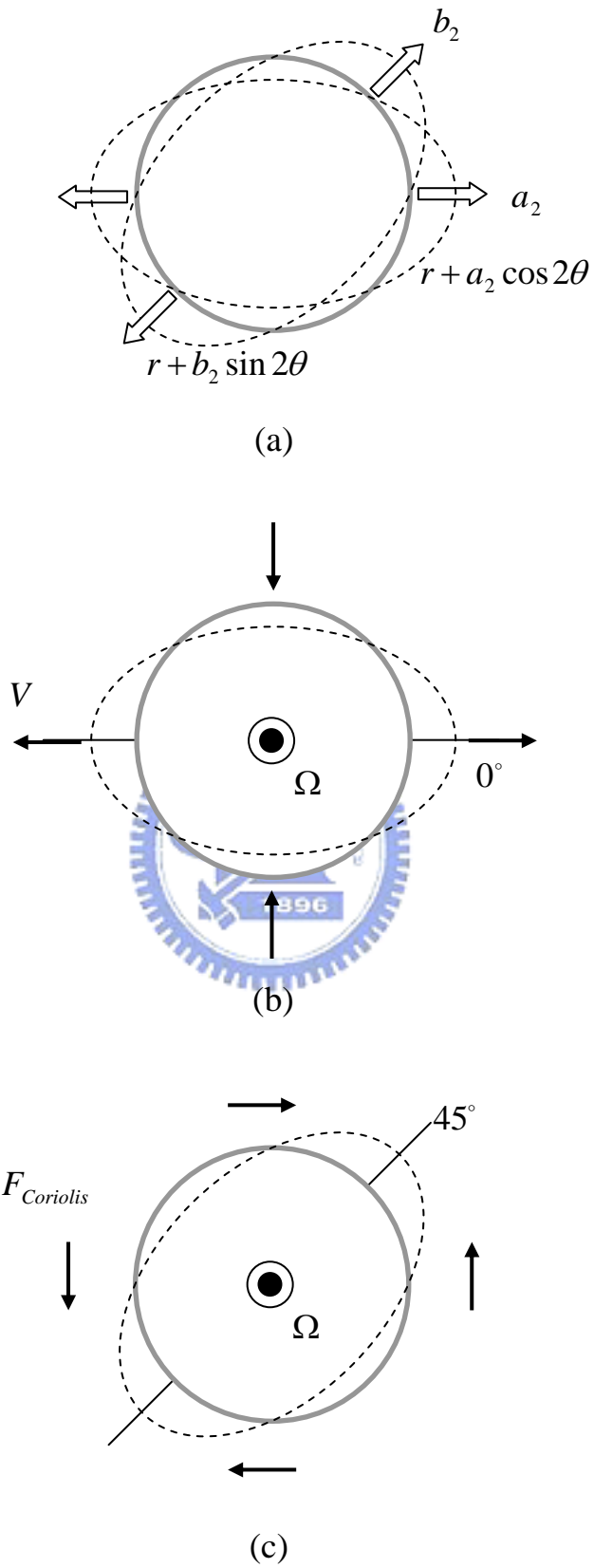


Figure 3.2 (a) The 2nd mode vibration shapes and its generalized coordinates; (b) the primary mode on 0 degree axis; (c) the secondary mode result from Coriolis force on 45 degree axis.

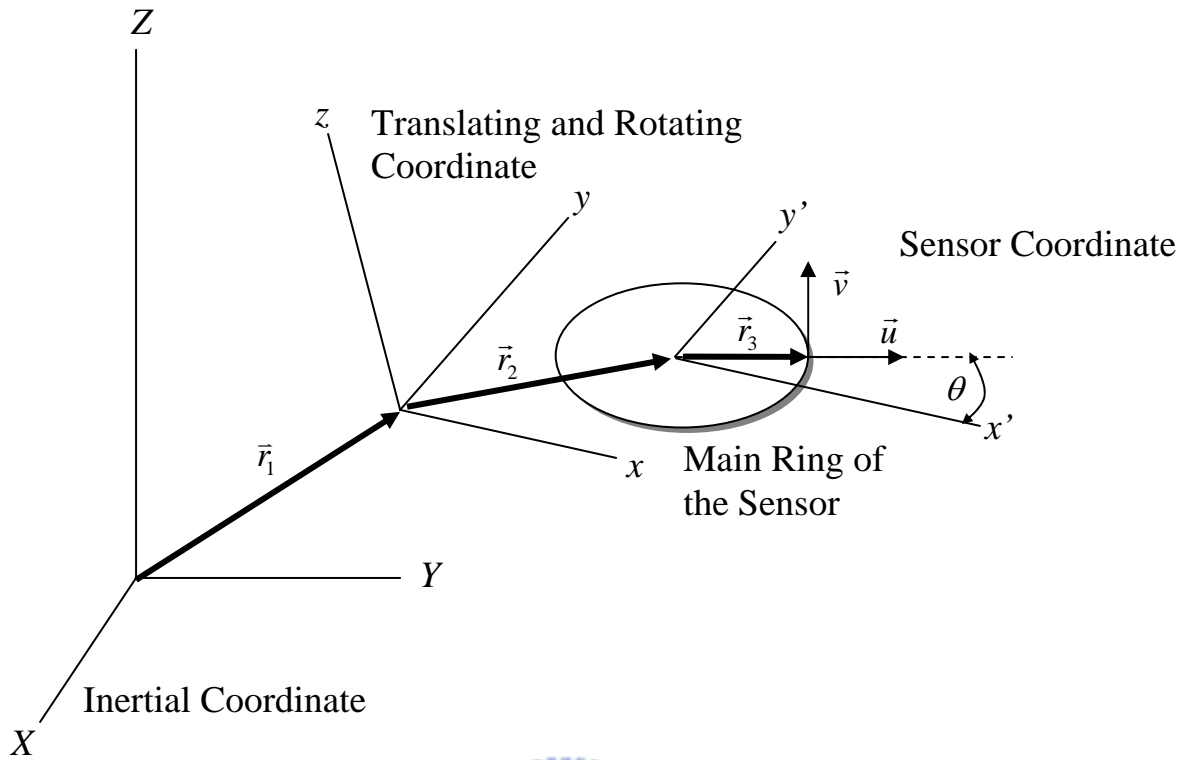


Figure 3.3 Coordinate system of the sensor.

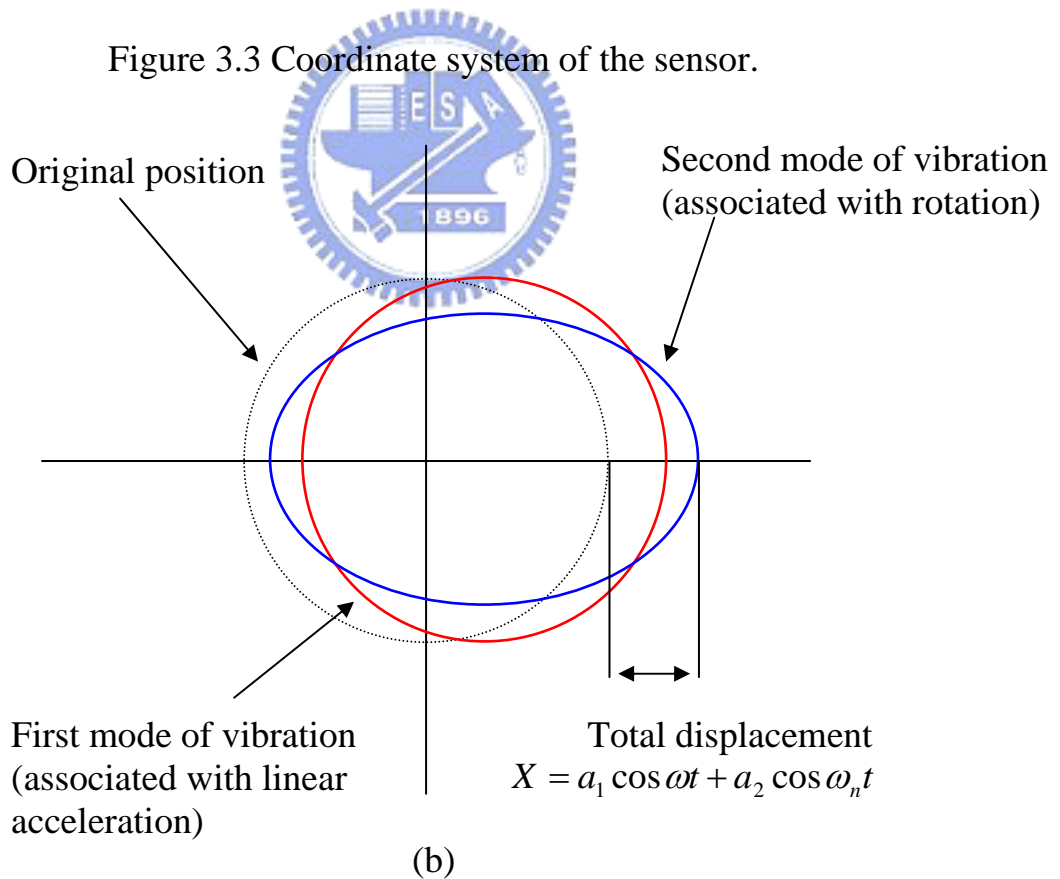
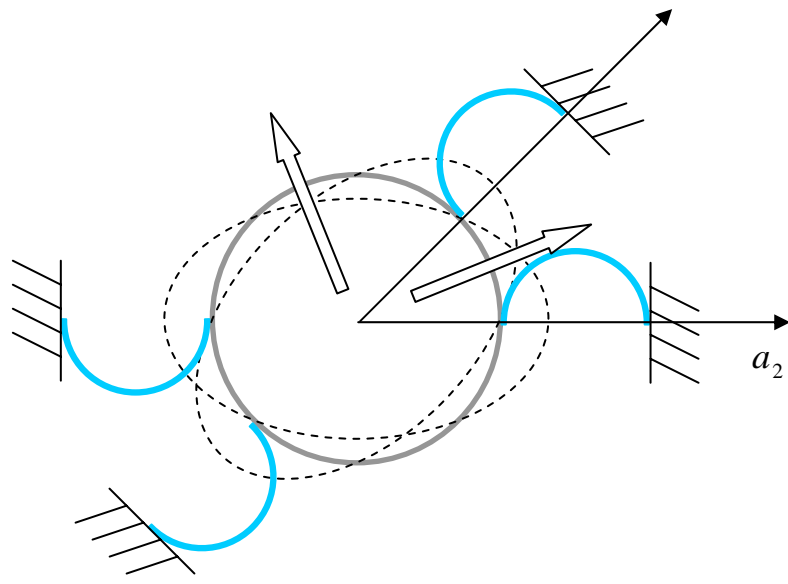
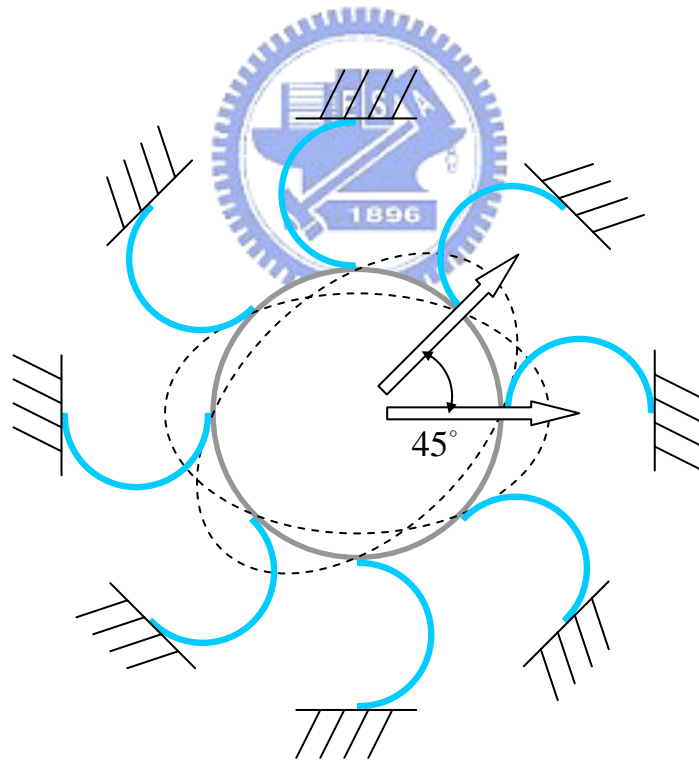


Figure 3.4 Motion of the ring, comprising first and second modes of vibration.

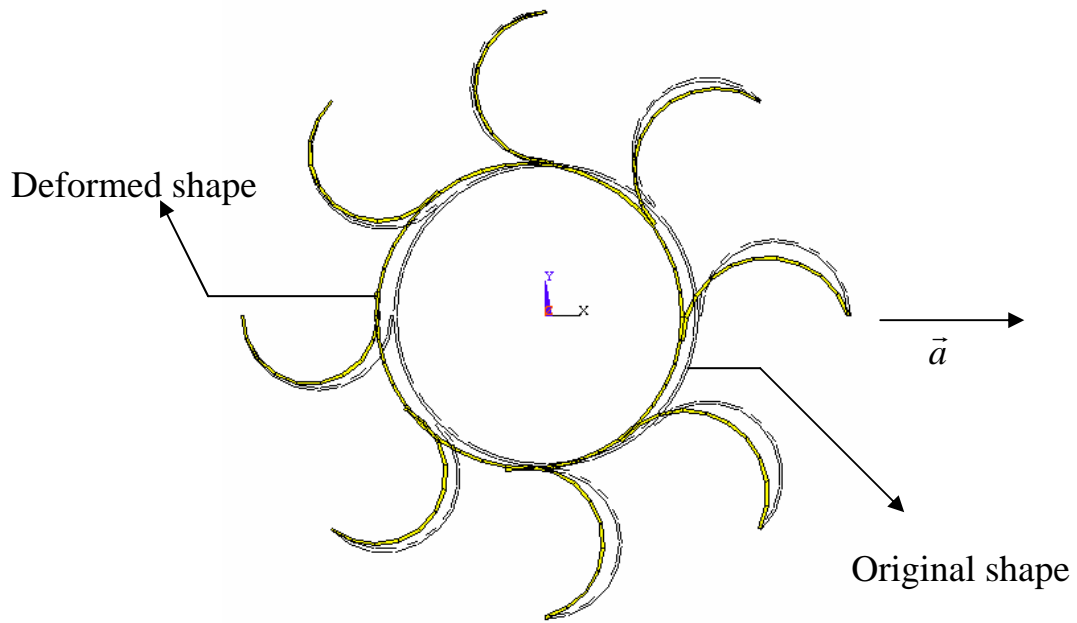


(a)

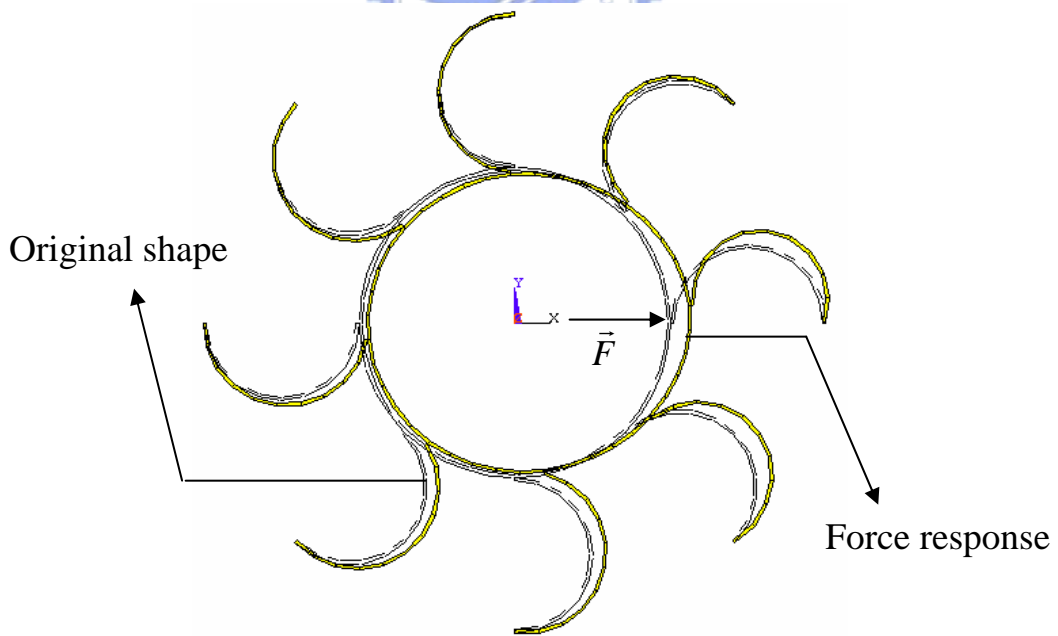
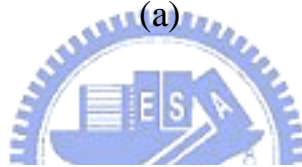


(b)

Figure 3.5 Supports arrangement (a) four supports; (b) eight supports.



(a)



(b)

Figure 3.6 (a) Structural deformed due to linear acceleration along x-axis;
 (b) force response for the force applied at one point positive to x-axis.

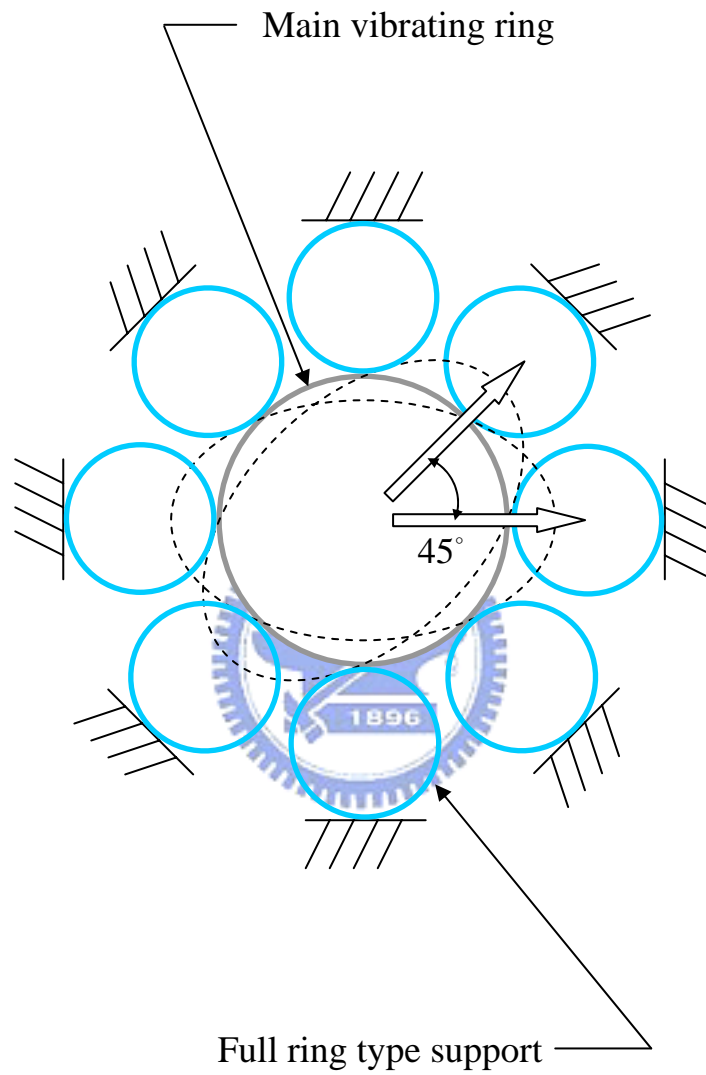


Figure 3.7 The vibrating ring gyroscope with symmetry support and symmetry arrangement.

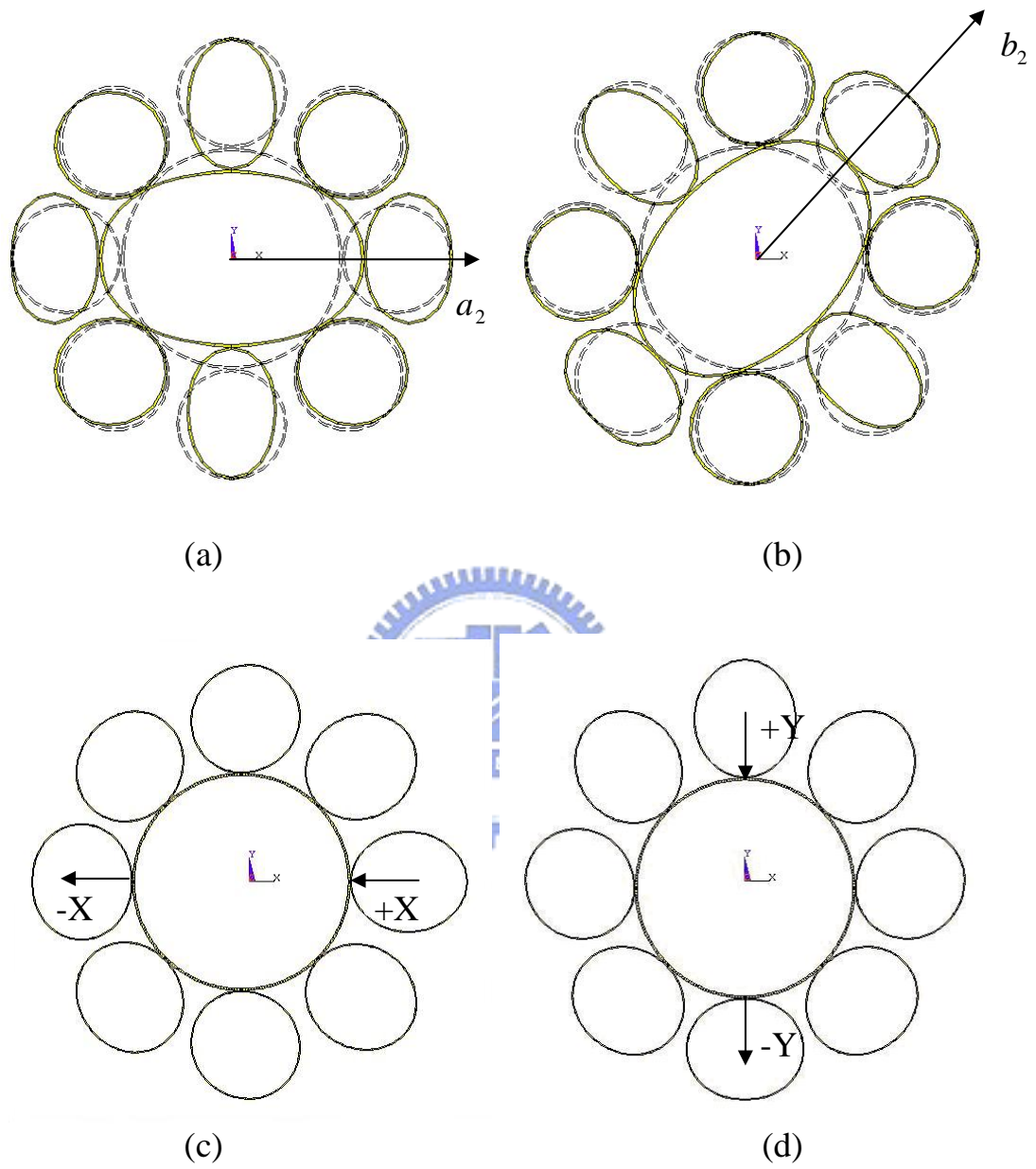
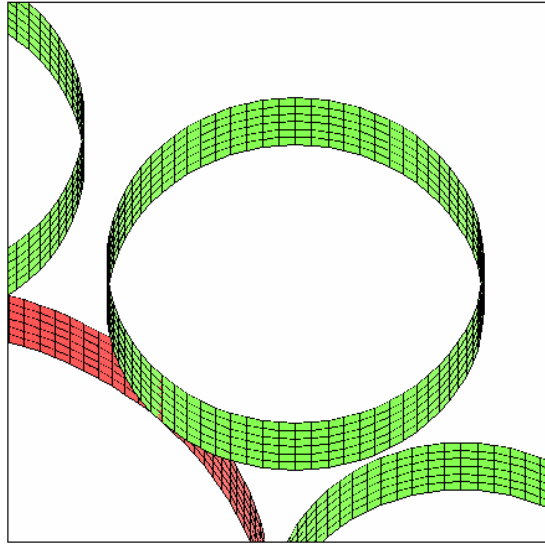
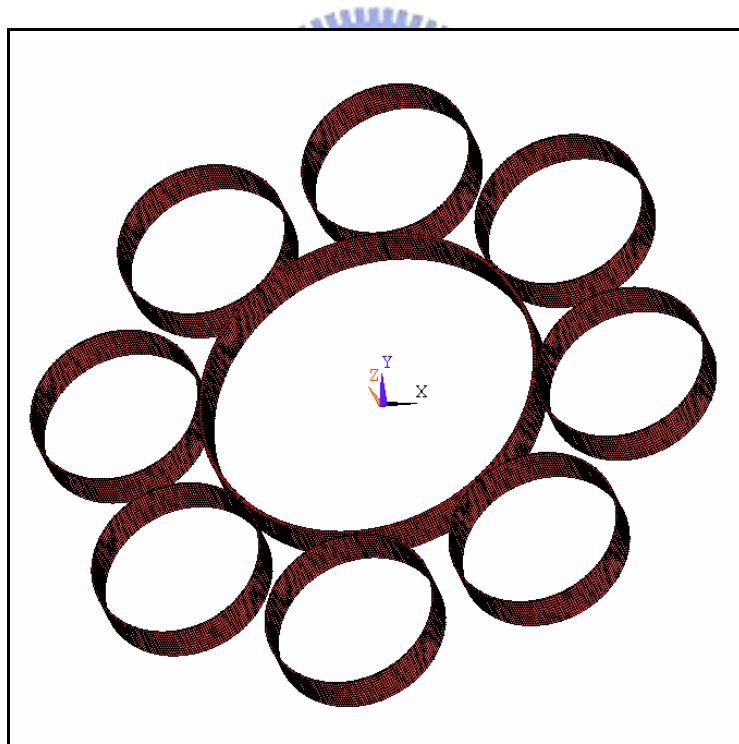


Figure 3.8. (a)(b)Scheme for detecting rotation of gyroscope; (c)(d) scheme for detecting linear acceleration of accelerometer.

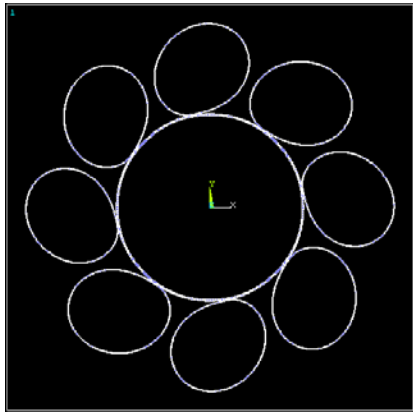


(a)

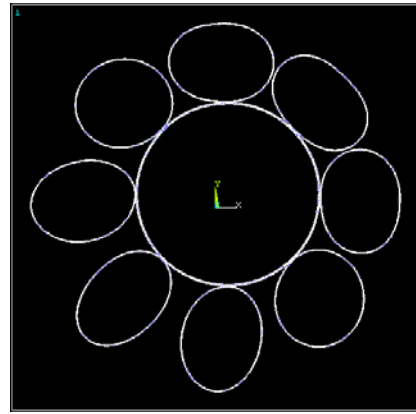


(b)

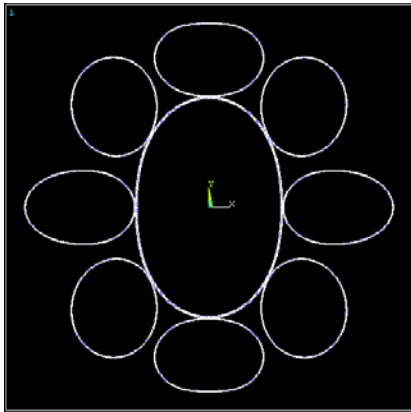
Figure 3.9 Finite element analysis: (a) the part of the structure modeled by quadrilateral shell elements and (b) full view of the meshed structure.



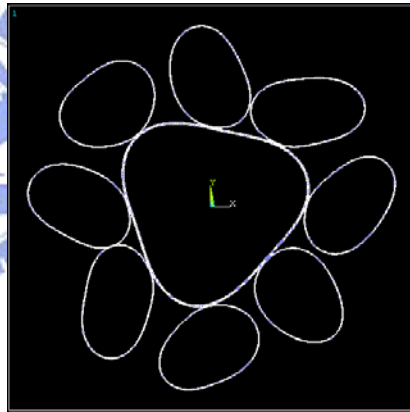
(a) 13628Hz



(b) 13651Hz

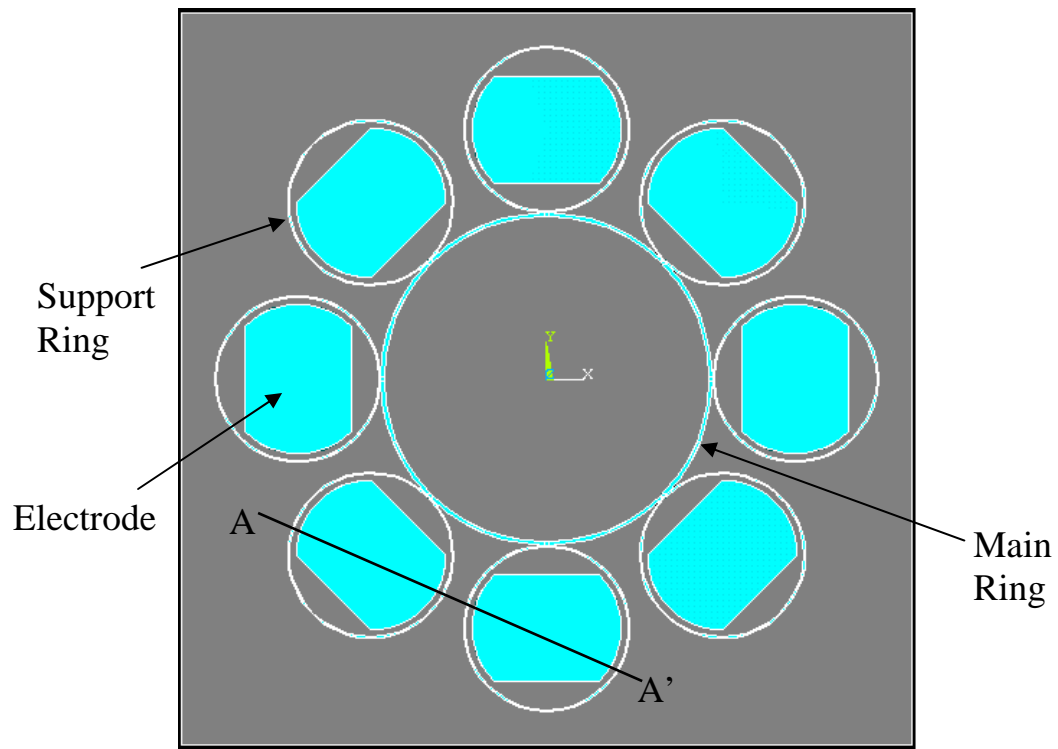


(c) 22823Hz

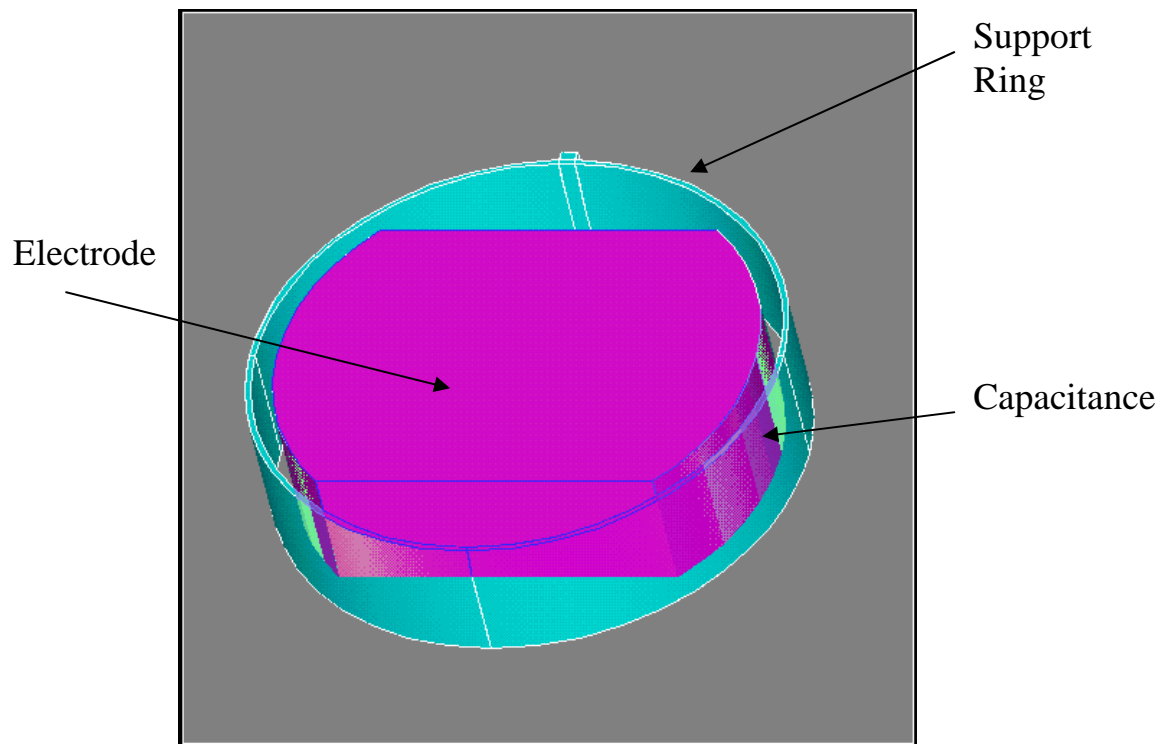


(d) 43615Hz

Figure 3.10 Mode shape of the structure (a) rotation mode; (b) plane motion mode; (c) 2nd vibration mode; (d) 3rd vibration mode.



(a)



(b)

Figure 4.1 (a) Top view of structure with electrode; (b) detail view of support with electrode.

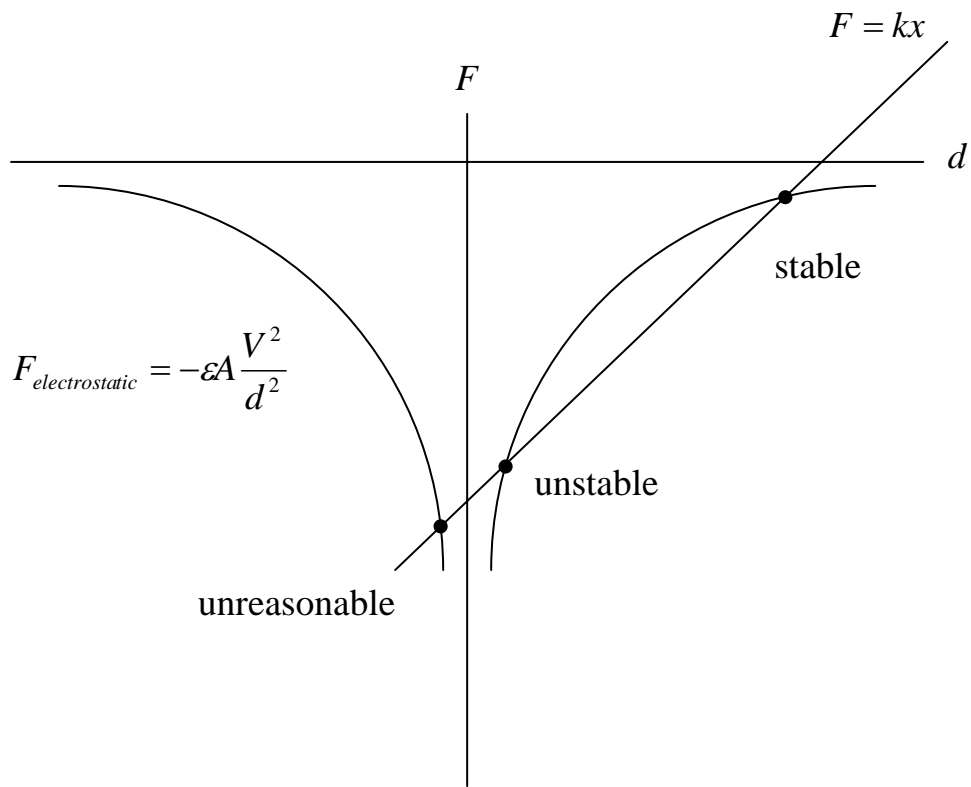


Figure 4.2 Intersects of electrostatic force and structure rebalance force.

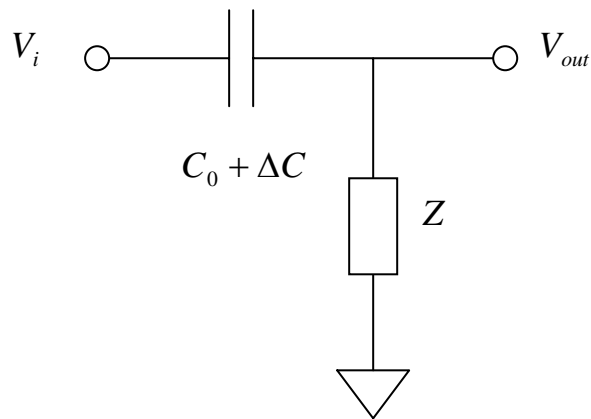
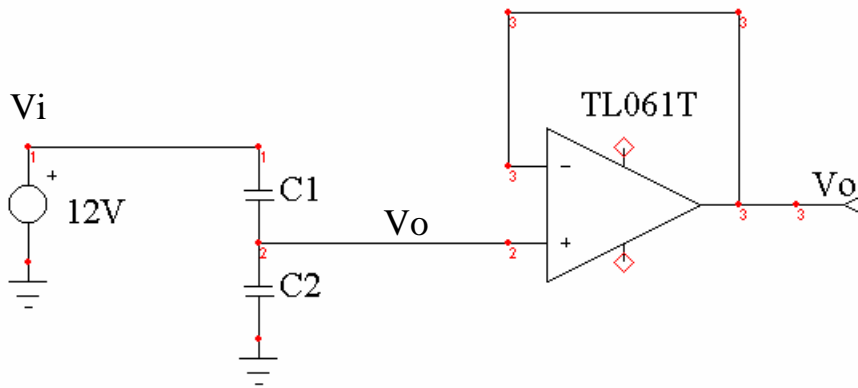
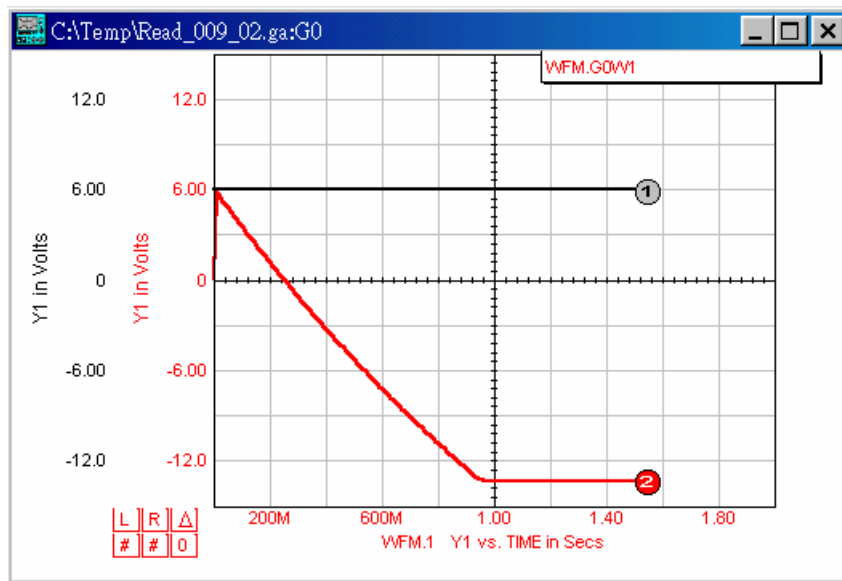


Figure 4.3 The variable capacitor connected to the detection circuit represented by an impedance.

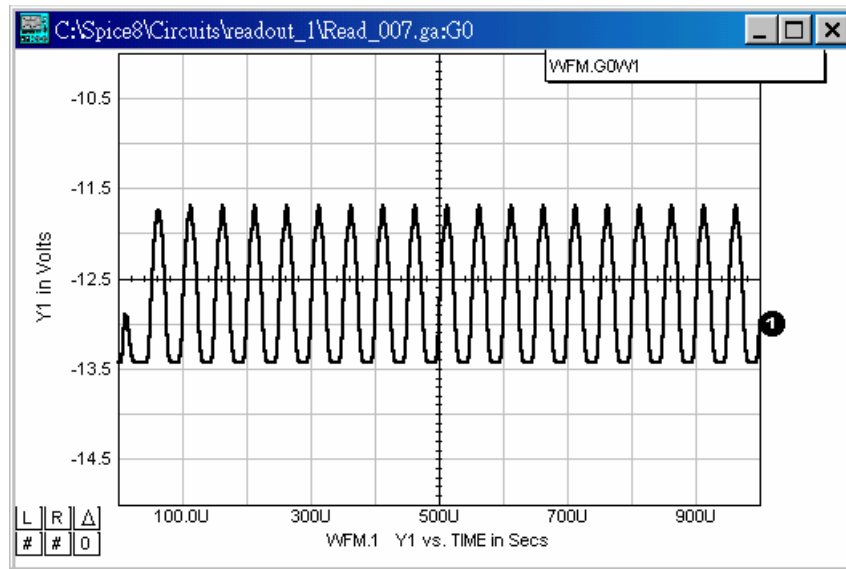


(a)

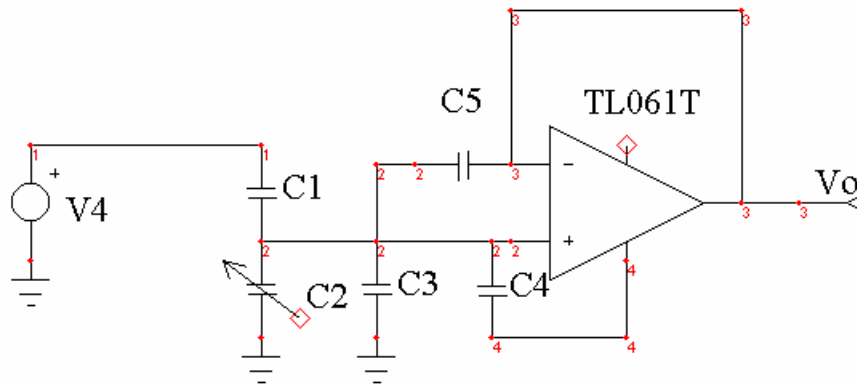


(b)

Figure 4.4 (a) Schematic diagram for detection scheme; (b) output voltage plot for 1n farad (line 1) and 1p farad (line 2).

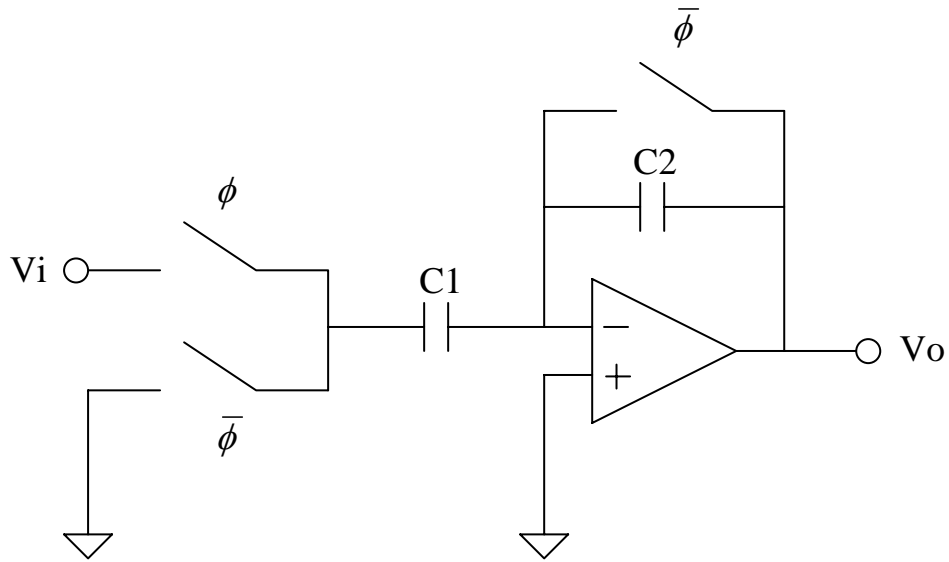


(a)



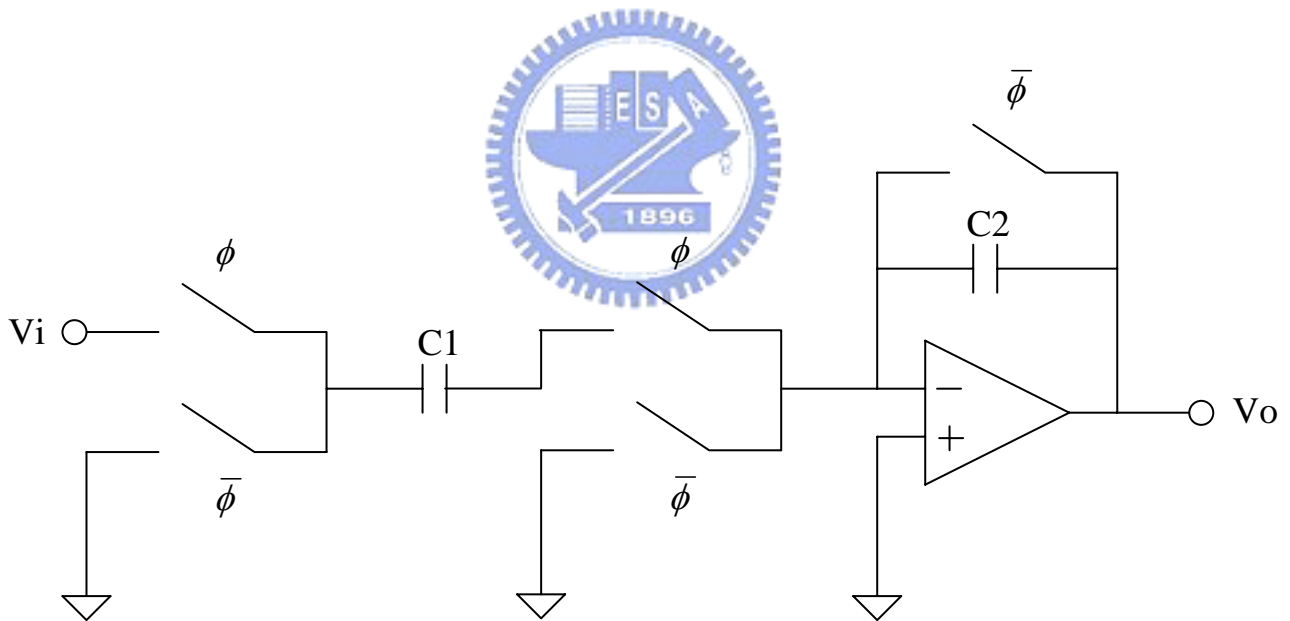
(b)

Figure 4.5 (a) Output voltage plot for variable capacitance C_2 ; (b) schematic diagram for detection with stray capacitance.



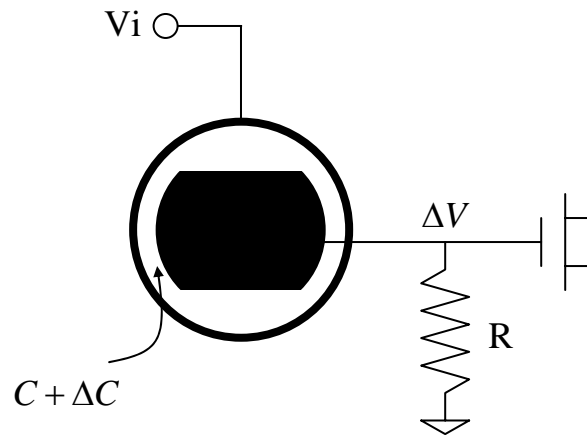
$$V_o = -V_i \frac{C_1}{C_2}$$

(a)

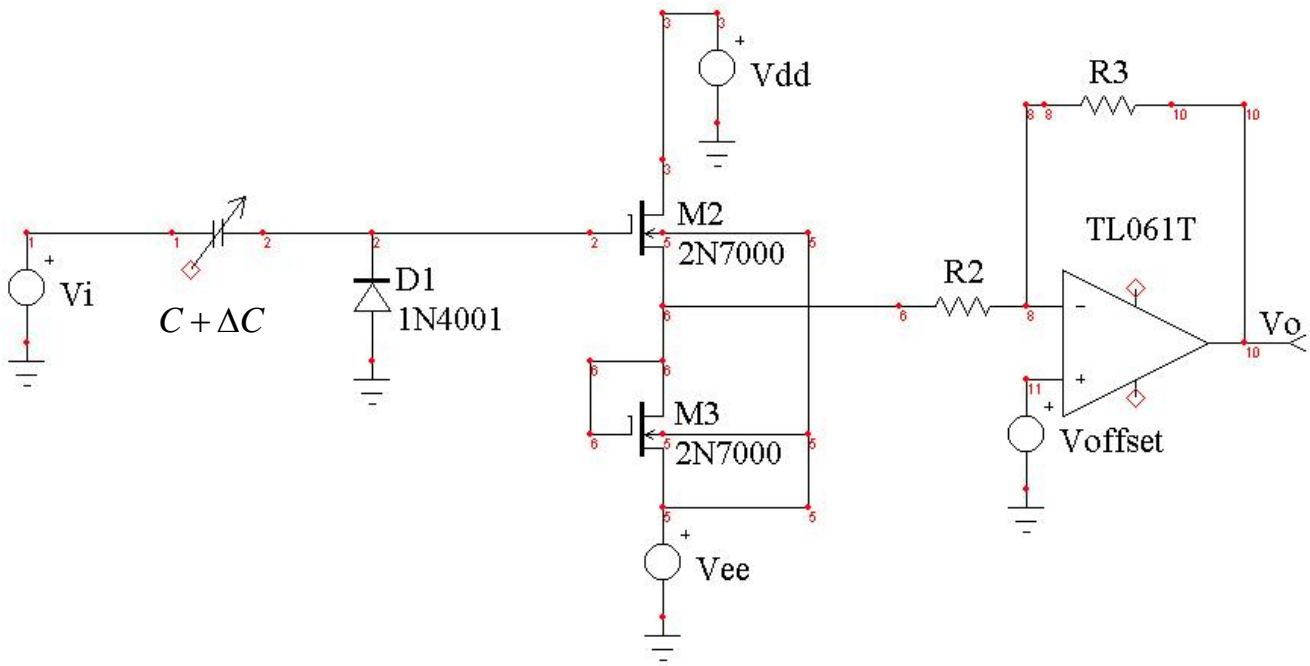


(b)

Figure 4.6 (a) Basic circuit for switched-capacitor; (b) stray-insensitive design.

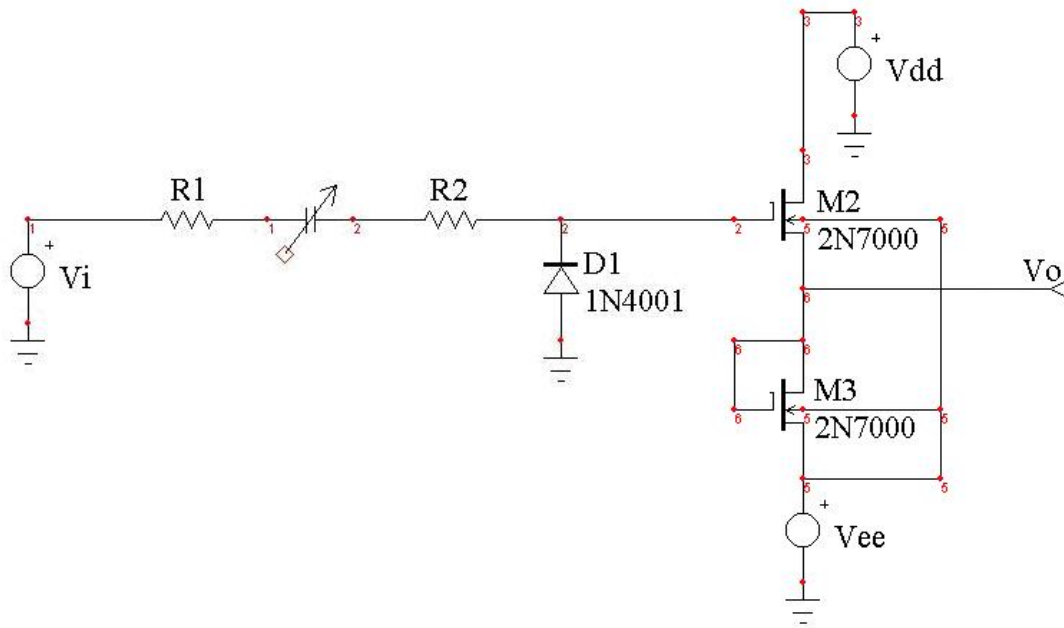


(a)

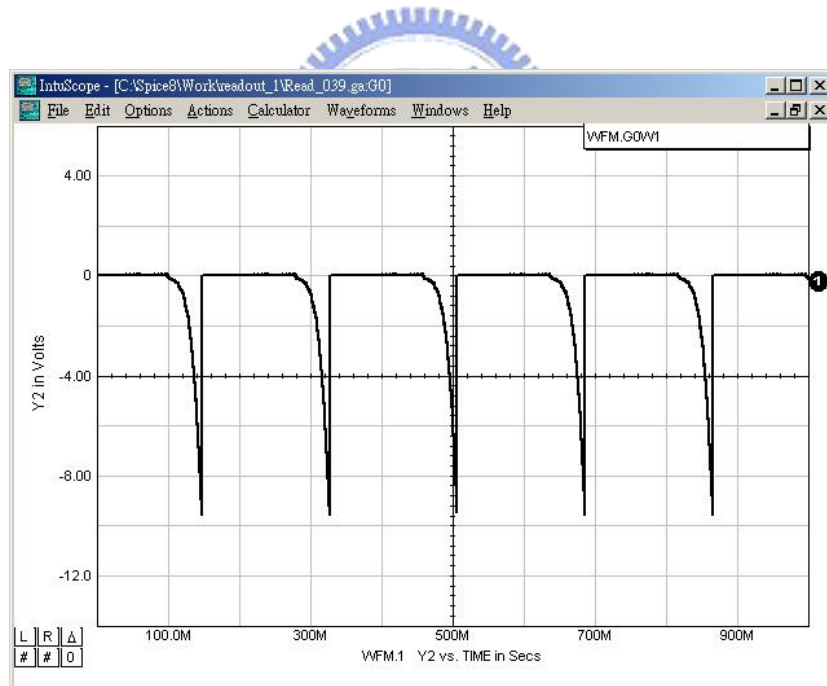


(b)

Figure 4.7 (a) Basic circuit for detection scheme; (b) schematic diagram for capacitive detection circuit.



(a)



(b)

Figure 4.8 (a) Schematic diagram for basic circuit with internal resistance; (b) output voltage plot shows periodical disturbance.

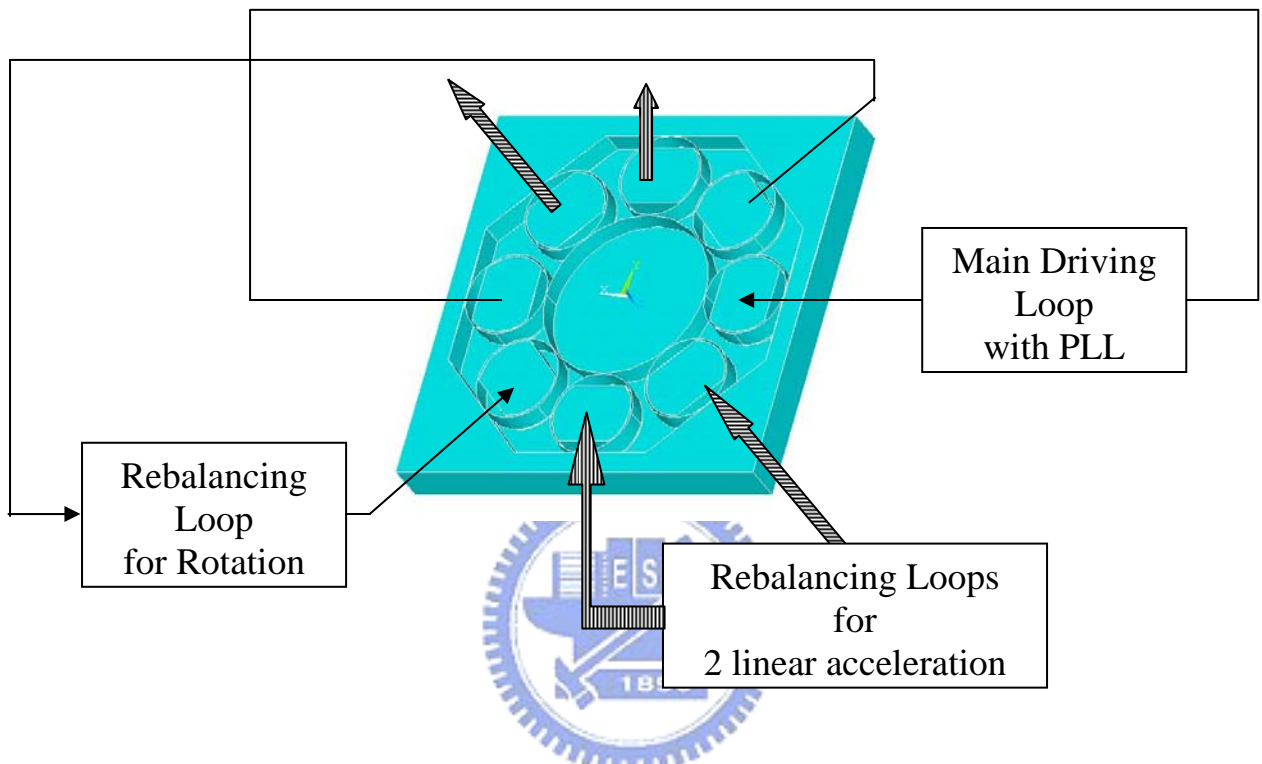
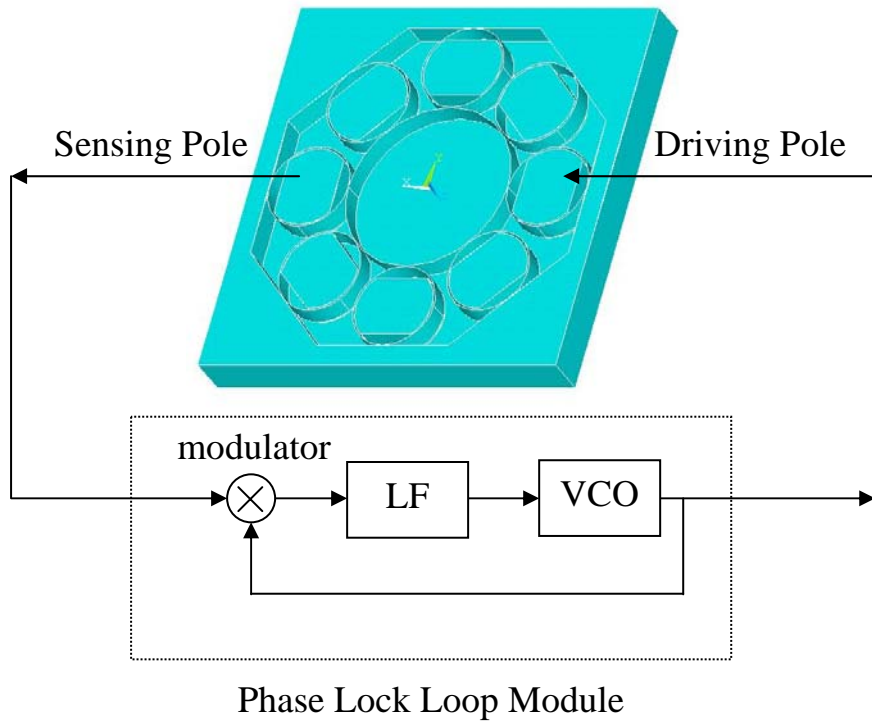
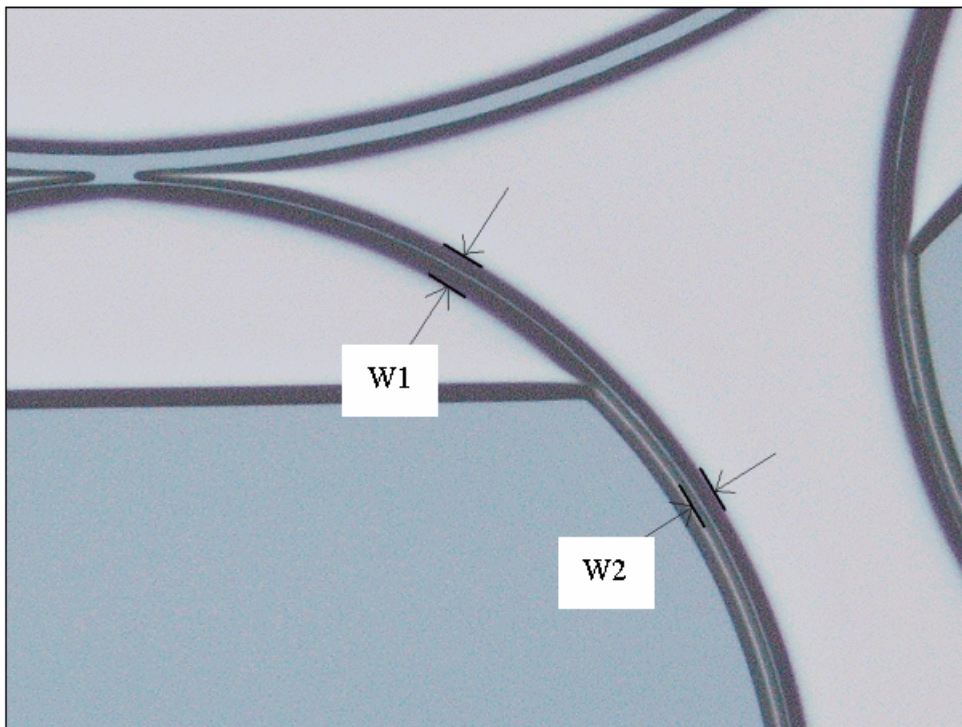


Figure 4.9 Schematic overview of control loops and structure.

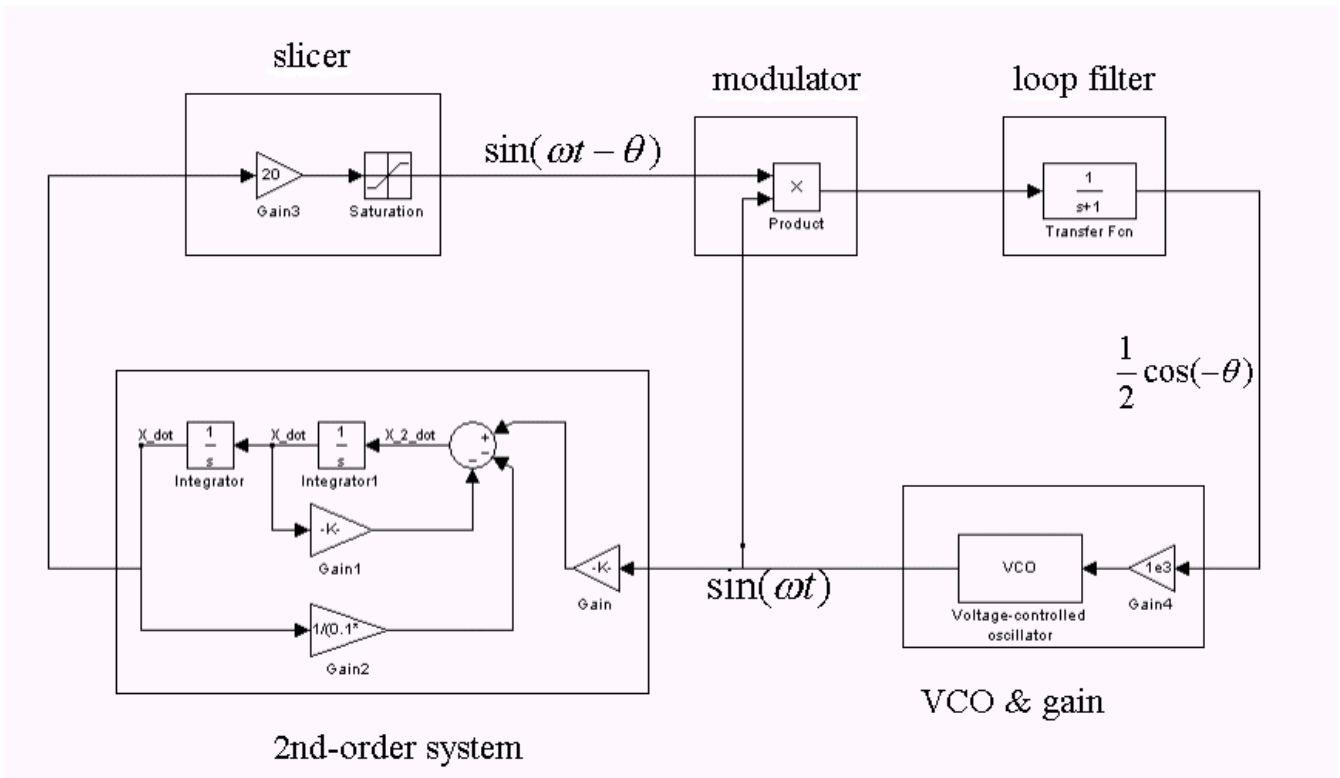


(a)

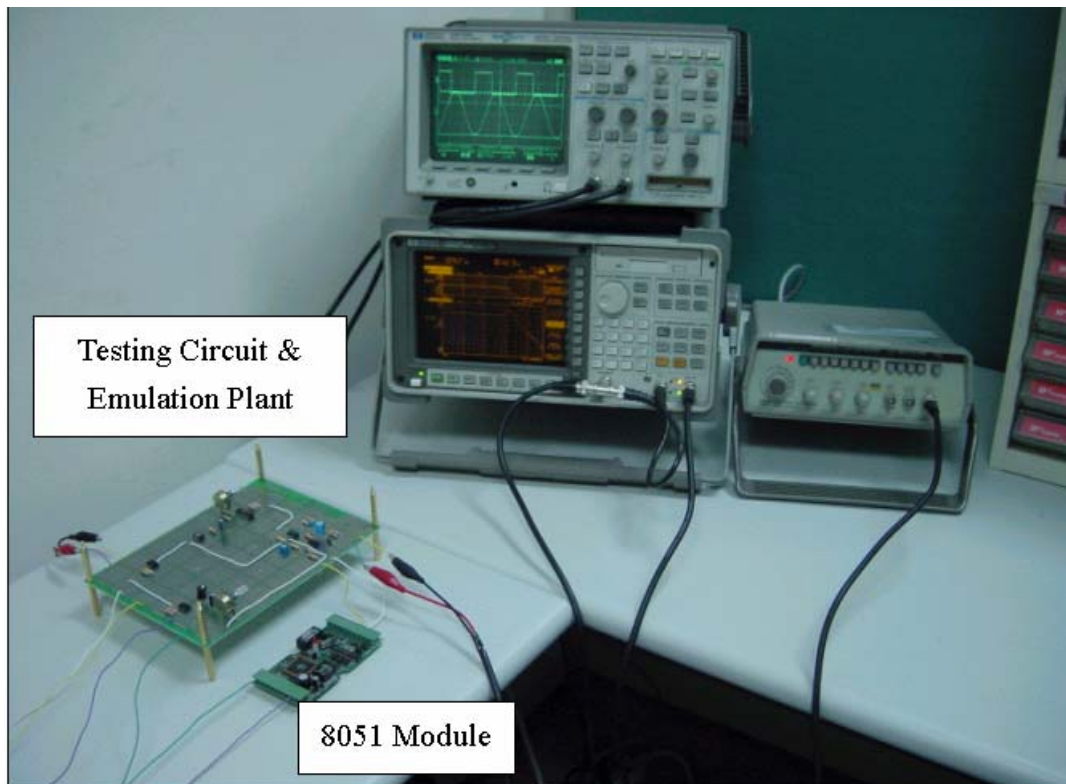


(b)

Figure 4.10 (a) Schematic diagram of microstructure with PLL driving circuit; (b) Silicon structure etched with RIE and observed with optical microscope (10 x 5).

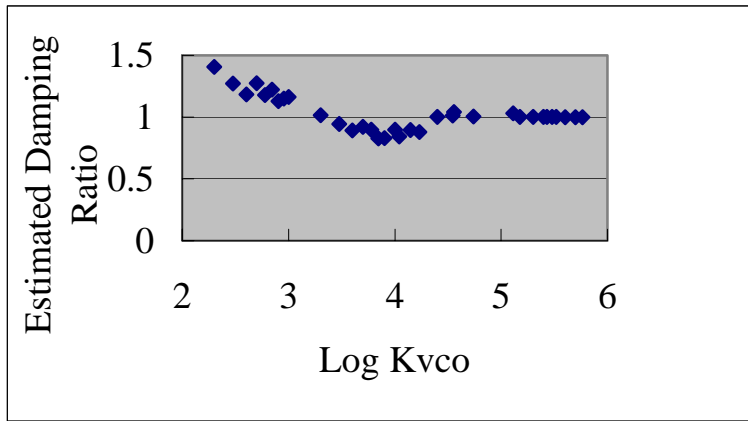


(a)

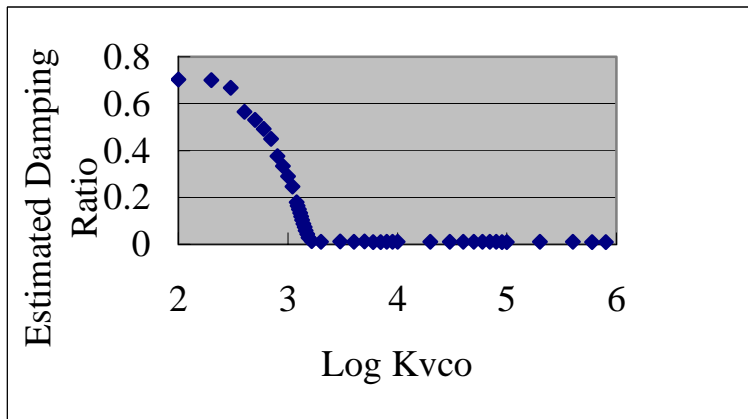


(b)

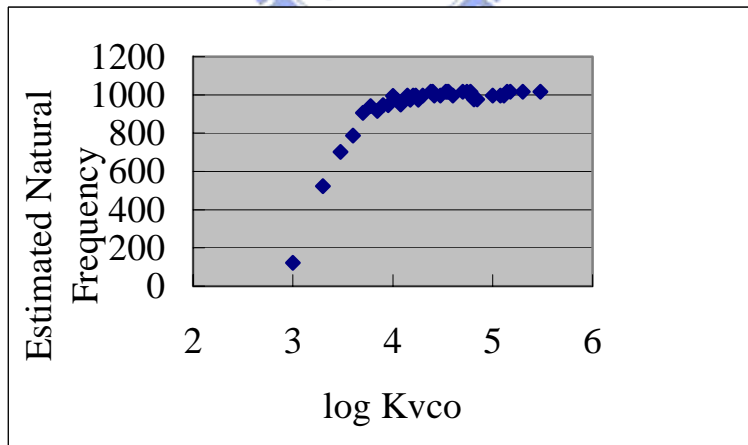
Figure 4.11 (a) Function block diagram for second order system with PLL; (b) experiment apparatus setup.



(a)

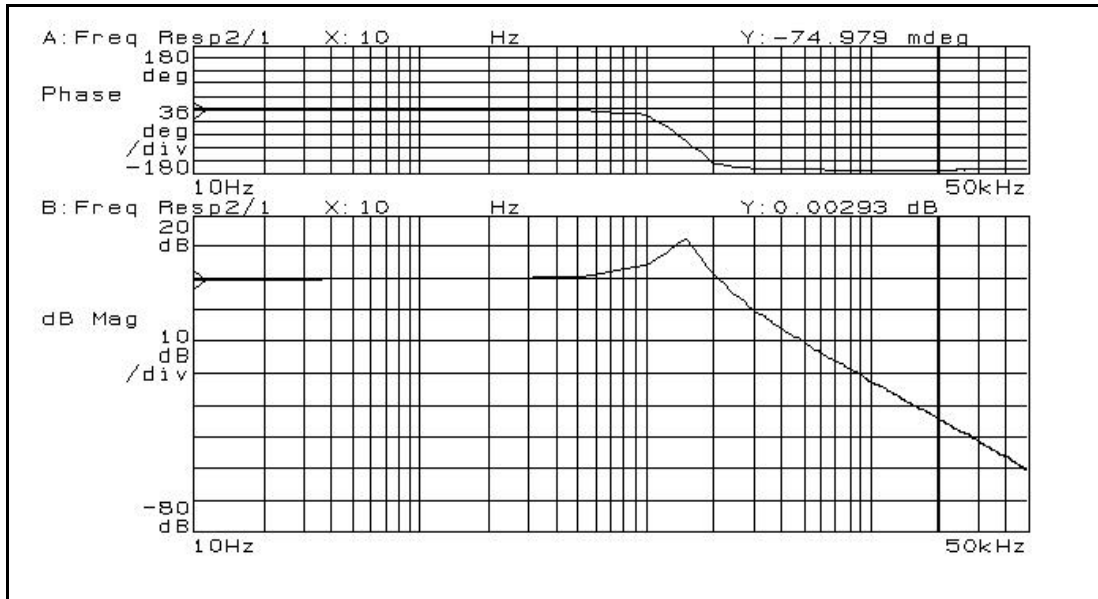


(b)

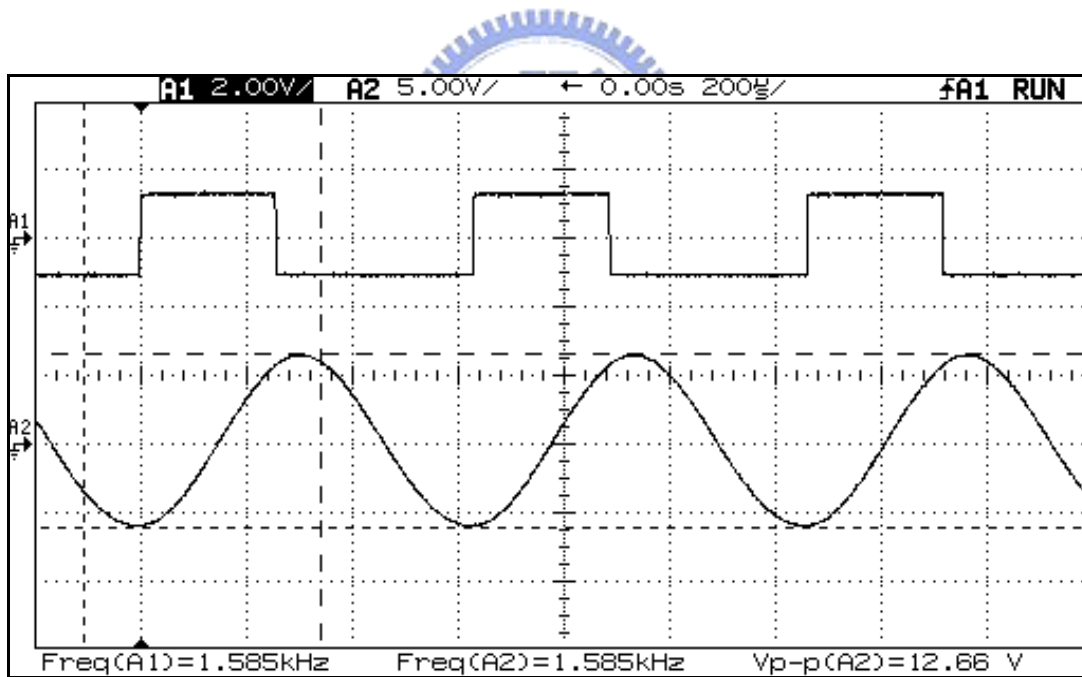


(c)

Figure 4.12 Numerical results: (a) $\zeta = 1$; (b) $\zeta = 0.01$; (c) $\omega_n = 1000\text{Hz}$ and $\zeta = 0.01$.

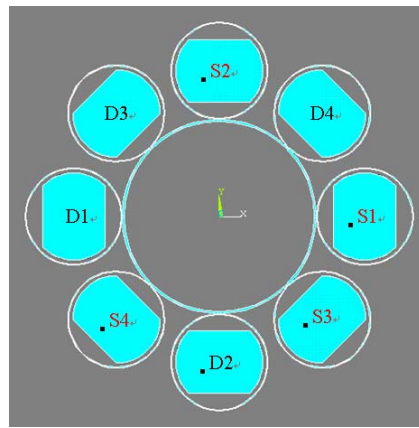


(a)

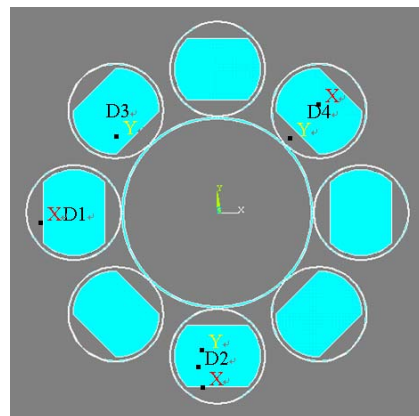


(b)

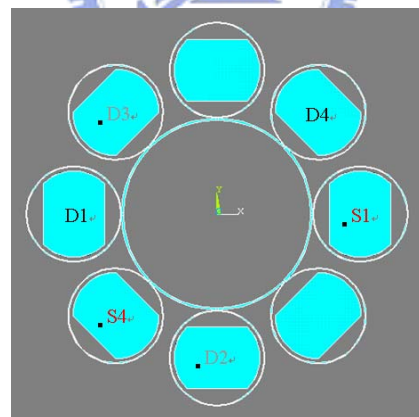
Figure 4.13 Experimental results: (a) bode diagram of the emulation plant; (b) tracking profile.



(a)



(b)



(c)

Figure 4.14 (a)Arrangement of driving electrodes and sensing electrodes;(b) linear displacement; (c) rotation.

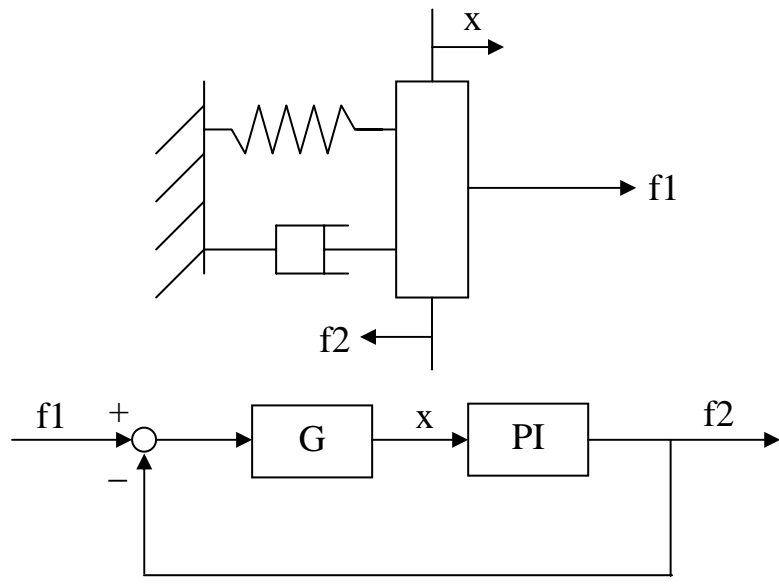


Figure 4.15 Schematic function diagram for rebalanced control circuit.

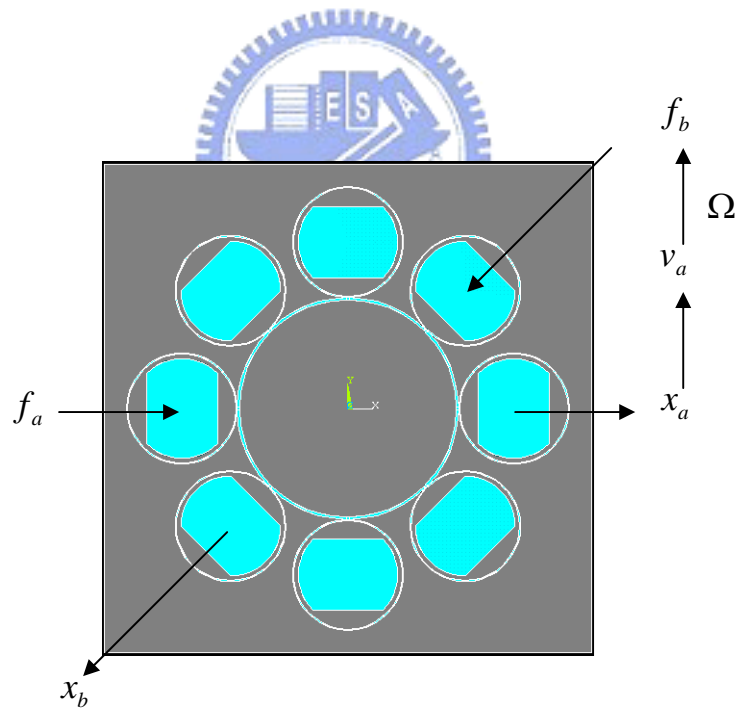


Figure 4.16 Applying forces and corresponding displacements under second mode.

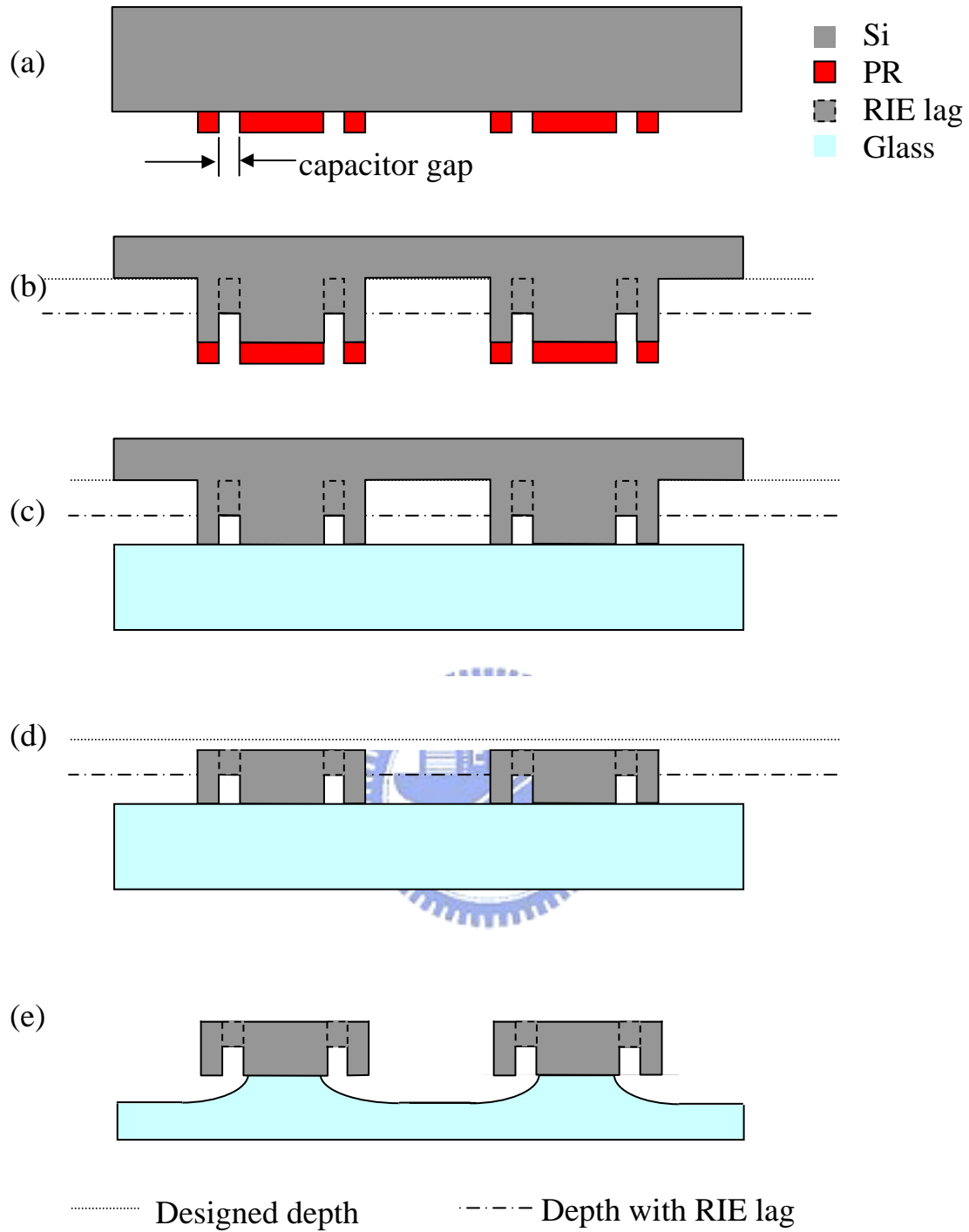
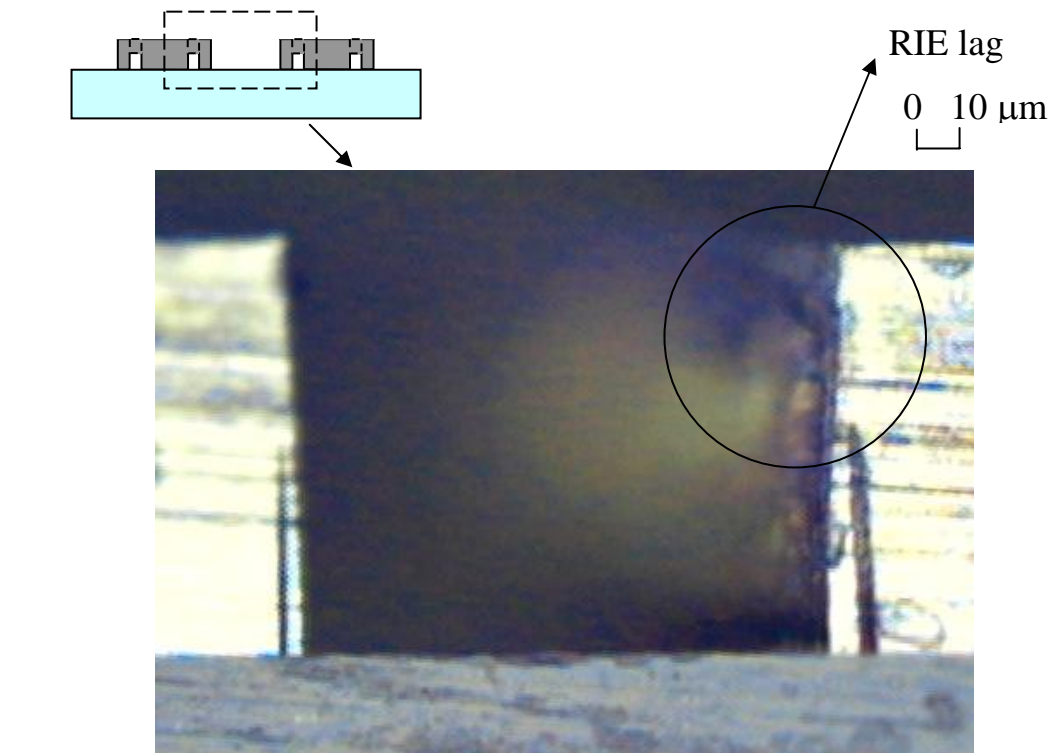
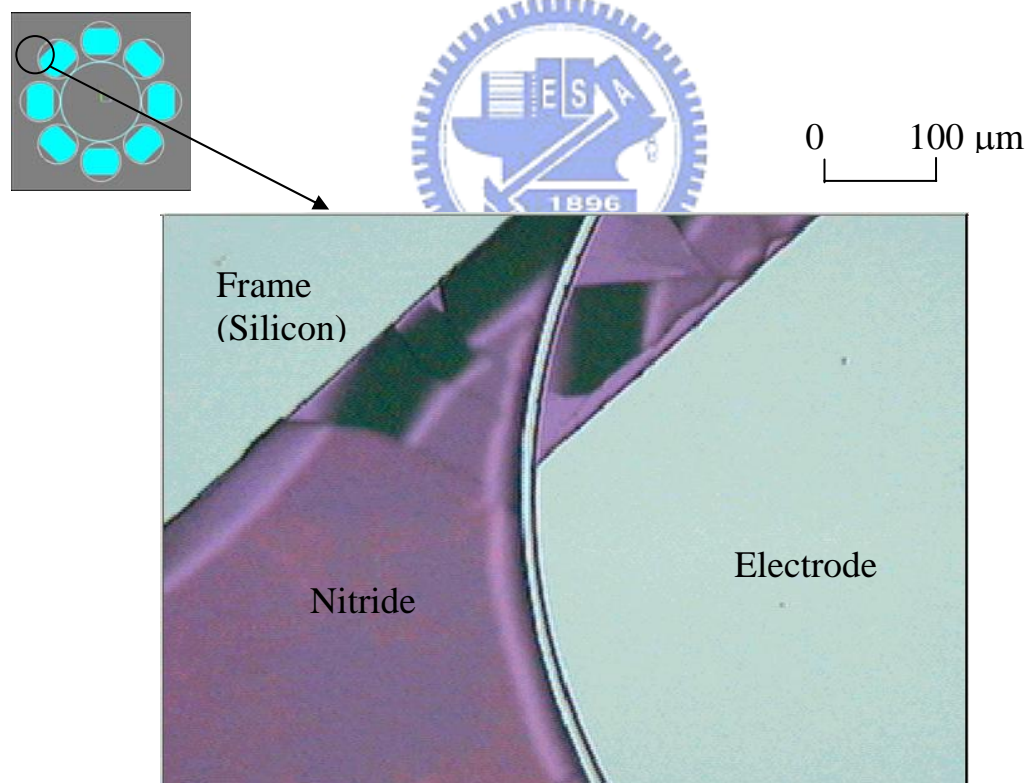


Figure 5.1. Fabrication by method I: (a) silicon patterning using photo resist, (b) deep silicon etching, (c) anodic bonding, (d) back-sided wet etching and (e) releasing of structure.



(a)



(b)

Figure 5.2 Photographs of the ring-type motion sensor fabricated by the process shown in Fig. 5.1. (a) Side view of the structure, with ARDE effect shown; (b) top view of a corner of the structure, 20 μ m high.

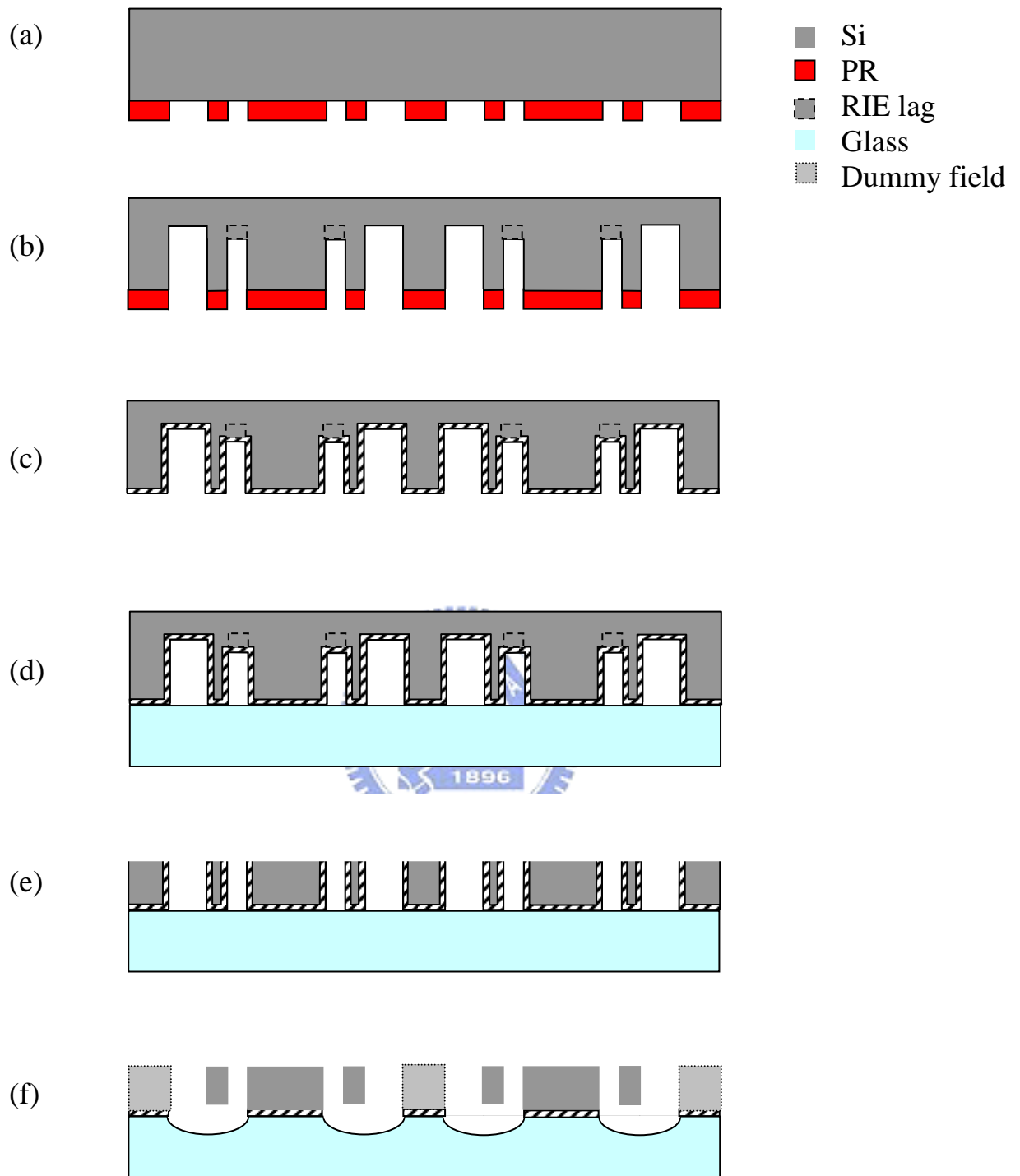


Figure 5.3 Fabrication by method II (method I with dummy fields): (a) silicon patterning using photo resist, (b) deep silicon etching, (c) protective layer deposition, (d) anodic bonding, (e) back-sided wet etching and (f) releasing of structure.

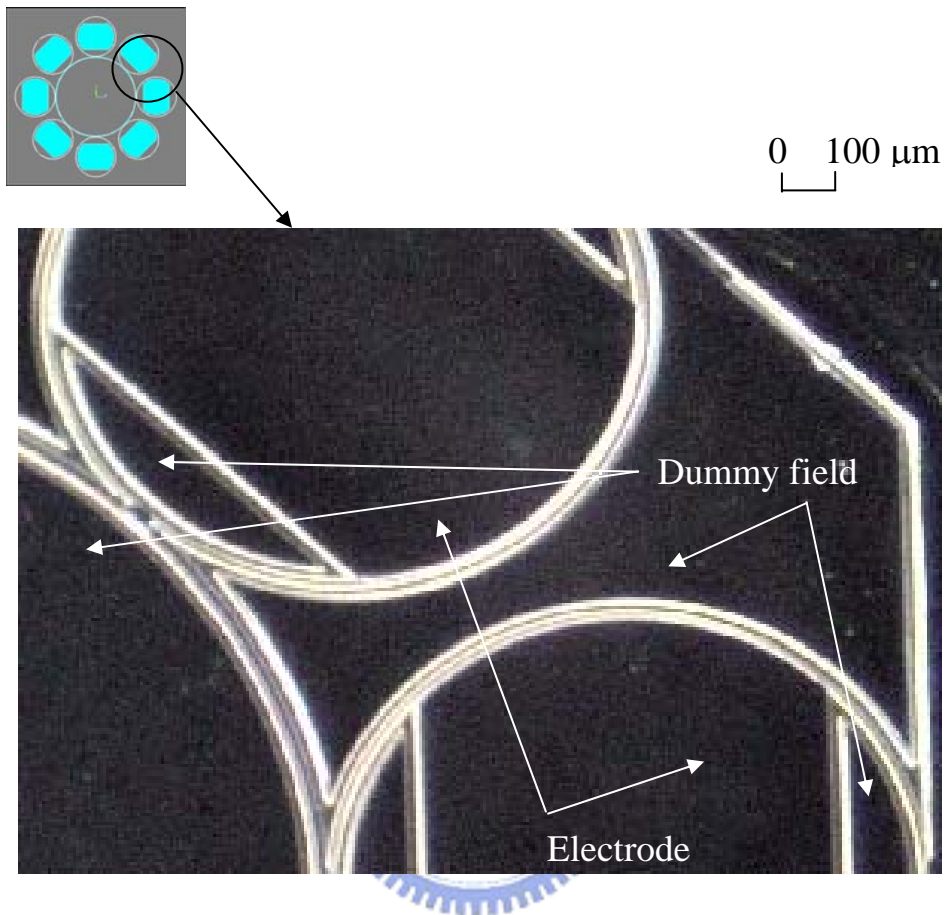


Figure 5.4 Photographs of the ring-type motion sensor fabricated using process shown in Fig. 5.3. Top view of the structure, 60 μ m high.

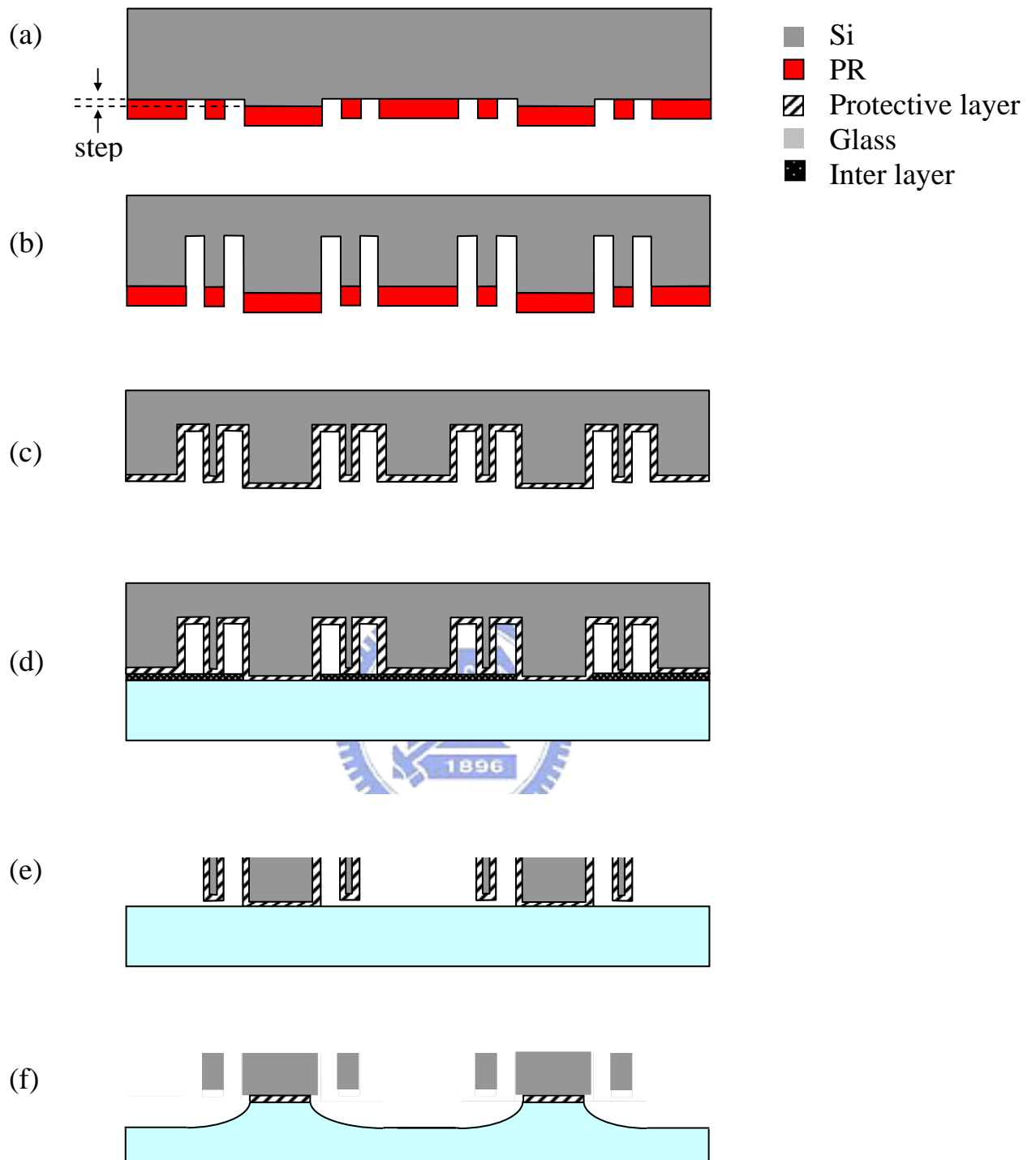


Figure 5.5 Fabrication by method III: (a) silicon patterning using photo resist, (b) deep silicon etching, (c) protective layer deposition, (d) anodic bonding, (e) back-sided wet etching and (f) releasing of structure.

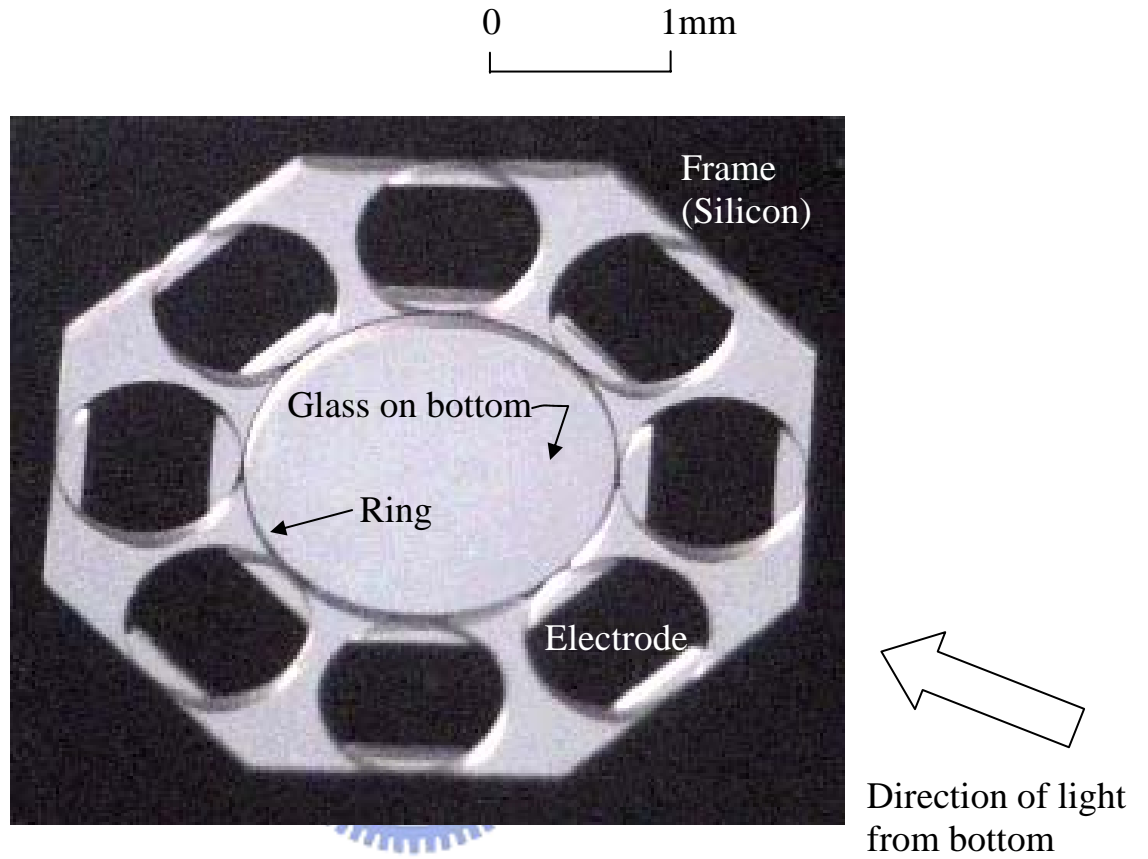


Figure 5.6 Photographs of the ring-type motion sensor fabricated using process in Fig. 5.5. Top view of a structure with a height of $180\mu\text{m}$, under back lighting through the glass.

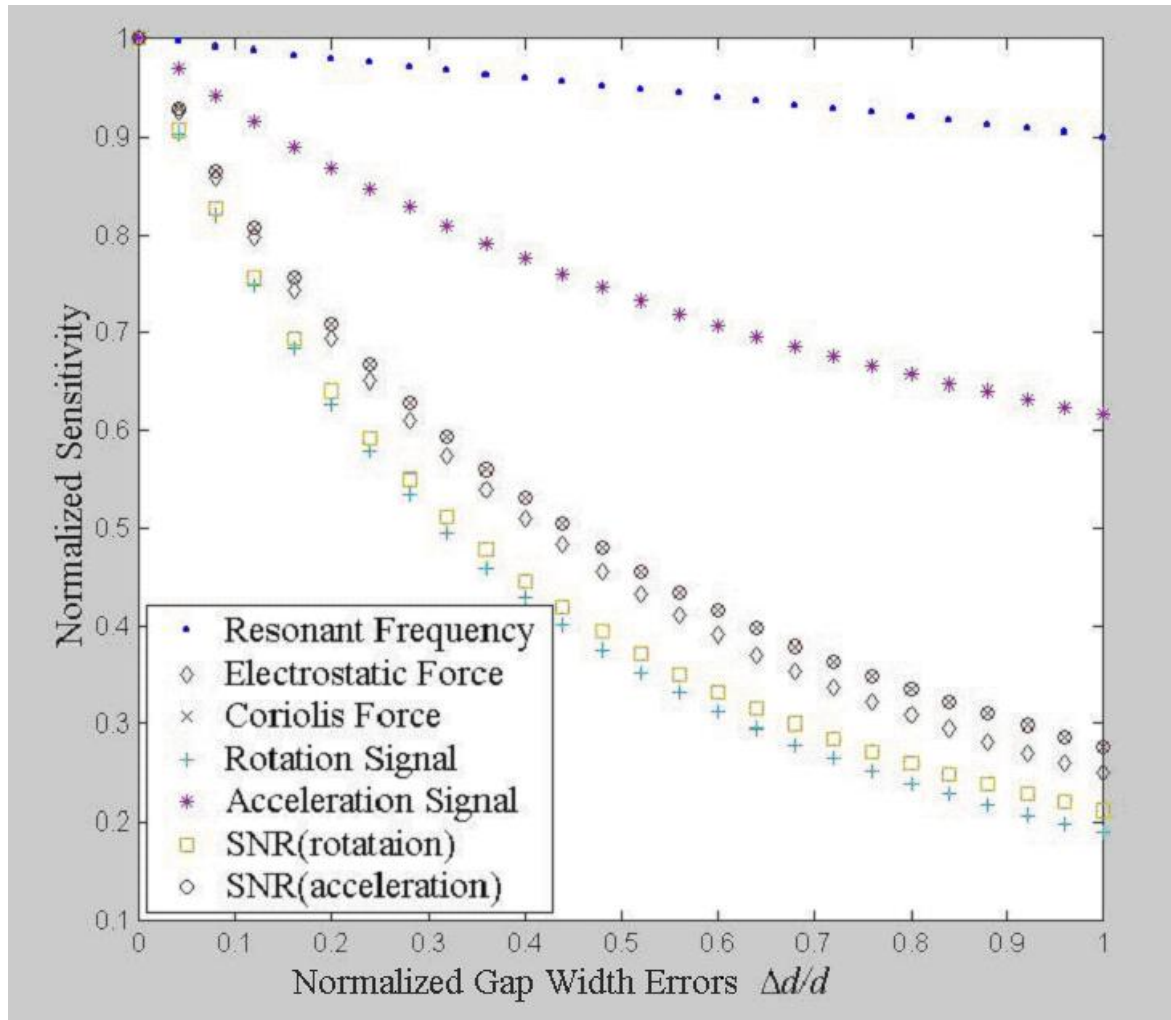


Figure 5.7 Normalized sensitivities of sensor characteristic of interest versus manufacturing errors in the gap width.

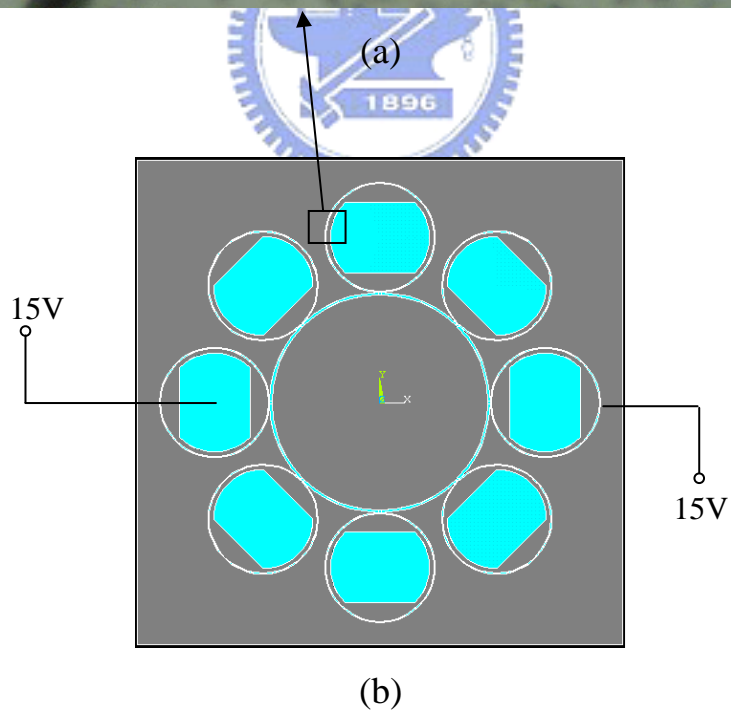
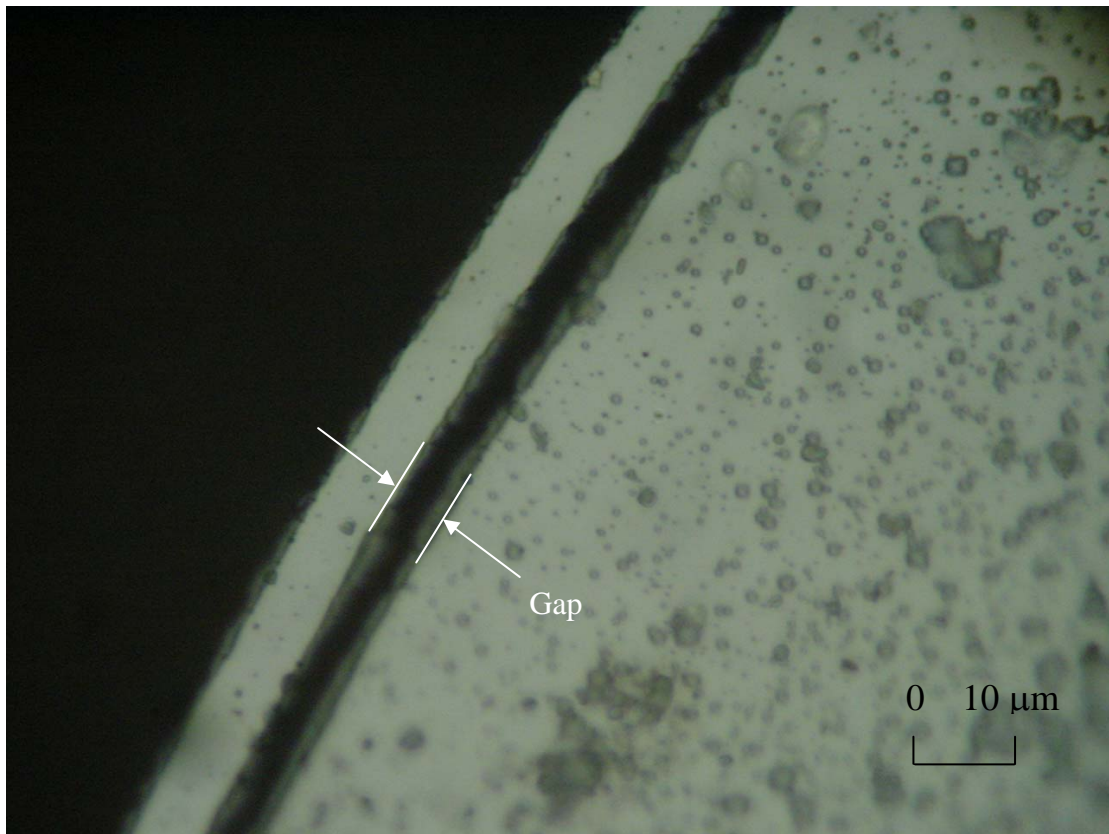


Figure 5.8 (a) Photograph of the ring-type motion sensor when the support ring is in a neutral position. (b) Electrical connections.

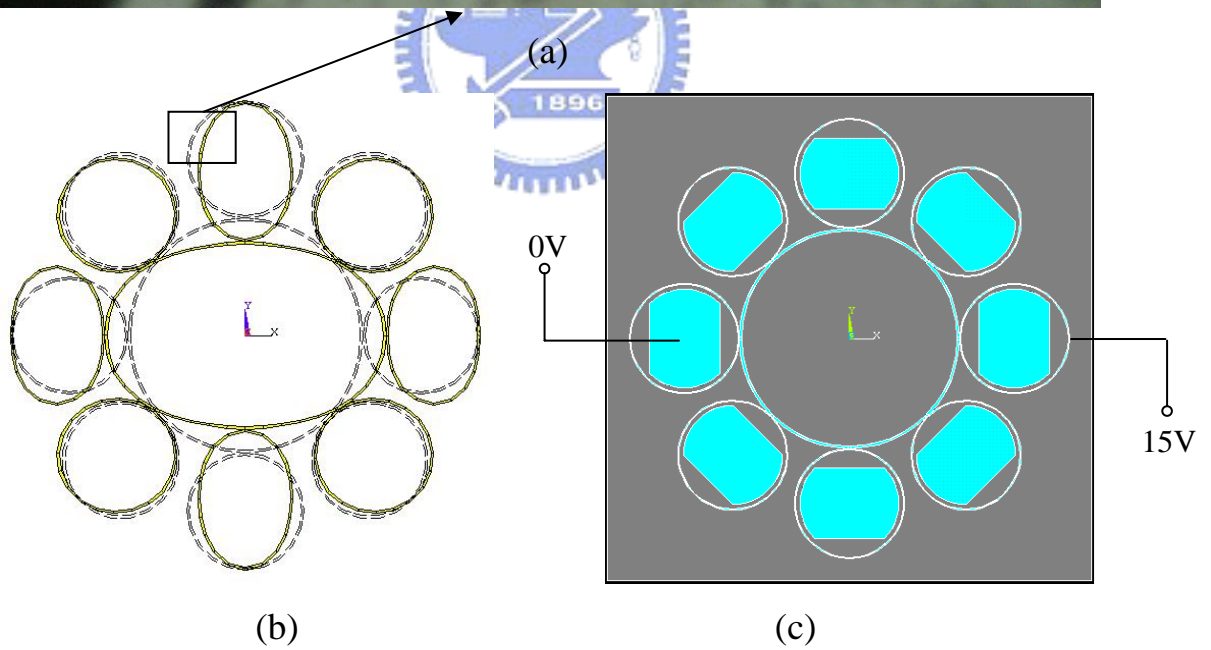
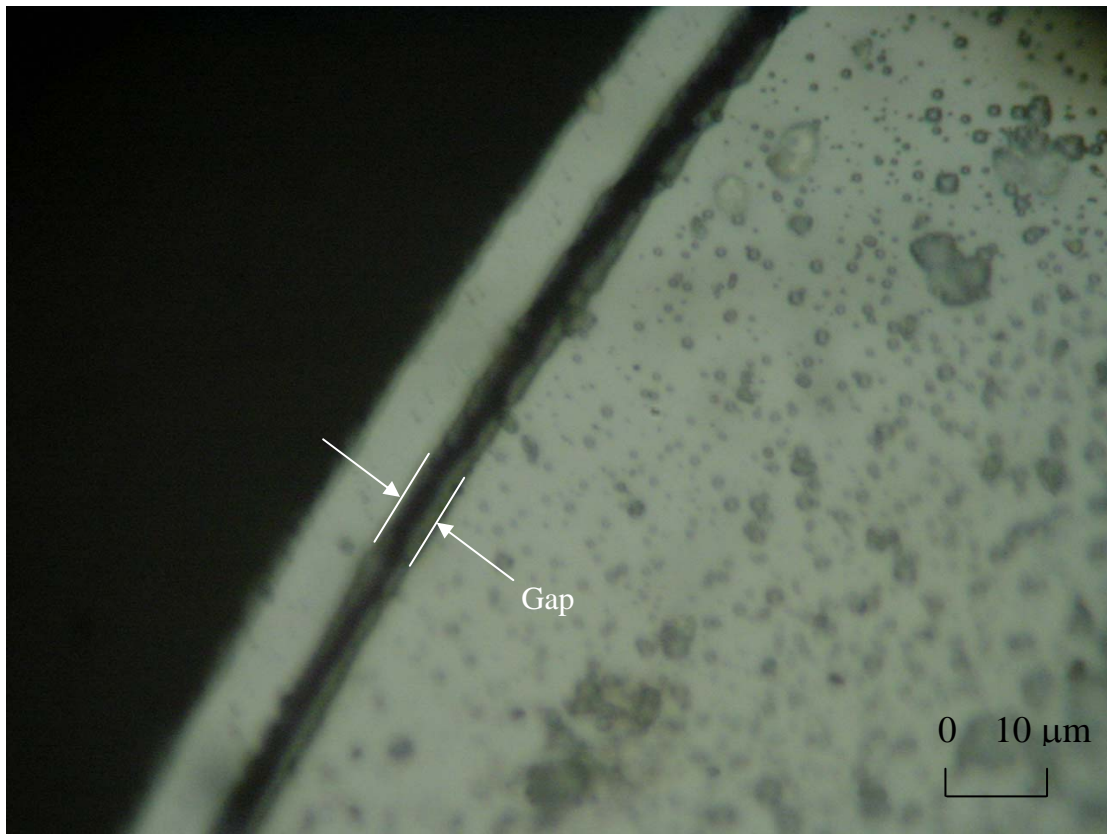


Figure 5.9 (a) Photograph of the ring-type motion sensor when the support ring is attracted by electrode. (b) Deformed structure. (c) Electrical connections.

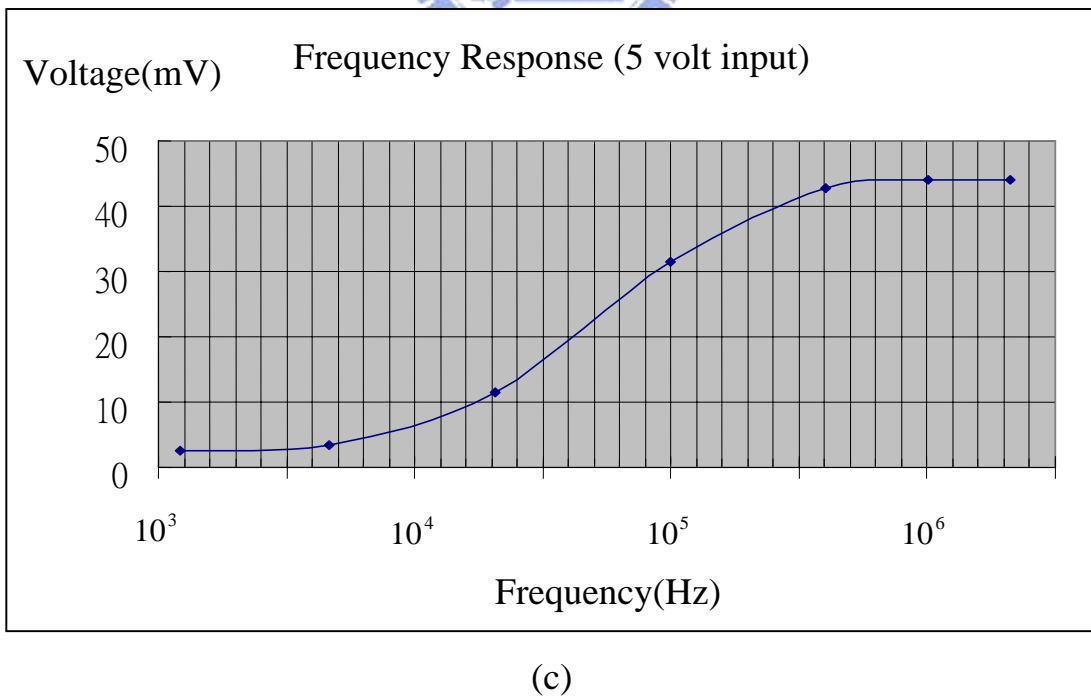
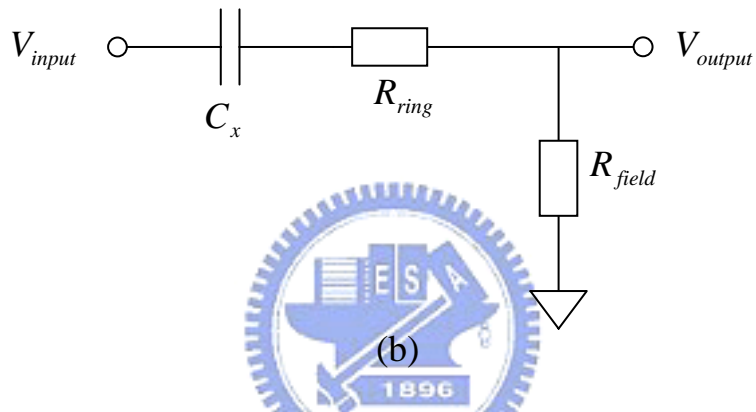
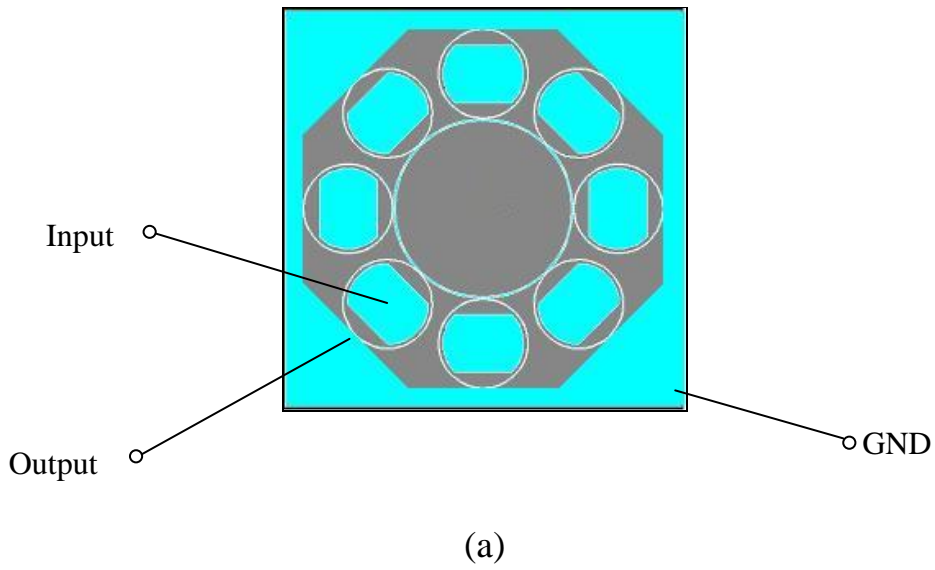


Figure 5.10 (a) Connections of electrical test. (b) Simplified model. (c) Frequency response.

Table. 1 Natural frequency of separated parts of the structure.

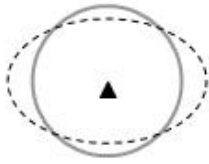
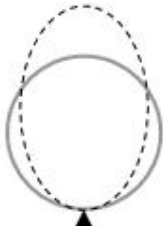

	main ring	extending support ring	rotating support ring
Mode			
Natural Frequency	$\omega_1 = \sqrt{\frac{3}{5} \cdot \frac{E}{\rho} \cdot \frac{w^2}{r^4}}$	$\omega_2 = 1.24\omega_1$	$\omega_3 = 0.4\omega_1$ $\omega_3' = 2.58\omega_1$

Table. 2 Comparison of calculated and simulated results.

	Analytical	FEM (Ansys5.3)
Resonant Frequency of Center Fixed Ring	20926 Hz	20990 Hz
Resonant Frequency of Side Fixed Extension Ring	25955 Hz	25457 Hz
Resonant Frequency of Side Fixed Rotation Ring	8456 Hz	9047 Hz
Resonant Frequency of Total Structure	21935 Hz	22823 Hz
Displacement caused by Electrostatic Force	2.56E-5 mm	2.46E-5 mm
Displacement caused by Acceleration	1.07E-5 mm	1.19E-5 mm
ring radius: 1mm, ring width: 20um, ring thickness: 250um, Young's modulus: 150GPa, material density: 2300kg/m ³ , applied electrostatic force: 5.43μN, applied acceleration: 9.8m/s ² .		

Table. 3 Comparison of identification data and experimental results.

Plant Parameters		L = 100mH C = 0.1uF			L = 50mH C = 0.1uF		
Emulation plant identification data							
Theoretical Calculation	ω_n	1.591KHz			2.251KHz		
HP35670A Identification	ω_n	1.589KHz	1.574KHz	1.598KHz	2.246KHz	2.178KHz	2.222KHz
	ζ	0.09	0.2	0.5	0.07	0.227	0.41
Experiment data of estimation & tracking frequency							
Estimation	ω_n	1.598KHz	1.527KHz	1.553KHz	2.295KHz	2.306KHz	2.313KHz
	ζ	0.049	0.127	0.523	0.060	0.161	0.306
Tracking Frequency	ω_n	1.587KHz	1.504KHz	1.534KHz	2.273KHz	2.21KHz	2.208KHz

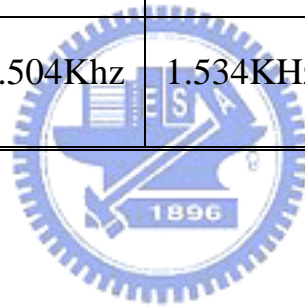


Table. 4 Rebalance Force on Electrodes for Compensating Acceleration.

		Acceleration			
		+X	-X	+Y	-Y
Rebalance Force on Electrodes	D1	1	0	0	0
	D2	0	1	1	0
	D3	0	0	0	$\frac{1}{\sqrt{2}}$
	D4	0	$\sqrt{2}$	0	$\frac{1}{\sqrt{2}}$

Table. 5 Applying forces and induced displacement under second mode.

		f_a	x_a	v_a	f_b	x_b
$\omega_{na} = \omega_{nb}$	No PLL	$\sin(\omega t)$	$\frac{Q}{K} \omega \sin(\omega t - \frac{\pi}{2} + \theta_a)$	$\frac{Q}{K} \omega \sin(\omega t + \theta_a)$	$\frac{Q}{K} \omega \Omega \sin(\omega t + \theta_a)$	$(\frac{Q}{K})^2 \omega \Omega \cdot \sin(\omega t - \frac{\pi}{2} + \theta_a)$
	PLL	$\sin(\omega t)$	$\frac{Q}{K} \omega \sin(\omega t - \frac{\pi}{2})$	$\frac{Q}{K} \omega \sin(\omega t)$	$\frac{Q}{K} \omega \Omega \sin(\omega t)$	$(\frac{Q}{K})^2 \omega \Omega \cdot \sin(\omega t - \frac{\pi}{2})$
$\omega_{na} \neq \omega_{nb}$	No PLL	$\sin(\omega t)$	$\frac{Q}{K} \omega \sin(\omega t - \frac{\pi}{2} + \theta_a)$	$\frac{Q}{K} \omega \sin(\omega t + \theta_a)$	$\frac{Q}{K} \omega \Omega \sin(\omega t + \theta_a)$	$(\frac{Q}{K})^2 \omega \Omega \cdot \sin(\omega t - \frac{\pi}{2} + \theta_a + \theta_b)$
	PLL	$\sin(\omega t)$	$\frac{Q}{K} \omega \sin(\omega t - \frac{\pi}{2})$	$\frac{Q}{K} \omega \sin(\omega t)$	$\frac{Q}{K} \omega \Omega \sin(\omega t)$	$(\frac{Q}{K})^2 \omega \Omega \cdot \sin(\omega t - \frac{\pi}{2} + \theta_b)$

Table 6. Dimensions of parameters.

	Symbol	Formula
Resonant frequency	ω_n	$\sqrt{\frac{E}{\rho}} \cdot \frac{w}{r^2}$
Electrostatic force	F_e	$\varepsilon \cdot V^{cc2} \cdot \frac{rt}{d^2}$
Coriolis Force	F_c	$\Omega \cdot Q \cdot \varepsilon \cdot \sqrt{\frac{\rho}{E}} \cdot V^{cc2} \cdot \frac{t \cdot r^3}{w \cdot d^2}$
Rotation signal	V_{rot}	$\Omega \cdot Q \cdot \varepsilon \cdot \frac{\sqrt{\rho}}{E \sqrt{E}} \cdot V^{cc3} \cdot \frac{r^6}{w^4 \cdot d^3}$
Acceleration signal	V_{acc}	$a \cdot \frac{\rho}{E} \cdot V^{cc} \cdot \frac{r^4}{d \cdot w^2}$
Signal to noise ratio for rotation	SNR(rot)	$\Omega \cdot Q \cdot \varepsilon^2 \cdot \frac{1}{E} \cdot V^{cc3} \cdot \frac{r^3 \cdot t}{w^5 \cdot d^3}$
Signal to noise ratio for acceleration	SNR(acc)	$a \cdot \varepsilon \cdot \sqrt{\frac{\rho}{E}} \cdot V^{cc} \cdot \frac{r^3 \cdot t}{d^2 \cdot w}$
<p>E : Young's modulus of material, ρ : material density, w : ring width, r : ring radius, ε : dielectric parameter, V^{cc} : static applied voltage, t : ring thickness, d : gap between ring and electrode, Ω : rotation rate, Q : quality factor, a : acceleration.</p>		

翁瑞鴻 (Jui-Hong Weng)

List of Publication

1. Jui-Hong Weng, Wei-Hua Chieng and Jenn-Min Lai, “Structural fabrication of a ring-type motion sensor”, J. Micromech. Microeng. Vol. 14, 2004, 710–716.
2. Jui-Hong Weng, Wei-Hua Chieng and Jenn-Min Lai, “Structural design and analysis of micromachined ring-type vibrating sensor of both yaw rate and linear acceleration”, Sensors and Actuators A, Vol. 117, 2005, 230–240.

